Fracture Network Modelling in a geological complex considered for carbon dioxide (CO_2) injection in the offshore area of the Lusitanian Basin

Madalena da Silva Branco Barata

Thesis to obtain the Master of Science Degree in

Energy Resources Engineering

Supervisors:
Prof. Leonardo Azevedo Guerra Raposo Pereira
Prof. Carlos Alexandre Ribeiro

Examination Committee:
Chairperson: Prof. Ana Paula Alves Afonso Falcão Neves
Supervisor: Prof. Carlos Alexandre Ribeiro
Member of the Committee: Dr. Pedro Pereira

November 2024

I declare that this document is an original work of my own authorship and that it fulfills all the requirements of the Code of Conduct and Good Practices of the Universidade de Lisboa.

Abstract

The following thesis focuses on developing conceptual models of fracture networks to be used as analogues for a geological complex targeted for carbon dioxide (CO_2) storage in the offshore area of the Lusitanian Basin. This work presents a fracture interpretation and characterization, followed by a statistical analysis of the identified fractures, leading to the development of several fracture network scenarios.

The main objective is to characterize and model fractures in the sealing formation and assess how these fracture networks could impact the feasibility of CO_2 storage. The study's main data source is the 3D seismic volume of Cabo Mondego, which allowed the creation of comprehensive conceptual models, given the data limitations in the target area.

Developing conceptual fracture network models provided an extensive characterization of the fractures within the study area by proposing different potential scenarios of their occurrence. The models derived from these scenarios allowed the visualization of possible fracture distributions, considering the main fracture characteristics, and offering a useful analogue for understanding their behavior in the target area.

This thesis is aligned with the PilotStrategy project, which aims to improve the understanding of deep saline aquifers for CO_2 storage across Europe. Integrating this work with the broader project by considering the fracture scenarios in the dynamic simulations, provides valuable insights into the dynamic behavior of the target area and the CO_2 storage potential within the offshore Lusitanian Basin.

Keywords: Lusitanian Basin; CO_2 geological storage; fracture characterization; conceptual models

Resumo

A presente dissertação tem como foco o desenvolvimento de modelos conceptuais de redes de fraturas a serem utilizados como análogos para um local identificado para armazenamento geológico de CO_2, na zona offshore da Bacia Lusitaniana. Este estudo apresenta uma interpretação sísmica e caracterização das fraturas, seguida de uma análise estatística, que conduz ao desenvolvimento de vários cenários de rede de fraturas.

O principal objetivo passa por caracterizar e modelar as fraturas da rocha selante, compreendendo o impacto das mesmas no complexo de armazenamento. A principal fonte de dados deste estudo é o volume sísmico 3D de Cabo Mondego, que permitiu o desenvolvimento de modelos conceptuais robustos, dadas as reconhecidas limitações de dados na área de estudo.

O desenvolvimento de modelos conceptuais permitiu uma caracterização detalhada das fraturas existentes na área de estudo, propondo diferentes possibilidades para a sua ocorrência e permitindo a visualização de potenciais cenários de distribuição de fraturas, com base nas principais características das mesmas, fornecendo assim um análogo eficaz para compreender o comportamento das fraturas na região.

Esta dissertação foi desenvolvida no âmbito do projeto PilotStrategy, que tem como objetivo o estudo de Aquíferos Salinos Profundos como local para armazenamento geológico de CO_2 em várias regiões europeias. A integração deste trabalho no projeto referido, através da integração dos cenários de fraturas nas simulações dinâmicas, fornece informações relevantes sobre o comportamento dinâmico da região e sobre o potencial de armazenamento geológico de CO_2 no offshore da Bacia Lusitaniana.

Palavras-chave: Bacia Lusitaniana; Armazenamento geológico de CO_2; caracterização de fraturas; modelos conceptuais

Table of Contents

List of Figures

List of Tables

List of Histograms

List of Equations

List of Acronyms

CO_2 – Carbon Dioxide

ppm – Parts per million

IPCC – Intergovernmental Panel on Climate Change

CCUS – Carbon Capture, Utilization and Storage

CCS – Carbon Capture and Storage

DSA – Deep Saline Aquifer

H/L – Height/Length Ratio

1 Introduction

1.1 Motivation

The urgency to mitigate climate change has demanded the development of innovative technologies to reduce carbon dioxide (CO_2) emissions. Among these technologies, Carbon Capture Utilization and Storage (CCUS) involves the sequestration of CO_2 in deep geological formations, including depleted oil and gas reservoirs, unminable coal seams, and deep saline aquifers. The geological suitability of a storage site requires adequate capacity while ensuring permanent confinement of the CO_2 and preventing leakage. Deep saline aquifers, porous rock formations saturated with brine, have emerged as promising sites for CO_2 geological storage. However, the presence of faults and fractures in these formations can pose significant challenges to long-term storage. Therefore, modelling and characterizing the fracture network is crucial for understanding the effects of faults on seal integrity and assessing the risk of CO_2 leakage.

Portugal holds significant potential for CO_2 storage in deep saline aquifers due to its extensive sedimentary basins. However, the scarcity of hard data on these formations justifies the creation of fracture models that accurately characterize and assess their impact on CO_2 storage. This characterization will be used to evaluate the influence of fault and fracture networks on the sealing formation integrity, identify potential leakage pathways, and assess the feasibility of CO_2 storage in the area. This study looks forward to offer valuable perspectives on the potential of CCUS in Portugal, emphasizing on the significance of seal integrity within a CO_2 storage complex and emphasizing the crucial understanding of risk mitigation. These insights aim to inform future CCUS strategies, aligning both national and international climate goals.

The work presented herein contributes to the PilotStrategy project[1], an international project funded by the European Union Horizon 2020 and is coordinated by the University of Évora in Portugal. This project focuses on investigating CO_2 geological storage sites in industrial regions of Southern and Eastern Europe to support the development of carbon capture and storage (CCS). The alignment with PilotStrategy's goals not only enriches the research framework but also strengthens the connection between the study, and practical, real-world advancements in the field of carbon capture technologies.

---

[1] https://pilotstrategy.eu/

1.2 Objectives

The work to be developed in the aim of the thesis focuses in developing a set of conceptual models of fracture networks in a geological complex considered for carbon dioxide (CO_2) injection in the offshore area of the Lusitanian Basin. The main goal is to characterize and model fractures in the sealing formation of the injection site and evaluate the impact of fracture networks on the feasibility of CO_2 storage in the area, while compiling all available data sources, including 2D and 3D seismic data, well data, reports, and more, to produce conceptual models based on this comprehensive information. Given the limited availability of fracture-related data in the target area, the creation of fracture network scenarios is expected to be necessary for further integration into the dynamic modeling phase. The data gathering process also involves data collection through field trips and the utilization of analogous data. The work includes literature review, seismic interpretation, seismic attributes analysis, fracture properties characterization and the construction of conceptual geological models of the fracture network.

This study utilizes real data, while being aligned with the PilotStrategy project. The widespread goal of PilotStrategy is to enhance the understanding of deep saline aquifers for CO_2 geological storage across five European industrial regions. The integration of this work with the broader project aims to contribute with valuable insights into the dynamic behavior of fracture networks within the specified geological complex, furthering the understanding of the potential for CO_2 geological storage in the offshore area of the Lusitanian Basin.

1.3 Structure of the thesis

The structure for this master's thesis includes six chapters. Firstly, in Chapter 1 the objectives and motivation that led to this work are introduced. In Chapter 2 it is presented an extensive literature review covering various topics that are crucial for the subsequent work. Following the literature review, the case study is presented with geographical and geological settings of the area and an overview of the available dataset is provided (Chapter 3). Subsequently in Chapter 4, a description of the methodologies employed for fracture modelling will be presented. This leads to the development of fracture network scenarios that represent potential fracture distributions in the target area, which are presented in results' chapter together with other key results and discussion (Chapter 5). Finally, the conclusions are presented in Chapter 6.

2 Literature Review

2.1 CCUS Role and Climate Goals

According to the Intergovernmental Panel on Climate Change (IPCC), CO_2 currently makes up a minimal portion of the Earth's atmosphere, around 420 ppm. This concentration has risen from 280 ppm before the Industrial Revolution due to the widespread use of fossil fuels, contributing to the transformation of carbon into CO_2 through combustion (IPCC, 2018). Despite the apparently small change in concentration, this increase is causing severe implications in the carbon cycle balance, which encompasses interactions between the atmosphere, oceans, biosphere, and rocks.

While the carbon cycle involves the movement of carbon through the atmosphere, oceans, and biosphere, it is just a component of a larger cycle that includes substantial carbon reservoirs in rocks. The geological cycle involves the deposition of sediments containing carbon from plants and animals, forming rocks that effectively store carbon (Berner, 2003). Geological processes, such as the uplift of mountains, erosion and volcanic activity, release carbon from deeply buried rocks back into the atmosphere and oceans, initiating the cycle again. Human activities, particularly the combustion of fossil fuels, disrupt this balance by rapidly introducing carbon from the geological cycle into the atmosphere. This disturbance has thrown the natural equilibrium of the carbon cycle off balance.

In response to the escalating threat of climate change, the Paris Agreement was established in December 2015 at the United Nations Climate Change Conference (https://unfccc.int/). This agreement, signed by global political leaders, outlines three key climate goals: (i) the short-term goal aims to peak carbon emissions into the atmosphere as soon as possible, while (ii) the long-term goals are to limit the increase in global average temperature to below 2 degrees Celsius, preferably to 1.5 degrees Celsius, compared to pre-industrial levels and (iii) to achieve a neutral carbon balance in the atmosphere by mid-century (UNFCCC, 2022). Climate scientists emphasize the urgency of these efforts, warning that without substantial action on climate change, the global temperature could increase by more than 4 degrees Celsius by the end of the century, leading to severe consequences.

The interest in CO_2 capture and storage outcomes from global concerns about climate change, leading to the establishment of the United Nations Framework Convention on Climate Change (UNFCCC) in 1992. The primary goal of this convention was the "stabilization of greenhouse gas concentrations in the atmosphere at a level that prevents dangerous anthropogenic interference with the climate system." (United Nations, 1992). Considering CCUS in this context it aligns with the international objective of stabilizing atmospheric greenhouse gas concentrations. The extent of emissions reduction necessary for stabilizing

CO_2 concentration depends on both future emissions levels (baseline) and the targeted long-term CO_2 concentration. Lower stabilization targets and higher baseline emissions necessitate more substantial reductions in CO_2 emissions.

The Energy Technology Perspectives Report (IEA, 2020) from the International Energy Agency (IEA) underscores the crucial role that CCUS must assume. It is identified as one of the four key pillars essential for global energy transitions, standing alongside renewables-based electrification, bioenergy, and hydrogen. In this regard, the inclusion of CCUS in the array of options for reducing greenhouse gas emissions can facilitate the achievement of stabilization goals. Model results indicate that utilizing CCUS alongside other measures could not only significantly reduce the cost of stabilization but also enhance flexibility in achieving these reductions.

According to scenarios outlined by the International Energy Agency (IEA, 2020), CCUS is projected to contribute significantly to the required reduction in CO_2 emissions. By 2070, it is estimated to contribute 15% of the cumulative reduction in CO_2 emissions worldwide.

Industry sector emissions are among the hardest to abate in the energy system, posing significant challenges both technically and financially. This sector is a major contributor to global CO_2 emissions, accounting for nearly a quarter of it (Figure 1) – in 2022 9 Gt CO_2 of direct emissions were recorded (IEA, 2022). When considering indirect emissions, from industrial power and heat demand, the sector's responsibility extends to almost 40% of CO_2 emissions. The steel and cement subsectors are the highest emitters, along with iron and chemicals, collectively contributing to nearly 70% of industrial emissions in 2017. These subsectors face difficulties in decarbonization due to the need for high-temperature heat and inherent process emissions that cannot be avoided with a switch to renewable energy sources.

Shifting from fossil fuels to low-carbon alternatives for heat generation would necessitate facility modifications and significantly increased electricity demand (IEA, 2019). Furthermore, about one quarter of industrial emissions are process emissions resulting from chemical or physical reactions, particularly prevalent in cement production (accounting for 65% of emissions) (Figure 2), as well as in iron, steel, aluminum, and ammonia production. These process emissions pose a unique challenge as they cannot be eliminated by switching to alternative fuels as well.

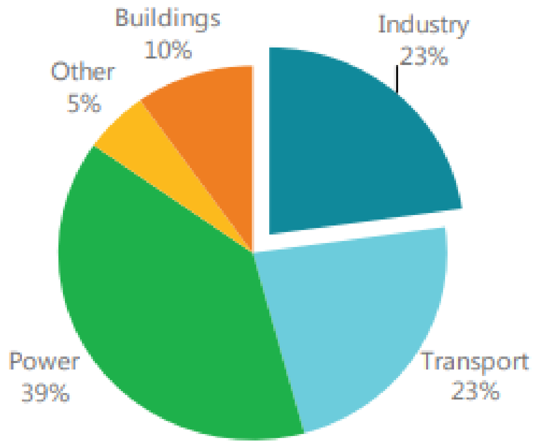

Figure 1- Direct CO_2 emissions by sector in 2017 Source: (IEA, 2019)

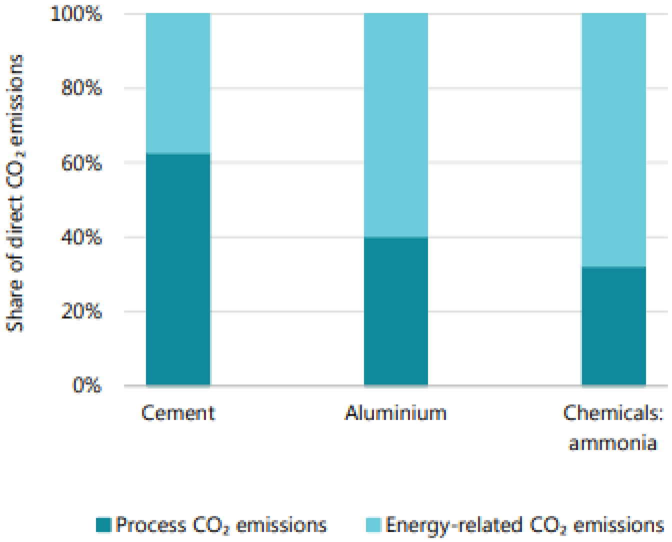

Figure 2- Process emissions by industry subsector in 2017 Source: (IEA, 2019)

Expanding the use of CCUS holds particular significance for the decarbonization of industries. It emerges as a crucial solution in mitigating emissions from challenging industry subsectors, such as cement, iron and steel, and chemicals. Alongside measures like energy efficiency, electrification (including electrolytic hydrogen), and greater reliance on renewable energy, CCUS forms an integral part of a technology portfolio capable of achieving substantial emissions reductions at the lowest cost in these subsectors. The establishment of CCUS hubs in industrial areas with shared CO_2 transport and storage infrastructure can lead to cost savings for facilities adopting carbon capture in their production processes (IEA, 2019). CCUS stands out as a valuable tool, being able to significantly reduce emissions while supporting a cost-effective industrial transition aligned with the Paris Agreement objectives.

In the scope of Portugal's energy and industry strategies, facing challenges posed by global warming is a multifaceted task that involves varied solutions. The industrial sector contributes around 18% of the total

CO_2 emissions (IEA, 2021). As Seixas et al. (2015) report mentioned, the cement sector is expected to be the main industry requiring CO_2 storage due to its elevated process emissions. Approximately two-thirds of the CO_2 emitted by this sector in 2018 comes from industrial processes and are not possible to mitigate through fuel switching. Achieving carbon neutrality in sectors characterized by high process emissions necessitates the geological storage of CO_2.

Meeting the ambitious goal of reducing greenhouse gas (GHG) emissions necessitate comprehensive changes across all sectors of the economy. Economists point to carbon pricing as a policy instrument that can encourage innovation and minimize the costs of transitioning to a low-carbon economy. Instead of governments impose specific emission reduction techniques, a carbon price assigns a monetary value to carbon emissions, creating an economic incentive for companies to reduce their environmental impact. In this way, companies are encouraged to identify and implement cost-effective emission reduction strategies tailored to their specific circumstances. By leveraging this market's efficiency, carbon pricing facilitates the achievement of environmental objectives in a flexible and economically advantageous manner (World Bank, 2017).

While there are some exceptions, such as Sweden, Switzerland, Norway, Finland and Lichenstein, in 2023 the majority of carbon prices in European countries are in the range of 1€–50€/tCO_2e (World Bank, 2023). To achieve the Paris temperature target, the High-Level Commission on Carbon Prices (World Bank, 2017) concluded that prices would need to be at least US$40–80/$tCO_2$ (36.65€-73.30€/tCO_2) by 2020 and US$50–100/$tCO_2$ (45.81-91.62€/tCO_2) by 2030[2]. “Countries may choose different instruments to implement their climate policies, depending on national and local circumstances and on the support they receive” ((World Bank, 2017).

By the end of 2023, Portugal approved the legal framework for the implementation of a voluntary carbon market. This market is about creating conditions for the development of instruments that help to meet national commitments to combat climate change, aligned with the Paris Agreement and the European strategy to achieve carbon neutrality by 2050. The voluntary carbon market will focus on projects to reduce GHG emissions and carbon sequestration projects, developed in Portugal, that promote emission mitigation, with compensation for those that cannot be reduced or avoided. The goal is for companies to have the opportunity, through this new regime, to acquire carbon credits (units that represent a certain amount of GHG emissions that have been reduced or avoided), as a way to offset emissions of polluting gases they cannot reduce or avoid, but also to value their investments in projects or solutions developed to reduce or eliminate carbon footprint (Jornal de Negócios, 2023).

---

[2] Carbon tax rates were converted using the EUR-USD currency conversion rate as of January 21, 2024 (USD 1 = EUR 0.9162).

2.2 CO_2 capture, transport, and utilization

The CCUS process comprises four key stages: capture, transport, utilization, and storage. This CO_2 is mainly captured from two major emissions sources: industrial activities and fuel combustion. Typically, CO_2 is separated from other gases emitted from industrial processes. Once captured, the CO_2 is cleaned and compressed before being transported to an injection site deep underground for permanent storage. CO_2 geological storage consists in injecting CO_2, into deep underground rock formations, ensuring its permanent removal from the atmosphere (IEA, 2020).

CO_2 capture plays a crucial role in various industrial processes, with established technologies for separating or capturing CO_2 from flue gas streams being commercially available for many years. In the context of CCUS, the focus of capture is to clean CO_2 so it can be economically stored, being extracted as a concentrated CO_2 stream from combustion exhaust gases, making it suitable for transportation to a CO_2 storage site (IPCC, 2005), (Global CCS Institute, 2021). Three main capture processes have been developed:

- Pre-combustion capture: Implemented before the combustion of fossil fuels, this process involves converting solid or liquid fuel into a mixture of CO_2 and hydrogen. The separated hydrogen can be burned without CO_2 production, while the CO_2 is compressed and suitable for transport and storage.
- Post-combustion capture: This process involves separating CO_2 from flue gas generated by the combustion of a primary fuel. Liquid solvents or other separation methods are employed in this approach.
- Oxyfuel combustion processes: In this method, fuel combustion uses oxygen instead of air, resulting in exhaust gas composed of water vapor and CO_2. The CO_2 can be easily separated to produce a high purity CO_2 stream.

The widespread implementation of CCUS relies significantly on the availability of secure and efficient CO_2 transport infrastructure. Large-scale transport of CO_2 primarily occurs through pipelines and ships, with truck or rail transport being viable for shorter distances and smaller volumes. Pipeline transport, already established on a significant scale, offers an economical option, also with potential for repurposing existing natural gas pipelines for CO_2 transport from onshore sources to offshore storage locations. The choice of the CO_2 transport mode is influenced by economic considerations and regulatory frameworks, where pipelines prove to be the most cost-effective means for transporting large quantities of CO_2 (IEA, 2020).

CO_2 can have diverse applications for various products and services. These applications encompass direct utilization, where CO_2 is not chemically altered, as well as the conversion of CO_2 into valuable products. The fertilizer industry stands as the largest consumer worldwide, incorporating CO_2 as a raw material in urea production, which consumes more than 100 $MtCO_2$ per year followed by the oil and gas sector for EOR at nearly 80 $MtCO_2$ consumed (IEA, 2019). Emerging pathways for CO_2 utilization present new solutions such as transforming hydrogen into a synthetic hydrocarbon fuel. Additionally, CO_2 can substitute fossil fuels in the manufacturing of carbon-dependent chemicals and contribute to the production of building materials, potentially replacing water in concrete, or serving as a raw material in its components.

2.3 CO_2 geological storage

Geological storage is the main option for securely storing CO_2, allowing it to be stored for extended periods, within rocks deep below the Earth's surface. Ideal storage sites possess highly permeable and porous rock layers, facilitating the movement of CO_2 through the rock and filling pore spaces. Once injected into the storage site, CO_2 moves upward through the permeable formation until reaching the cap rock, that prevents it from escaping. The storage site becomes increasingly secure over time, initially trapping CO_2 within pore spaces and sealed by a cap rock. Eventually, CO_2 dissolves in the water within the rocks, becoming denser and less mobile (Blunt, 2010). The injection of CO_2 into deep geological formations uses similar technologies to the ones developed in the oil and gas upstream industry, including well-drilling, injection technology, and reservoir dynamics simulation. Experience from other underground injection practices, such as natural gas storage, deep liquid waste injection, and acid gas disposal, contributes with valuable operational insights (IPCC, 2005).

Several authors (Arts, 2008), (Bachu, 2007), state that geological media suitable for CO_2 storage must exhibit specific characteristics, including: the ability to accommodate the intended volume of CO_2 – capacity - the capability to receive CO_2 at a rate consistent with the supply from CO_2 emitters – injectivity - the prevention of CO_2 leakage from the storage space to other subsurface areas, shallow potable groundwater, or the surface – confinement. Sedimentary basins usually offer these characteristics, as sandstone and carbonate formations generally provide the required porosity for storage capacity and permeability for injectivity. Additionally, low-permeability formations such as shales or evaporites, act as confining barriers, preventing CO_2 leakage (Bachu, 2007).

Under the previously mentioned characteristics, various geological media offer distinct storage opportunities: According to Ringrose (2020), deep saline aquifers (DSA) represent the largest available volumes for CO_2 storage and a very promising geological media for CO_2 storage, although still underexplored. Depleted oil and gas reservoirs are another promising option for CO_2 storage as they have already been extensively studied and characterized, and often have well-established infrastructure in place. CO_2 storage in hydrocarbon reservoirs or deep saline formations typically occurs at depths below 800 meters, where pressures and temperatures keep CO_2 in a liquid or supercritical state. After injection, CO2 is compressed and occupies pore spaces, partially displacing existing water (IPCC, 2005). In enhanced oil recovery (EOR) projects CO_2 is injected in the subsurface in order to improve the recovery of hydrocarbons and maintain the reservoir pressure. Coal beds also offer the possibility to store CO_2, either in unminable coal seams or as part of enhanced coal-bed methane (ECBM) projects. However, coal bed storage is not as widely considered as other options because the available storage capacity is relatively limited. A variety of other geological formations have been proposed for CO_2 storage, including volcanic rocks (especially basalts), underground caverns, and oil or gas bearing shale formations (Figure 3).

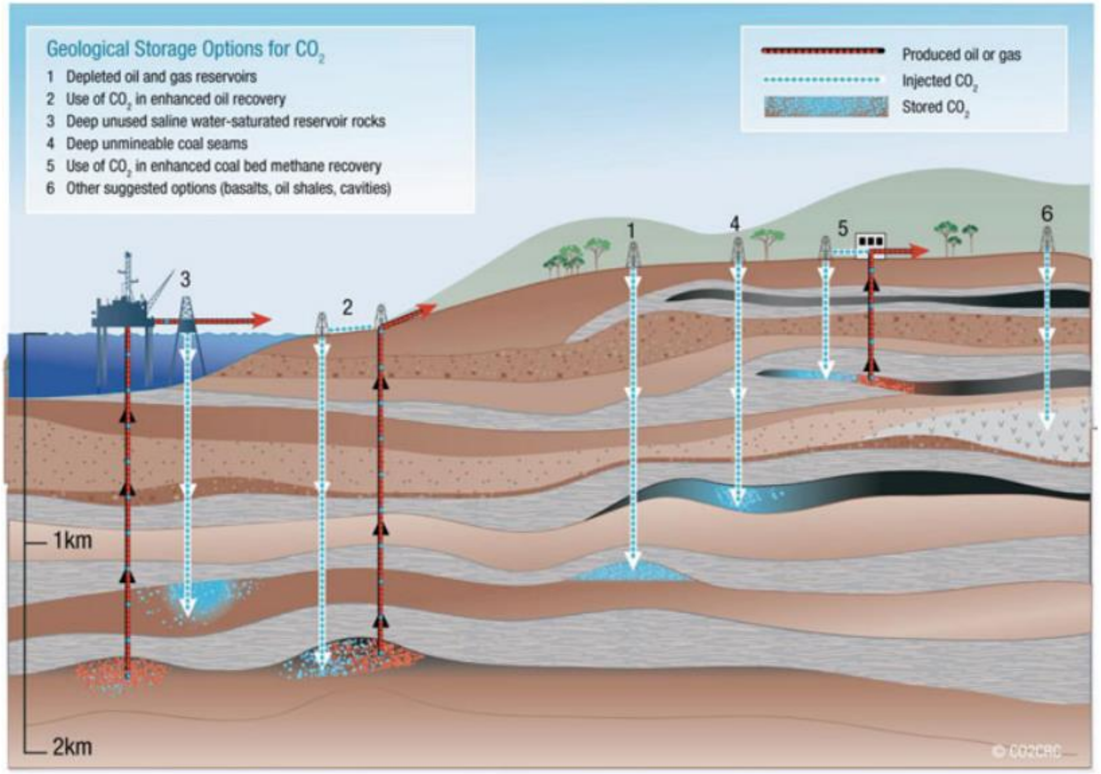

Figure 3- CO_2 geological storage options Source: (IPCC, 2005)

As mentioned, once injected, CO_2 tends to rise to the uppermost part of the rock layer due to buoyancy forces. Ensuring long-term trapping for hundreds to thousands of years can be achieved through four main mechanisms (Figure 4):

- Structural and stratigraphic trapping occur when the injected CO_2 moves upward under buoyancy forces or pressure gradients until it reaches a low permeability rock or structure that prevents further fluid migration. The migration is facilitated by CO_2's density, which is similar to a liquid and viscosity, similar to a gas, being both lower than brine's density and viscosity in the storage formation (Zhang, 2014). Potential traps include cap rocks, faults, and unconformities, with the success of CO_2 sequestration by this mechanism relying heavily on the sealing capacity of the structure/formation (Zhang, 2014). Various forms of structural and stratigraphic traps, or combinations of both, contribute as physical traps to CO_2 geological storage. Structural traps may involve anticlinal folds or fault blocks, while stratigraphic traps commonly consist of low permeability rocks or facies change.

- Residual trapping occurs as CO_2 is injected, moving through porous spaces and displacing brine. When the injection stops, due to different densities, brine re-enters the pore space, leading to a substantial amount of CO_2 to be trapped in the pores without connectivity (Zhang, 2014). This trapping mechanism may happen due to capillary pressures and/or adsorption on mineral surfaces, resulting in an immobile phase within the rock matrix.
- Solubility/dissolution trapping refers to the process of CO_2 dissolving in brine. Once dissolved, CO_2 forms a denser phase that migrates downward through gravitational segregation (Blunt, 2010). The solubility of CO_2 in the brine is influenced by factors like pressure, temperature, and salinity (Zhang, 2014). Previous research suggests that significant CO_2 solubility in brine occurs over extended periods, often taking thousands of years due to its minimal molecular diffusion coefficient (Zhang, 2014).
- Mineral trapping involves the reaction of ions, resulting from CO_2 dissociation in the brine, with minerals within the rock. Precipitation reactions take place as oxides in the rock dissolve and then precipitate as carbonates (Blunt, 2010), (Zhang, 2014). Both dissolution and precipitation processes contribute to the decrease of CO_2 mobility over time. This gradual reduction in mobility enhances storage security, but the challenge lies in the slow nature of these processes, spanning hundreds to thousands of years (Blunt, 2010).

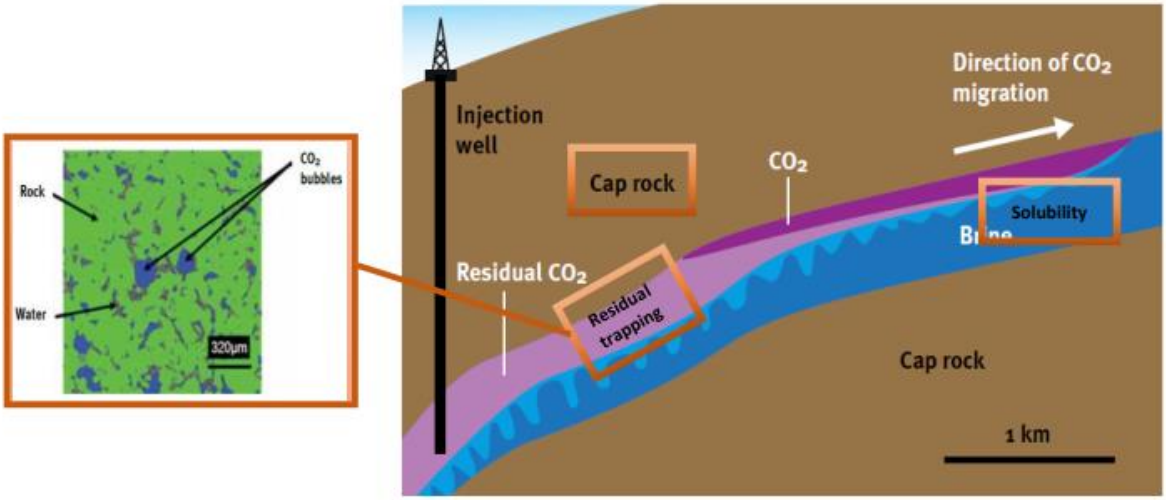

Figure 4- Stratigraphic, residual and solubility trapping in saline formations Source: (Blunt, 2010)

Currently, CO_2 geological storage is operating in a large number of projects: The Sleipner project was the world's first large-scale commercial carbon capture and storage initiative. It is specifically targeted to the Sleipner West natural gas field, where the extracted gas contains high concentrations of CO_2. In the Sleipner facility, CO_2 is separated from the extracted natural gas and is injected into a deep saline aquifer about 800 to 1,100 meters below sea level. The project began in 1996 and has injected over 20 million tonnes of CO_2 to date (Global CCS Institute, 2023). The Sleipner project serves as a landmark in the development of CCS technology demonstrating the feasibility and cost-effectiveness at a large scale of capturing and storing CO_2 from industrial operations. The project has also been shown to be safe and environmentally sound.

Northern Lights project represents a groundbreaking cross-border, open-source CO_2 transport and storage infrastructure network. This innovative system provides companies throughout Europe the opportunity to store their CO_2 securely and permanently beneath the seabed in Norway. In its initial phase, the project aims to capture and store approximately 0.8 Mtpa of CO_2 from a cement factory and a waste-to-energy facility in eastern Norway (IEA, 2021). Following capture, the CO_2 will be compressed and liquefied at each site and transported by specially designed ships to a temporary storage location in western Norway. Subsequently, it will be injected in a saline aquifer reservoir, situated about 110 km from the shore and 2.6 km beneath the seabed. The receiving terminal, offshore pipeline, and injection infrastructure, are designed for future expansion, accommodating over 5 million tonnes of CO_2 per year, with an anticipated total storage capacity of at least 100 million tonnes (CCUS Hub, s.d.).

2.4 CO_2 storage potential in Portugal and the PilotStrategy Project

Several geological environments have been studied in Portugal for CO_2 storage, including coal seams (COSEQ Project), mineral carbonation in ultramafic and mafic rocks (InCarbon (2018)), CO_2 hydrates in subseabed sediments (Bernardes, Carneiro, & Abreu, 2013), and DSA (Carneiro, Boavida, & Silva, 2011). Among these options, the choice of CO_2 storage in deep saline aquifers emerges as the most promising within the Portuguese geological landscape.

According to the Strategy CCUS project, the estimated total storage capacity of DSA in Portugal ranges between 3.54 and 14.14 gigatons (Gt) of CO_2, with a central estimate of 7.09 Gt. This storage capacity is distributed across eight clusters, one onshore and seven offshore: two clusters in the Porto Basin, three in the Lusitanian Basin (two offshore clusters, and one onshore), one in the Alentejo Basin and two in the Algarve Basin.

The majority of the storage potential lies in the Lusitanian Basin having an evaluated capacity in the offshore units of 2.93 Gt CO_2, surpassing the evaluated onshore capacity of approximately 260 Mt CO_2. Offshore storage units predominantly occupy the shallow continental shelf, positioned close to the coastline, representing an advantageous location concerning the main CO_2 emission sources in Portugal. The reservoirs within the Torres Vedras Group (Lusitanian Basin) exhibit the most significant storage potential (Pereira, Ribeiro, & Carneiro, 2021).

The surge in research initiatives and projects related to carbon sequestration in Portugal underscores the growing recognition of the importance of mitigating CO_2 emissions for both national and global sustainability. Previous projects such as KTEJO (2011) - particularly focusing on the Pego coal-fired thermoelectric power plant - and COMET (Boavida, 2011) - defining an integrated transport and storage infrastructure in Portugal, Spain, and Morocco, have played a crucial role in assessing the technical and economic feasibility of sequestering CO_2, considering the cost optimization of the entire CCS chain.

The strategic initiatives, including the CCS National Roadmap and Strategy CCUS Project, studied the role this technology could play in the Portuguese context in a low carbon economy scenario. The CCS National Roadmap proposed a Roadmap for Portugal (Seixas, et al., 2015), addressing themes such as public perception, costs and business models, transport, and storage risks, while Strategy CCUS Project, reflects a strategic plan to develop a CCUS network in southern and eastern Europe with the primary focus in Portugal being on regions with a high density of industrial CO_2 sources. Furthermore, the InCarbon Project, investigates the potential of CO_2 storage in mafic/ultramafic rocks from the Alentejo region and COSEQ Project (Lemos de Sousa, Rodrigues, Diogo, & Jesus, 2010) studies previously mined coal seams for potential storage, emphasizing the importance of assessing diverse geological environments to maximize storage potential.

Collectively, these projects contribute to shape a future where Portugal actively participates in global efforts to address climate change by exploring, assessing, and strategically implementing CO_2 geological storage technologies.

The research project "PilotStrategy” aims at investigating the potential of this technology by studying the CO_2 storage capacity in France, Portugal, Spain, Greece, and Poland. The main objectives include studying deep saline aquifers that offer significant CO_2 storage capacity, identifying safe and effective pilot storage sites, and engaging citizens and stakeholders throughout the project while exploring the social acceptance of CCS (https://pilotstrategy.eu/). The PilotStrategy project focuses on advancing knowledge regarding the use of deep saline aquifers for CO_2 geological storage in five European regions and has currently been developing a detailed investigation of saline aquifers in three distinct basins: the Paris Basin (France), the Lusitanian Basin (Portugal), and the Ebro Basin (Spain). The project aims to achieve a sufficient level of characterization in these regions by its conclusion, facilitating informed final investment decisions. To ensure the viability of CCS as a mean to mitigate climate change for both industries and local communities, additional research, political support, and social acceptance are considered essential. The project concentrates on deep saline aquifers – porous rock formations saturated with brine over a kilometer deep. Although deep saline aquifers exhibit promising potential for substantial CO_2 storage capacities, these have remained relatively unexplored in the context of CCUS until now.

In Portugal, the project is led by the University of Évora, responsible for tasks related to geocharacterization, risk analysis, and safety and performance analysis. Previous projects in Portugal (Strategy CCUS) were responsible for the analysis of technical, geological, and economic characteristics which led to the identification of two areas with potential for geological storage in the central/western region.

PilotStrategy stands out as a pioneering initiative in Portugal due to its pragmatic goal of capturing CO_2 emissions from industrial sources considered "hard-to-abate". These emissions are particularly difficult to mitigate due to the absence of viable alternatives to avoid CO_2 emissions in these processes, as previously mentioned. The project's emphasis on the central/western region of Portugal is driven by the substantial number of industries classified as "hard-to-abate" in this area and where the captured CO_2 is stored in proximity to these industrial sources (Figure 5).

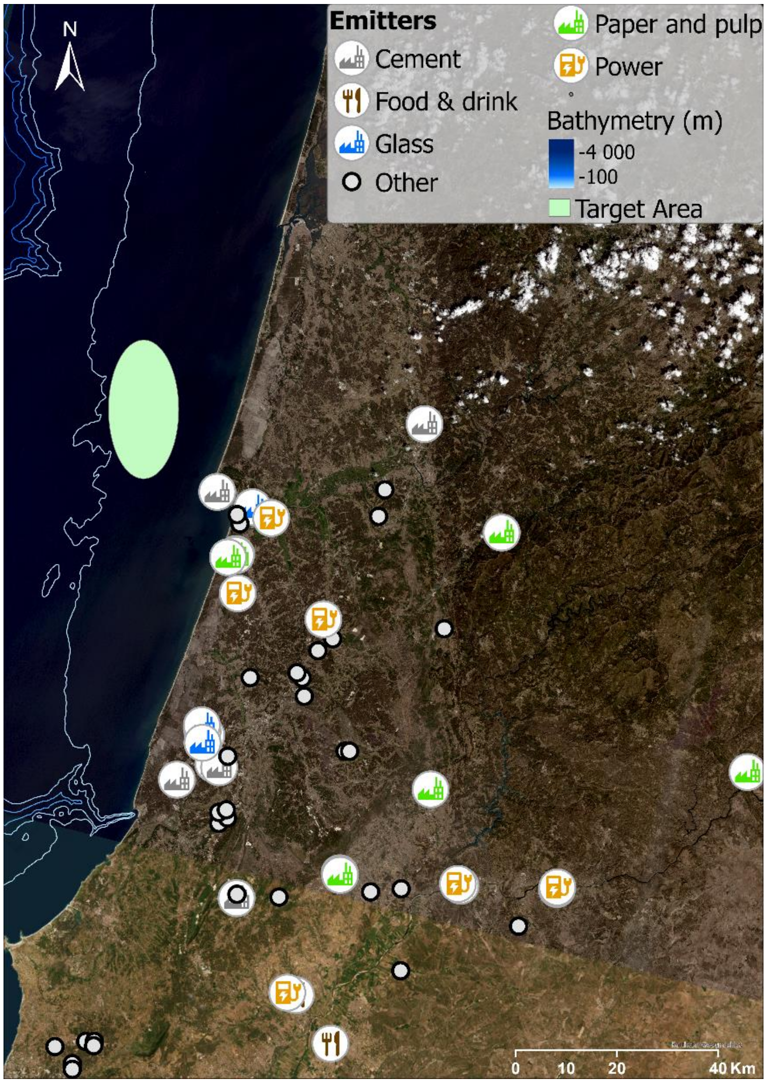

Figure 5- Emissions Sources central/western Portugal (Adapted From: (Carneiro & Mesquita, 2020)

2.5 The importance of fracture modelling for CO_2 geological storage

Fractures within geological formations have traditionally been recognized as potential paths for CO_2 escape, representing a substantial threat to storage site capacity (Bachu & Adams, Sequestration of CO2 in geological media in response to climate change: capacity of deep saline aquifers to sequester CO2 in solution, 2003). Areas with existing fractures reveal lower storage capacities and higher permeabilities compared to the surrounding matrix, enabling migration of CO_2 through the caprock. When CO_2 is injected, the density contrast between injected CO_2 and the formation brine water leads to buoyancy-driven upward movement, locating the CO_2 just below the caprock in cases of stratigraphic trapping. The effectiveness of CO_2 storage operations in saline formations relies on several factors, including dynamic capacity, which refers to the rate and pressure required for CO_2 injection, the static capacity of the aquifer, indicating how much CO_2 can be stored, and long-term security, involving the examination of potential CO_2 leakage.

These aspects present challenges that require careful attention when studying CO_2 geological sequestration. Therefore, it is imperative to evaluate caprock integrity thoroughly to strategically plan CO_2 storage locations and identify potential leakage pathways.

The impact of faults on subsurface fluid movement has been well-known. In the presence of faults near a CO_2 injection site, variations in pressures, temperatures, and injection rates can influence some of those factors. For instance, CO_2 injection induces pore pressure increases and reduces effective stresses, leading to changes in fracture apertures or fault slip and the generation of new fractures with hydraulic origins. These phenomena could compromise storage integrity and facilitate CO_2 leakage (Nicol, et al., 2017) (Figure 6). When faults behave as conductive pathways, CO_2 migration may occur if the buoyancy pressure exceeds the capillary pressure (Smith, Durucan, Korre, & Shi, 2011). CO_2 leakage through faults can pose risks, particularly when freshwater reservoirs are present in shallow formations. However, according to Smith et al. (2011), if there is no environmental harm, designing CO_2 storage sites in faulted areas, can help to dissipate injection volumes through fault zones to other reservoir layers. Besides environmental considerations, faults formed before CO_2 injection or reactivated during the injection period can influence storage capacity, maximum injection pressures and rates, and caprock integrity (Nicol, et al., 2017).

During the injection phase, when fluid pressures are at their peak and CO_2 is most mobile, preventing significant pressure increases at the well and in the underground storage formation is crucial to avoid rock fracturing or the activation of dormant fractures and faults.

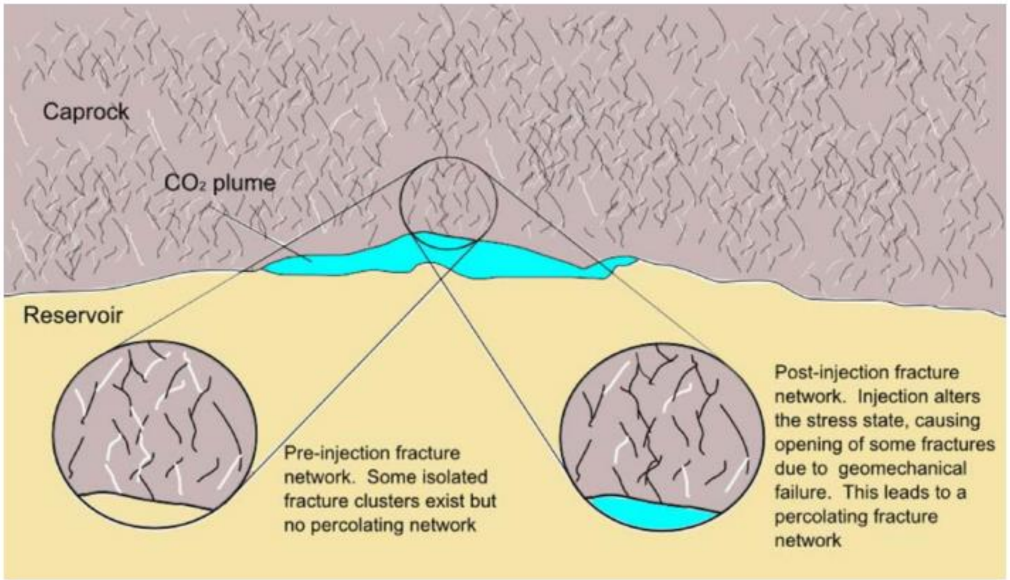

Figure 6- Injection influence on possible CO_2 migration through fracture networks Source: (Smith, Durucan, Korre, & Shi, 2011)

The structure of a fault zone depends on factors such as tectonics, depth of formation, magnitude of displacement and fluid flow. Traditionally, the fault structure comprises a fault core and a damage zone that surrounds it (Childs, et al., 2009) (Figure 7). In low-porosity rocks, composed of cohesive fine-grained materials in the core, the damage zone can have multiple scale fractures distributed along the fault (Faulkner, et al., 2010). In high-porosity rocks like sandstones, fault cores consist of incohesive materials, and damage zones show deformation bands which propagate, resulting in high permeability surfaces (Faulkner, et al., 2010). A previous study by Anders (1994) also found that in host rocks with low permeability, there is generally a decrease in fracture density as the distance from the fault core increases. On the other hand, in rocks with high permeability, microfractures resulting from deformation bands frequently don’t exhibit significant variation along the damage zone.

The damage zone widths are thought to be correlated with fault displacement. Previous studies indicate that the growth in damage zone width increases with displacement. However, after several hundred meters of displacement, the width-to-growth ratio decreases (Faulkner, et al., 2010). Fault zones play a crucial role in assessing the risk of CO_2 leakage as they can act as conduits for migration. In cases where fault zones have lower permeability compared to the host rock, they can behave as a seal, impeding lateral fluid flow. On the other hand, in tight rocks fault zones, higher permeabilities may act as fluid conduits for upward CO_2 migration (Faulkner, et al., 2010).

Generally, CO_2 may either seep along the fault zone or move across it. The presence of clay-rich (low-permeability) formations can prevent flow across the fault, while the clustering of fractures in the damage zone can facilitate flow along the fault. The importance of along-fault CO_2 migration increases when there is a higher density of small-scale fractures, a more extensive or interconnected fracture network, and/or a critically stressed fault. In along-fault flow, fracture connectivity is crucial for hydraulic conductivity. For instance, two fault zones with similar structures may differ in their ability to allow fluid flow depending on the presence of sufficiently connected high-permeability pathways (Nicol, et al., 2017). Ensuring the integrity of sealing formations is imperative for evaluating storage capacity. CO_2 leakage along potential high-permeability pathways represents an eminent geological hazard for CCUS, posing challenges to both technical feasibility and society acceptance of the technology (Zoback & Gorelick, 2012).

Overall, the internal structure, mechanical properties, and fluid flow within faults and the storage complex are intricately coupled, as documented in studies from several authors such as Faulkner et al. (2010), Bush and Kapmann (2018), Wang et al. (2021). These studies provide valuable insights into the characteristics and impacts of fractures, emphasizing the significance of this subject in order to have a reliable estimation of the long-term CO_2 storage.

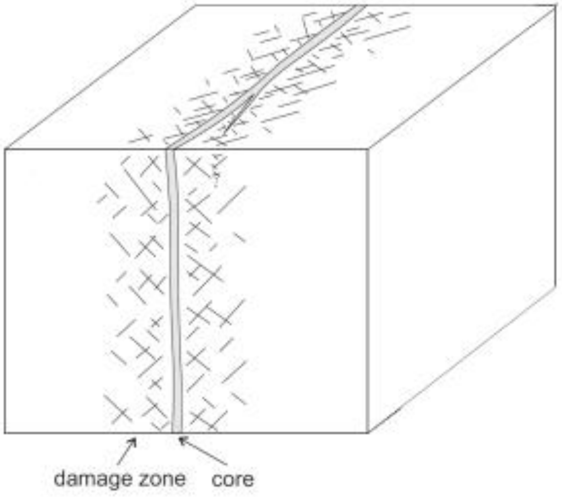

Figure 7- Common fault structure Source: (Childs, et al., 2009)

3 Case Study

3.1 Geographical Setting

Within the aim of the PilotStrategy project, an injection site for CO_2 was selected on the offshore of the Portuguese coast, which is the target area considered in this study (Figure 8). It is located near to the

Figueira da Foz port, in the central part of Portugal. The water column is approximately 80 m. This location is specifically convenient for injection CO_2 due to its proximity to main national CO_2 emitters (such as cement and pulp and paper).

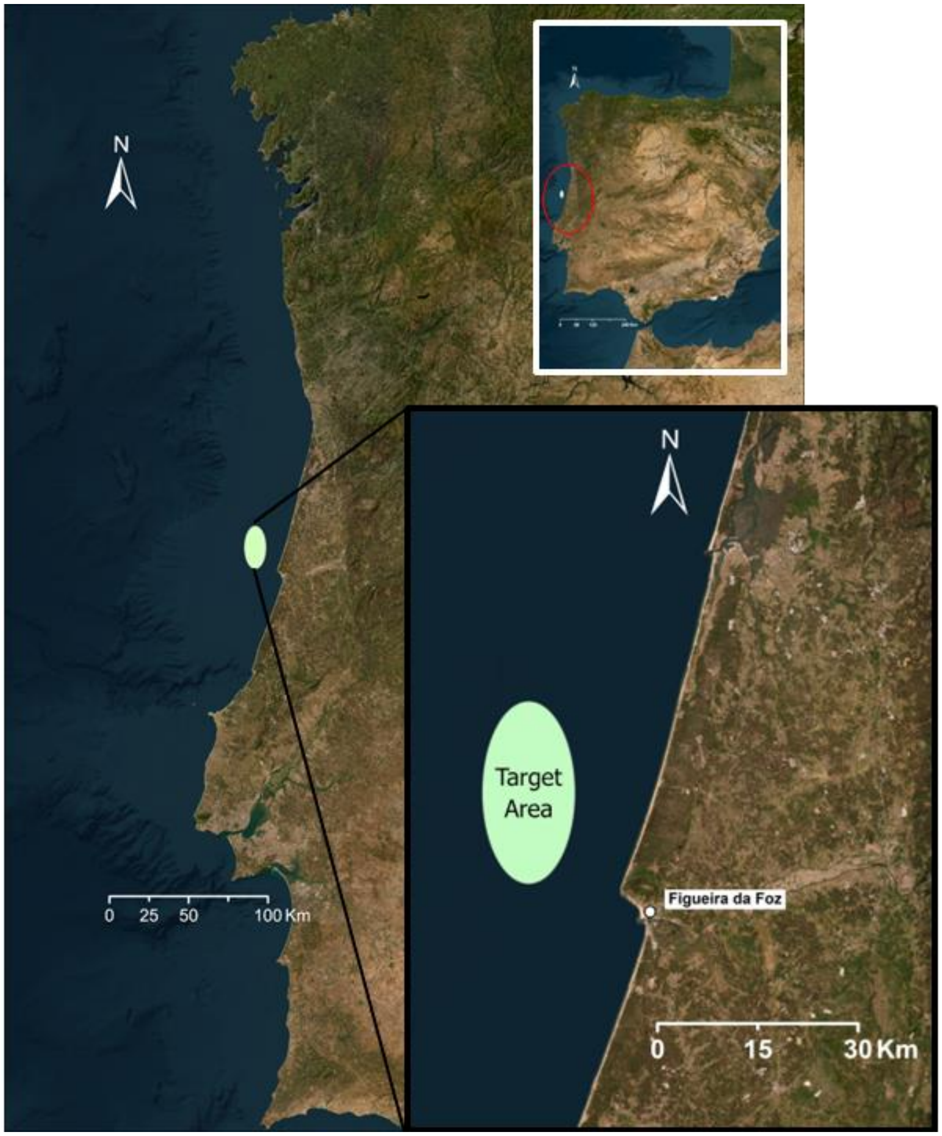

Figure 8- Study area location

3.2 Geological Setting

The geology of mainland Portugal is shaped by the Variscan orogeny, with the majority of the territory being composed of igneous and metamorphic rocks from the Paleozoic (mostly) and Proterozoic that constitute the basement of the Mesozoic sedimentary basins, developed during the break-up of Pangea and rifting phases of the Atlantic Ocean. Along the Variscan basement margins, several sedimentary basins have emerged. The main Mesozoic basins that can be observed in the West Iberian Margin include the Porto Basin, the Lusitanian Basin, and the Alentejo Basin. (Pinheiro, Wilson, Pena dos Reis, Whitmarsh, & Ribeiro, 1996)

The Lusitanian Basin (Figure 9), extending along the West Iberian Margin with a NNE–SSW trend, covers both onshore and offshore areas, with an approximate area of 20,000 km2 (Kullberg, et al., 2006) and a maximum thickness of about 6 km. Bounded by the 'slope fault system' to the west and the Porto-Tomar Fault to the east, this basin stretches from the town of Aveiro to the south of the Arrábida Chain. The western limit, in some instances, is also marked by horsts like the Berlengas Horst (Azerêdo, Duarte, Henriques, & Manuppella, 2003).

A sequence of rift episodes occurred between the Upper Triassic and the Lower Cretaceous times which contributed to the basin's formation. These episodes have been highly documented throughout the years by many authors, although its description and exact number of episodes has not always been in complete agreement:

- First Rift Phase (Upper Triassic-Lower Jurassic): Occurred within normal fault-bound half-grabens, evidenced by variations in thickness and depositional facies.
- Second Rift Phase (Lower to Upper Jurassic): Marked by the onset of marine deposition and a relative increase in regional thermal subsidence.
- Third Rift Phase (Upper Jurassic-Lower Cretaceous): Resulted in thick synrift sequences deposited in multiple sub-basin systems. Two distinct depositional stages were observed during this phase: (1) widespread carbonate deposition in lacustrine to deep-marine environments, followed by (2) the influx of marine to fluvial siliciclastic sediments. In the Lower Cretaceous, continental break-up followed by the North Atlantic Ocean opening, led to the deposition of a thick sequence of coarse-siliciclastic sediments (Pena Reis, Pimentel, & Garcia, 2010).

On the Lower Cretaceous time, a passive continental margin was formed in western Iberia, marked by oceanic accretion to the west (Kullberg, 2000). Significant geological transformations occurred from the Upper Cretaceous to the Upper Miocene time, due to the collision of the Iberia microplate with Eurasia or Africa plate, resulting in the reactivation of extensional faults formed in rift stages (Terrinha, et al., 2019).

The Lusitanian Basin exhibits two primary tectonic styles: one dominated by halokinetic structures and the other by faulting. These structures display NNE-SSW and NE-SW trends, identically to Hercynian basement faults. Several diapiric structures have developed over reactivated Hercynian basement faults, most of them near the coastline, where thick Lower Jurassic evaporites are found (Proença Cunha & Pena dos Reis, 1994).

The majority of the diapirs in the Lusitanian Basin, especially the larger ones, are located north of the Torres Vedras-Montejunto fault. The Dagorda Formation, mainly composed of evaporitic mudstones, plays a significant role in diapirism within the basin, with halokinesis (salt movements) also being linked to extensional and compressional episodes in the basin (Kullberg, 2000). The migration of evaporitic units resulted in the appearance of asymmetrical anticlines and the development of sub-basins with subsidence in the deeper parts of the Lusitanian Basin.

Proença Cunha and Pena dos Reis (1994) highlighted the importance of salt movements during various periods, emphasizing their significant role in the structural control of sub-basins and strongly influencing the sedimentary fill in the Lusitanian Basin. One of the periods often considered as key-moment of halokinetic activity is in the Upper Jurassic related to the second rifting episode.

Considering the Meso-cenozoic sedimentary outcrops extending through all the basin, Rocha & Soares proposed in (1984) the Lusitanian Basin's division into three sectors by major faults, each sector having distinct lithostratigraphic characteristics. This division was followed throughout the years, and it is still documented in more recent research (Rasmussen, Lomholt, Andersen, & Vejbæk, 1998); (Kullberg, 2000); (Kullberg, et al., 2006); (Pena Reis, Pimentel, & Garcia, 2010):

- Northern Sector: It is bounded by the Aveiro Fault to the north and the Nazaré Fault to the south, with Lower–Middle Jurassic and Cretaceous–Paleogene well preserved sequences.
- Central Sector: Defined between the Nazaré Fault in the north, and the Montejunto-Arrife Fault (onshore) and the Estremadura Spur (offshore) to the south. It reveals thick well-preserved Middle Jurassic outcrops, while Late Jurassic and part of the Cretaceous have undergone significant erosion.
- Southern Sector: Located in the south of the Estremadura Spur, also comprising well preserved sections from the Upper Triassic–Upper Jurassic time and part of the Tertiary.

In the research by Carneiro et al. (2011) the offshore area of the basin is emphasized as a potential location for CO_2 storage opportunities due to the morphology of the continental shelf and the thickness of Mesozoic and Cenozoic formations. Focusing on clastic rock aquifers, viable reservoir/cap-rock pairs were identified in the Lusitanian Basin.

Three potential CO_2 reservoirs are considered:

- Upper Triassic Clastic Layers (Silves Formation): Comprising fluvial and alluvial continental clastic deposits overlain by the Dagorda Formation, a thick sequence of marls, gypsum, and salt layers, which acts as an excellent seal.
- Upper Jurassic Siliciclastics (Lourinhã Formation or Gres Superiores): Composed of coastal clastic and slope sand deposits that exhibit lithological and thickness variations from north to south.
- Lower Cretaceous Sandstones (Torres Vedras Group): (Rasmussen, Lomholt, Andersen, & Vejbæk, 1998), (Azerêdo, Duarte, Henriques, & Manuppella, 2003), (Pena Reis, Pimentel, & Garcia, 2010) consists predominantly of sands and conglomerates deposited in a fluvial environment. The formation has a relatively constant thickness ranging from 300 to 400 meters, and exhibit porosities of up to 35% (DGEG, s.d.). Sealing mechanisms for these sandstones involve interbedded shale

and/or the presence of overlying Upper Cretaceous marls and marly limestones from the Cacém Formation (DGEG, s.d.). The Cacém Formation is mainly composed of limestones which were deposited in a shallow-marine carbonate platform environment (Kullberg, (2000)), acting as the primary cap rock.

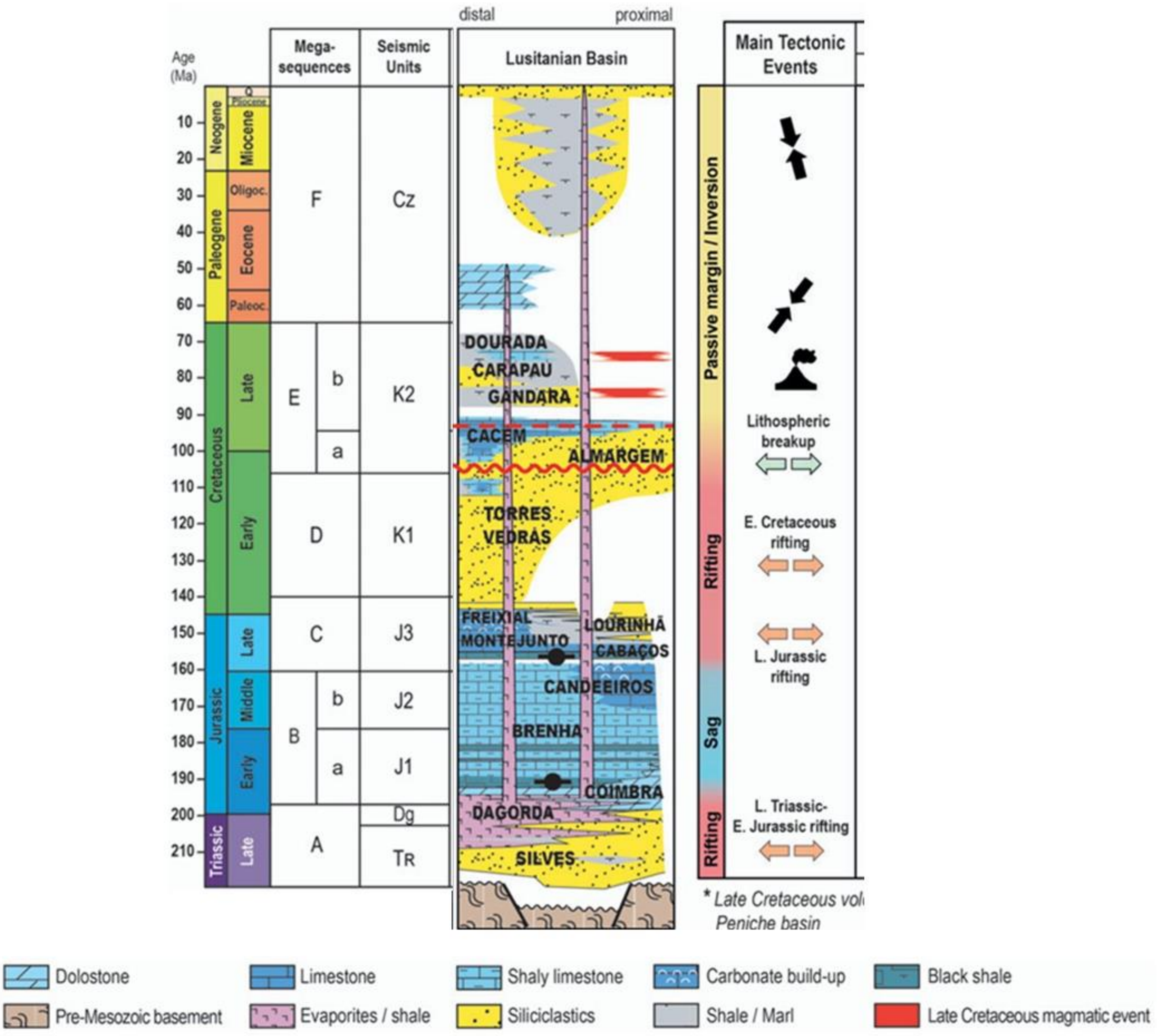

Figure 9- Chronostratigraphic chart of the Lusitanian Basin (adapted from: Casacão et al. (2023))

The potential storage complex (Figure 11) considered in this study involves the offshore TVG as the main siliciclastic reservoir, located around 860 meters below the surface, and the Cacém Formation (Figure 10) as the carbonate seal, with sedimentation dating from the Lower Cretaceous to Upper Cretaceous. The TVG presents very good porosities combined with the overall extension, making this unit the best reservoir target. (Marques da Silva, et al., 2023)

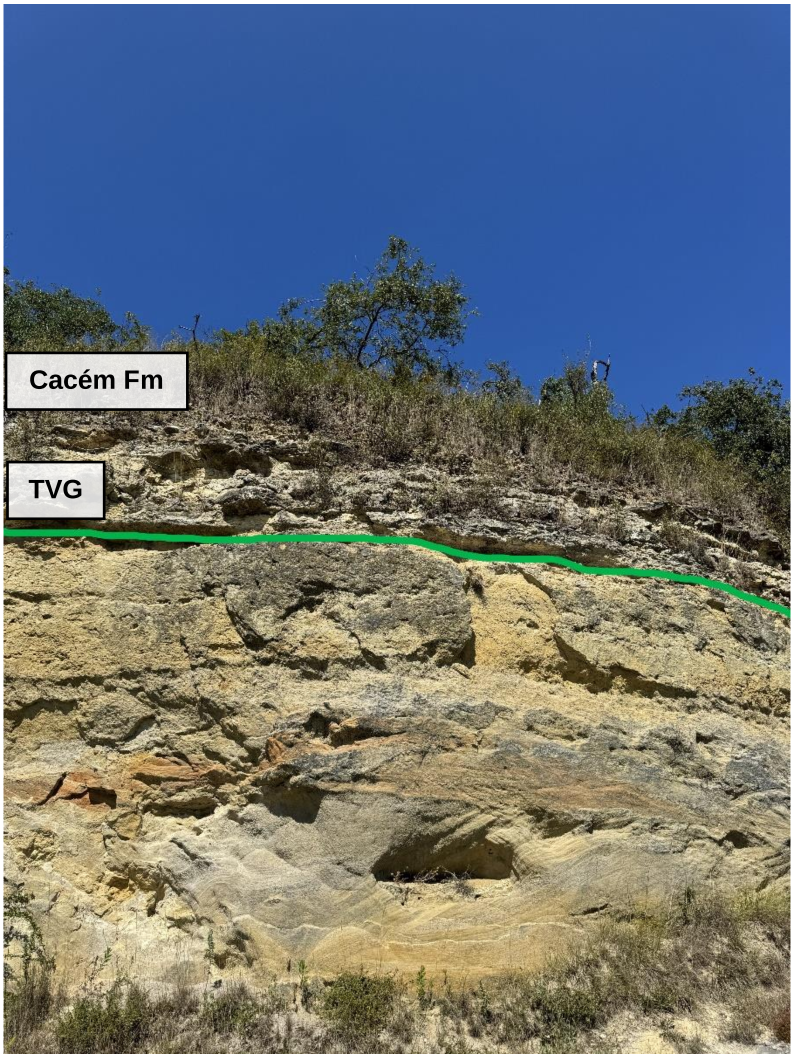

Figure 11- Reservoir (TVG) and Sealing (Cacém Fm.) Formations Outcrop

Figure 10- Cacém Formation Outcrop

3.3 Dataset analysis

Due to insufficient data in both quantity and quality for a robust analysis of the fractures in the study area, available information from nearby regions will be used. This dataset comprises the 3D Cabo Mondego, acquired by Mohave Oil & Gas in 2011, and several 2D seismic profiles from different two-way time (TWT) vintage multi-channel migrated seismic surveys, with a total length of 2950 km. (Figure 12) (Marques da Silva, et al., 2023) A vertical offshore well, located within the prospect area, was considered for the seismic resolution assessment. – Dourada (Do-1C). This well was originally drilled for petroleum exploration purposes during the 1970s and has limited data acquisition, exhibiting poor borehole quality.

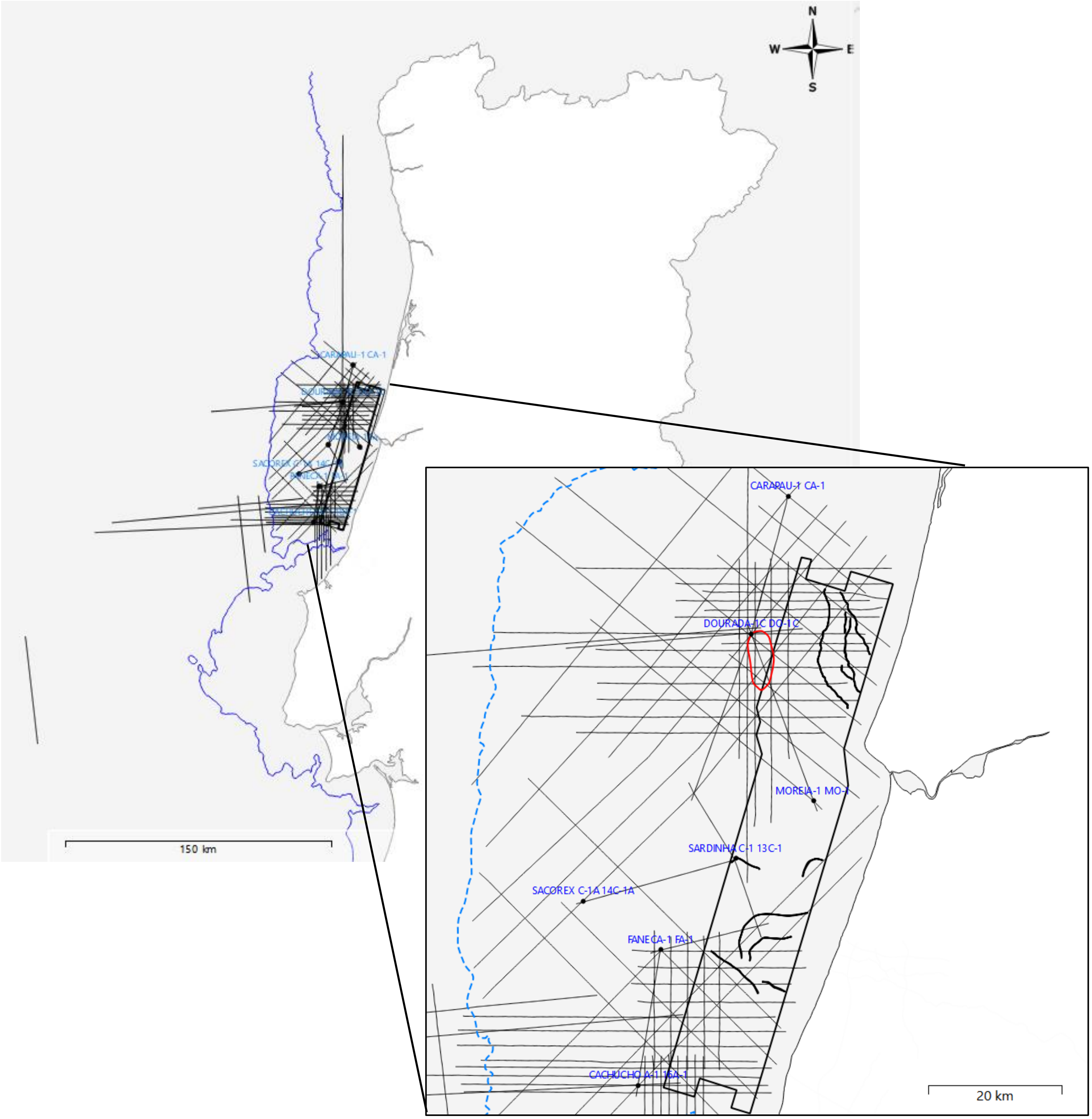

Figure 12- 3D seismic volume (bold) and 2D seismic lines in the study area

Additional to seismic data, also structural maps created in the aim of the PilotStrategy project were made available as part of the dataset. Structural maps highly contribute to the understanding of the study area by providing visual insights of the geological features, help to identify a suitable prospect location and serve as foundation to develop accurate 3D geological models. The map covers an extension of the offshore area that extends from the shore up to the continental platform break (dashed blue line on Figure 13) and considers not only the area of study (red polygon) but also the analogue areas used to the analysis of the fractures that are covered with 3D seismic. The 3D geological models that were subsequently developed in the aim of the PilotStrategy project are also utilized in this work as a grid, serving as foundation for building and analyzing the fracture models.

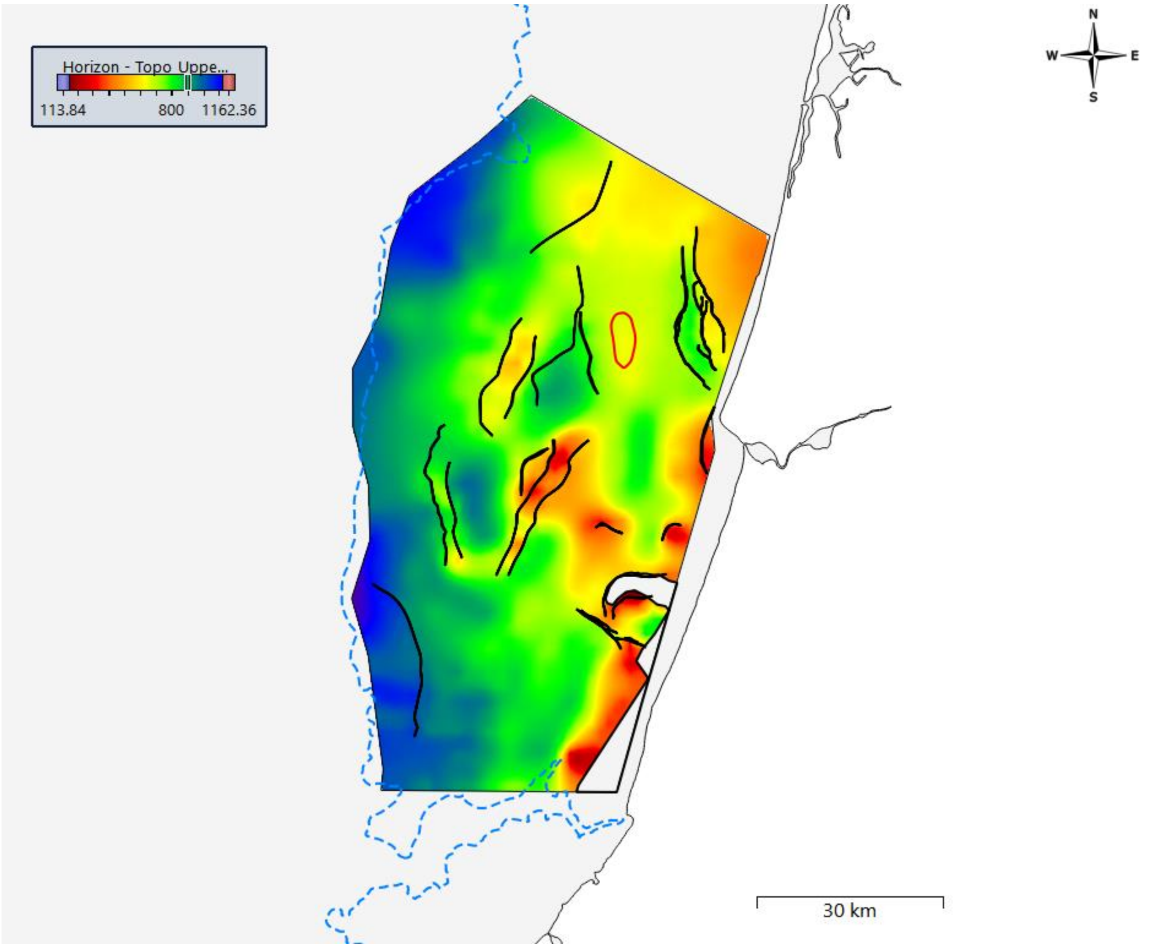

Figure 13- Cacém Formation structural map (in depth - meters) and Prospect (in red)

The essential data for the identification of fractures will be derived from a portion of the 3D seismic volume due to the poor quality of the 2D seismic lines where fractures identification is unfeasible. Although the 3D seismic volume only partially covers the prospect location, it will be the primary data source for this study. In contrast, 16 2D seismic lines intersect the prospect area, but their limited quality reduces the detail of the sections, making structures appear distorted or not even represented. (Figure 14). The 3D seismic volume (Figure 15) is located in the proximity of the area of study (on the NE as shown in Figure 12).

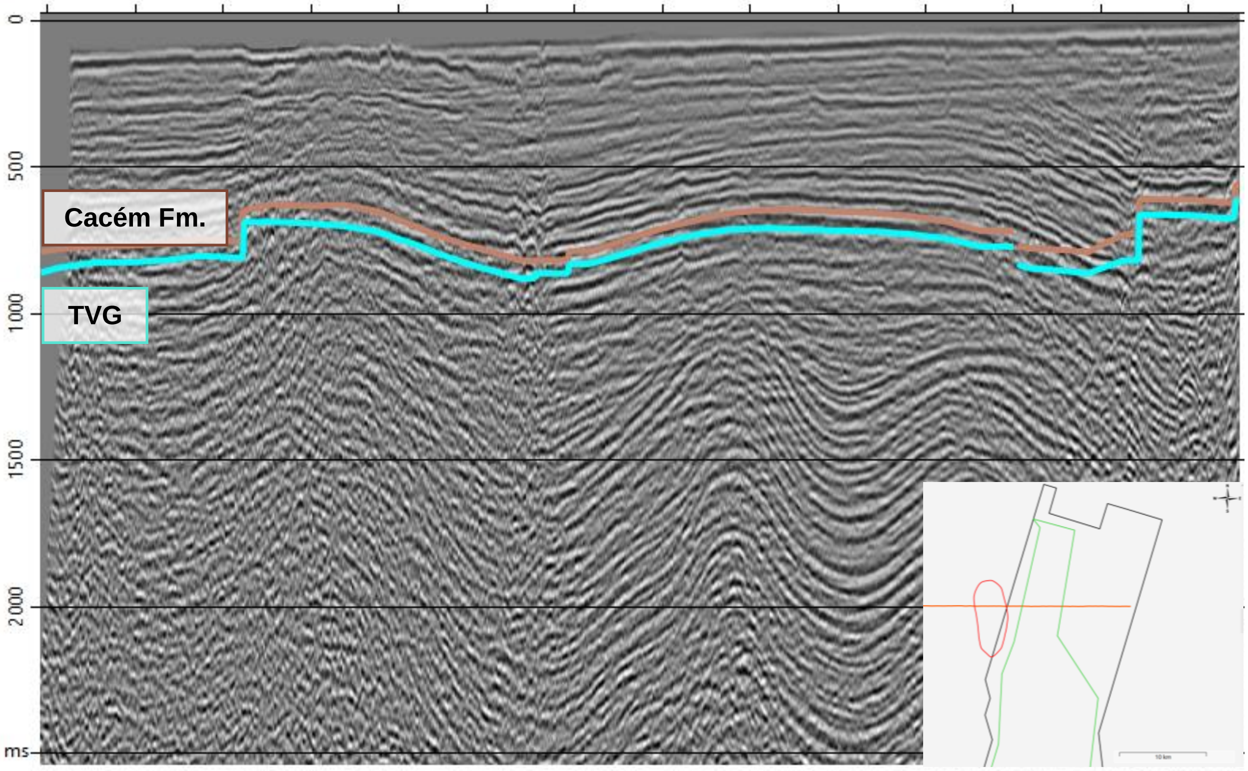

Figure 14- E-W seismic section (in ms) crossing the prospect (highlighted in red)

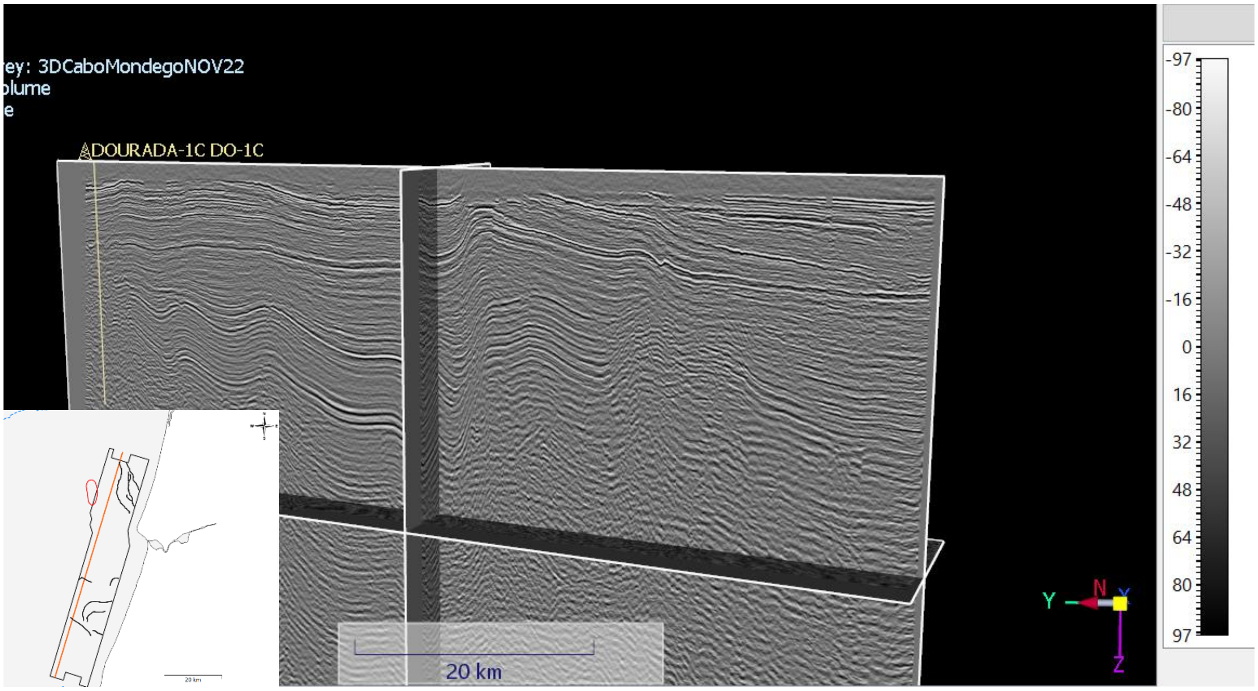

Figure 15- 3D sections with DO-1C well

In order to understand which structures would be possible to visualize in the data, an estimation of the vertical resolution was performed using the available data from the Dourada well.

Seismic resolution is the ability to distinguish between two features from one another. It indicates the minimum distance at which two interfaces can be identified as distinct reflectors. Vertical resolution is estimated as $\delta z \approx \lambda/4$, where λ is the "dominant wavelength":

$\lambda = V/f$

V: Interval velocity for Cacém Formation ≈ 4500 m/s (Figure 17); (obtained from well DO-1C)

Frequency range: 6-57 Hz; Dominant frequency ≈ 15 Hz (Figure 16);

Seismic Resolution ≈ 300/4 = 75 m

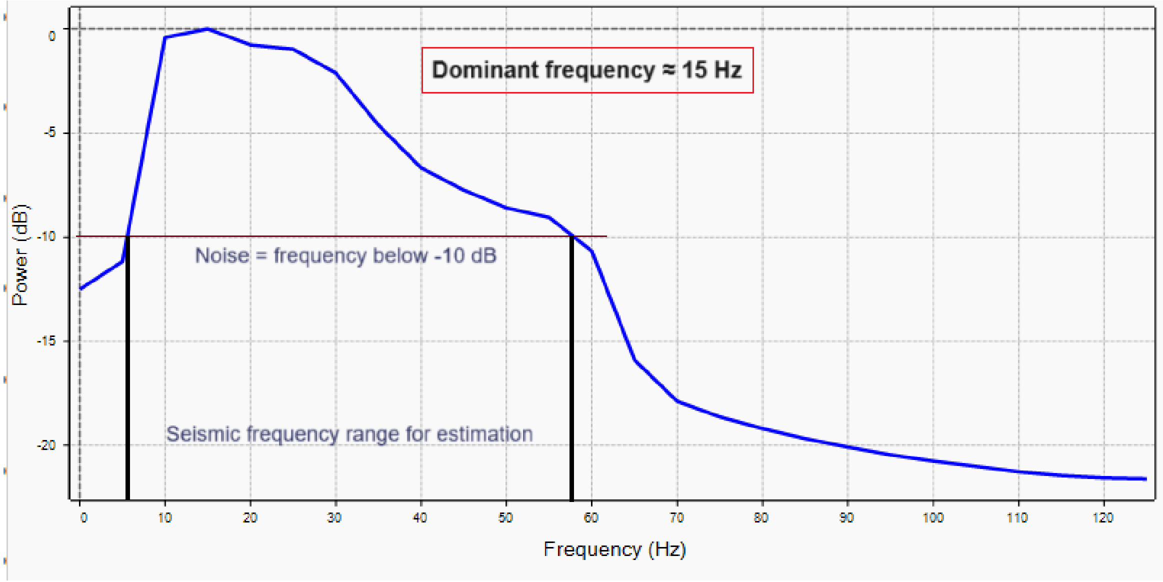

Figure 16- Frequency spectrum on Top Cacém Fm (≈ 660 ms)

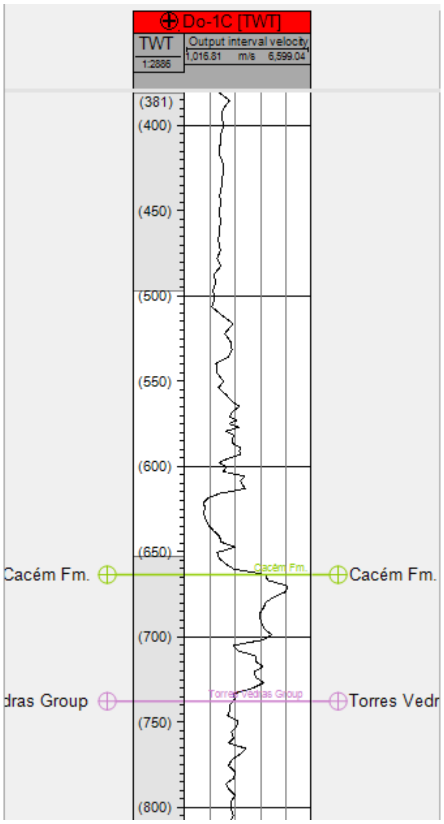

Figure 17- Interval velocity on Do-1C Well

4 Methodology

4.1 General Workflow

This section outlines the workflow (Figure 18) employed to achieve this study's goals. From the steps outlined below, the most significant ones are described in the following sections. Fracture identification represents one of the crucial steps, enabling the development of the fracture network models, while the characterization of these fractures has a key role in ensuring that the models are both reliable and robust. This process is essential for achieving the final step and most important objective of the work, the development of fracture network scenarios. The work involved the following steps:

1. Background - Study of the geological setting: A comprehensive study of the geological context of the area, with focus on Lusitanian Basin's northern sector, particularly on the Torres Vedras Group and the Cacém Formation.
2. Data Gathering and Quality Control: Gather pertinent data, evaluate its relevance, and ensure the reliability of the dataset. Estimate seismic resolution of the 3D volume.
3. Problem Statement: Define how to characterize fracture networks within the sealing formation.
4. Seismic Attributes Analysis: Identify which attributes can be useful for detecting fractures by adjusting various parameters in the computation process.
5. Fractures Identification: Relief attribute demonstrated effectiveness in revealing the presence of fractures. Variance attribute was also tested.
6. Modelling Software Testing: Utilize simulated data to explore software's functionalities.
7. Fractures Properties Characterization: Assess the variability of fractures proportions and distribution in the area.
8. Modelling Phase: Generate fracture scenarios for the reservoir sealing formation.

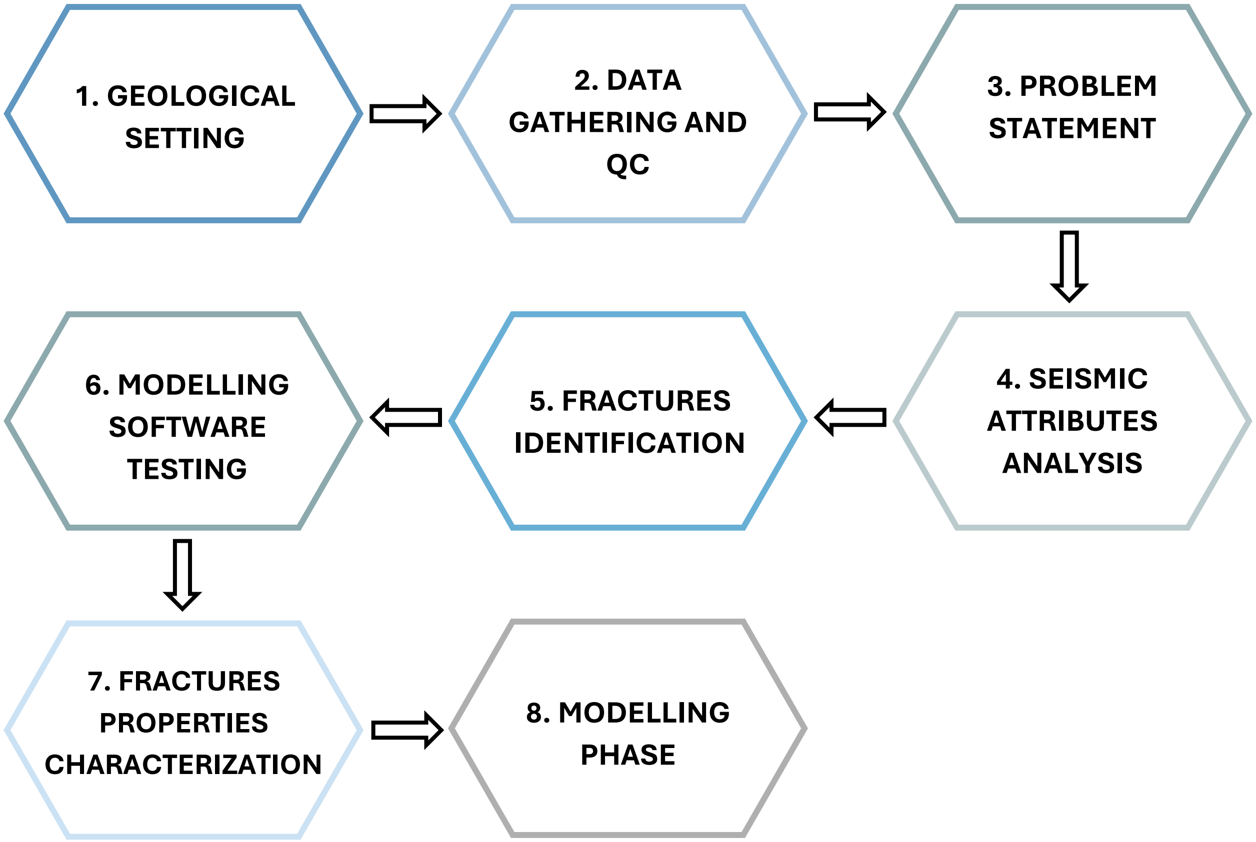

Figure 18- Methodology workflow

4.2 Seismic Attributes Analysis

Seismic attribute analysis can reveal hidden information within the seismic data, which is useful for prospects identification, depositional environments definition, and to detect and highlight discontinuities, contributing to understand the structural history of a region. In order to identify which seismic attributes can be useful for detecting fractures in this dataset, two attributes were computed in the seismic data (Figure 19):

- **Coherence attribute**, which measures the similarity of waveforms or traces given lateral and/or vertical windows (Chopra & Marfurt, 2007). Therefore, it can image discontinuities on seismic data related to faulting or stratigraphy. For this reason, a coherence cube was computed for the 3D volume of Cabo Mondego, while testing different values for two parameters: smoothing and inline/xline range. The initial range was of 3x3 while initial smoothing was 15. Other smoothing values used to test the attribute were 8 and 20 and an inline/xline range of 5x5. Although changes in the computation parameters were made, none of the combinations achieved the expected results of identifying fractures and for that reason, the attribute cannot be applied to this dataset for further work.
- **Relief attribute** which highlights impedance variations in the seismic data (Bulhões & Nogueira de Amorim, 2005). This attribute provided positive results and was used in the following steps of the work while coherence attribute failed to detect fractures, consequently being rejected.

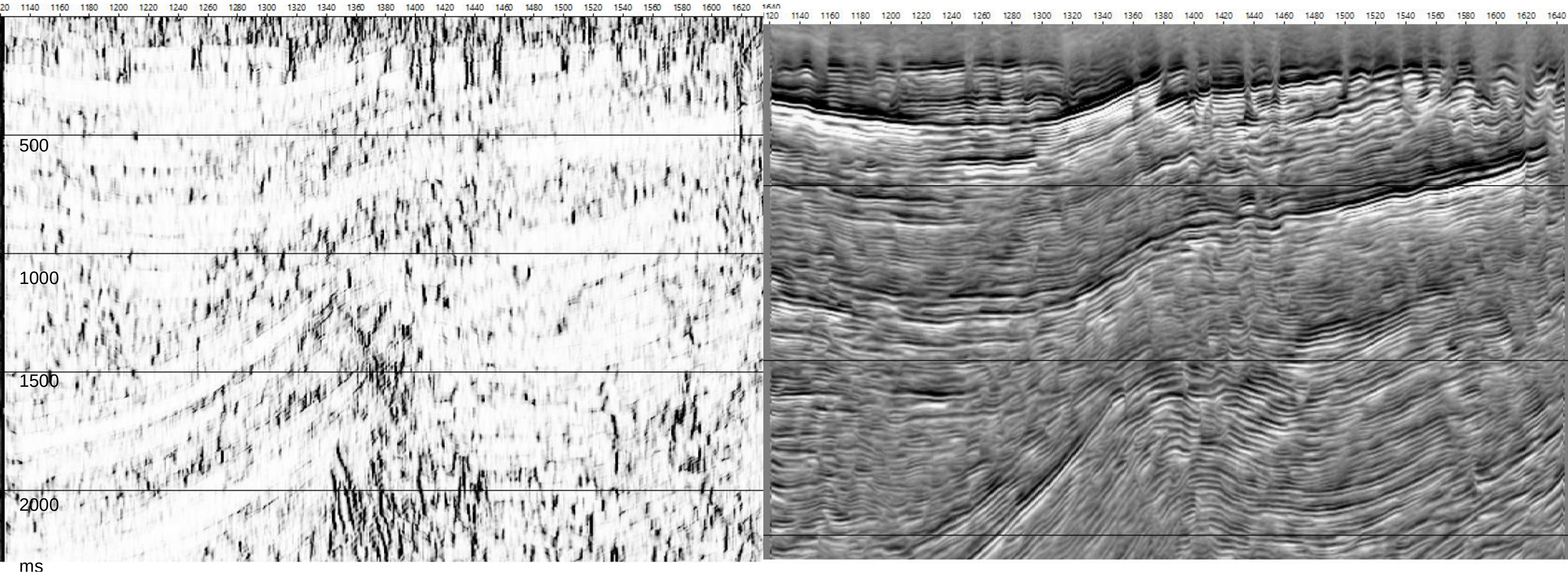

Figure 19 – Crossline 10875 with coherence attribute (left) and with relief attribute (right)

4.3 Fracture Identification with Relief Attribute

Fracture Interpretation

After testing two seismic attributes, Relief attribute demonstrated positive results for fracture identification (Figure 20). Consequently, an area within the 3D volume of Cabo Mondego was determined to perform fracture interpretation. The selected area excludes parts of the 3D seismic already interpreted in previous stages of the PilotStrategy project where major faults were identified.

Several seismic sections (crosslines and inlines) were analyzed while fractures were marked. Following this analysis, a classification was carried out in order to assess fracture's characteristics contributing to the next steps. The software utilized to conduct the fracture interpretation was again Aspen SeisEarth from Aspentech.

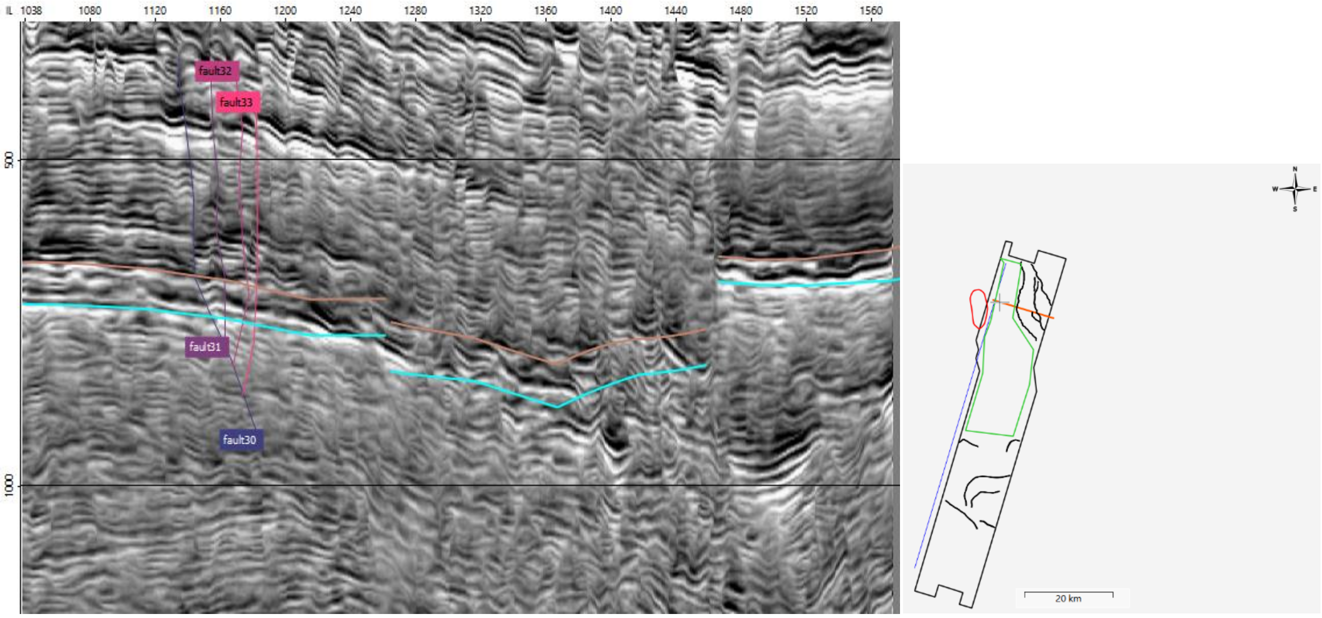

Figure 20- 3D Seismic Reflection Data with Relief Attribute

Fracture Classification

Fractures marked in the previous step were used to initiate the classification. The fractures were subsequently organized into four groups:

- Fractures which cross Cacém Formation and Torres Vedras Group
- Fractures which cross Cacém Formation but don't cross Torres Vedras Group
- Fractures which cross Cacém Formation, Torres Vedras Group and reach Seabed
- Fractures which cross Torres Vedras Group but don't cross Cacém Formation

Although the last class does not directly influence the sealing formation, fractures within the Torres Vedras Group can be connected to shallower fractures and fluid percolation can occur.

This classification is the first step towards the characterization of fractures in the considered area. Grouping fractures by a common characteristic is expected to contribute to assess the variability of fractures in the area.

Sections Selection

The chosen classification was then applied to specific seismic sections where fractures were identified. The sections (3 crosslines and 3 inlines approximately equidistant) were defined by relevance regarding the four classification groups as all the six sections exhibit the mentioned groups of fractures (Figure 21).

Figure 21- Selected 3D Seismic Sections (in orange) and following lines for interpretation (in dashed blue)

In these sections, all fractures from the four groups were marked and counted (showed on Appendix 1 to Appendix 6). Afterwards, one (or two) fracture groups were selected in each section to extend the interpretation to northern and southern sections (in the crosslines) and eastern and western sections (in the inlines), with the choice being primarily based on the identification of the fractures group that was easiest to follow its interpretation across further sections. Table 1 and Table 2 groups of fractures highlighted in green represent the groups chosen to extend interpretation. Figure 22 shows the fracture picks from all the identified fractures.

Table 1- Number of fractures identified in each Crossline

Xline	TVG/not Cacém	Cacém/not TVG	Cacém and TVG	Cacém, TVG, Seabed
14475	2	6	1	2*
12315	3	11*	8*	7*
10875	0	6	16*	14*

Table 2- Number of fractures identified in each Inline

Inline	TVG/not Cacem	Cacém/not TVG	Cacém and TVG	Cacém, TVG, Seabed
1420	0	5*	9*	7
1220	1	2	12*	10
1110	3	4	7	3*

---

* This group comprises “combined” fractures - two or more fractures apparently connected which are given the class that covers all the fractures within that gathering.

Figure 22- Fractures Identified in the Target Area

4.4 Modelling Tests

In order to get familiar with the modelling software and its functionalities, some tests were carried out using a synthetic dataset. The software used is a beta version of the AspenSKUA module v14.5 from Aspentech. Performing initial tests in the modelling software before computing the final models is a crucial step to ensure the efficiency and accuracy of the final outputs. These tests serve multiple purposes: besides contributing to the familiarization with the software's functionalities also allow to understand which parameters are needed to compute fracture models. Additionally, by working with a software's beta version, these preliminary tests also help to identify potential issues or limitations that could arise during the modelling phase. Each model consists of a set of ellipses defined by position, orientation angles, length, and height. Table 3 summarizes all the parameters utilized in this work with the available options for each one.

Table 3- Modelling Parameters Options

Parameters	**Options**
Length	Constant Value | Stochastic Approach
Strike	Constant Value | Stochastic Approach
Dip	Constant Value | Stochastic Approach
H/L Ratio	1: x (height = 1)
Intensity	Area per volume | Number per volume

Test models were computed for a reservoir grid developed in previous stages of the PilotStrategy project using Cacém formation (sealing formation) as target layer (Figure 23). Three models were created (Figure 24, Figure 25, and Figure 26), using different values of fractures intensity, length, orientation (strike and dip) and height/length ratio. The difference between test models and the final ones lies mainly in the fracture length (as a constant value was used, resulting in equal fracture lengths within each model) and in the fracture intensity (where each model was tested with three distinct intensity levels: low, intermediate, and high). The main difference, therefore, is the inclusion of relatively high intensity values, which were not observed in the actual data. All other parameters are similar to those identified in the fracture characterization. The three length values used in the test models are relatively close to real values, as well as the height/length ratio. Regarding orientation, only Model 3 is significantly different from reality, as most of the fractures identified in the area are subvertical. A summary of the utilized parameters is presented in Table 4.

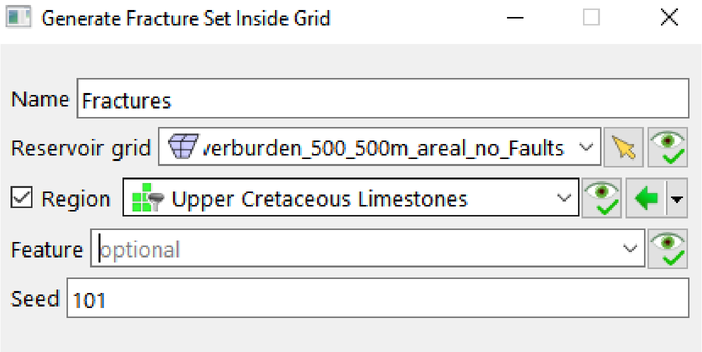

Name Fractures

Reservoir grid verburden_500_500m_areal_no_Faults

☑ Region Upper Cretaceous Limestones

Feature optional

Seed 101

Figure 23- Starting Modelling Parameters

Table 4- Testing Parameters

Tests	**Test 1**	**Test 2**	**Test 3**
Length (m)	200	500	1000
Strike	0º	90º	45º
Dip	90º	90º	45º
H/L Ratio	1:2	1:4	1:10
Intensity (/km3)	10	100	50

Test 1

Test 1 utilized a fracture intensity of 10 fractures per cubic kilometer, considering fractures of 200 meters length with N-S strike and 90º dip. These fractures have a 1:2 height/length ratio and aperture is not considered for this study.

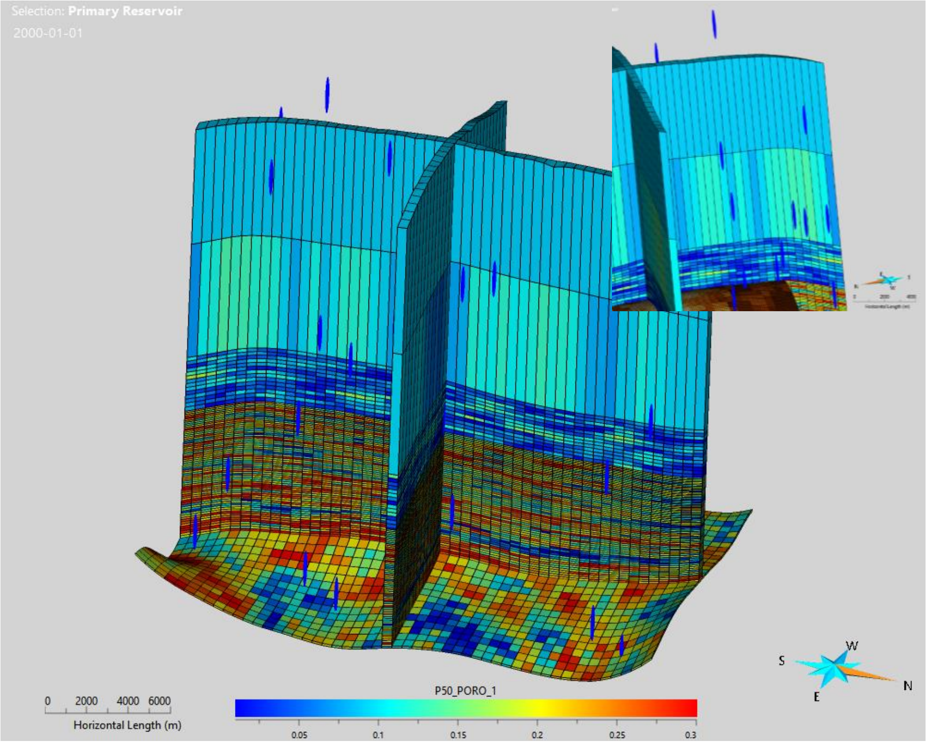

Figure 24- Test 1 Model

Test 2

Test 2 utilized a fracture intensity of 100 fractures per cubic kilometer, considering fractures of 500 meters length with E-W strike and 90º dip. These fractures have a 1:4 height/length ratio and aperture is not considered for this study.

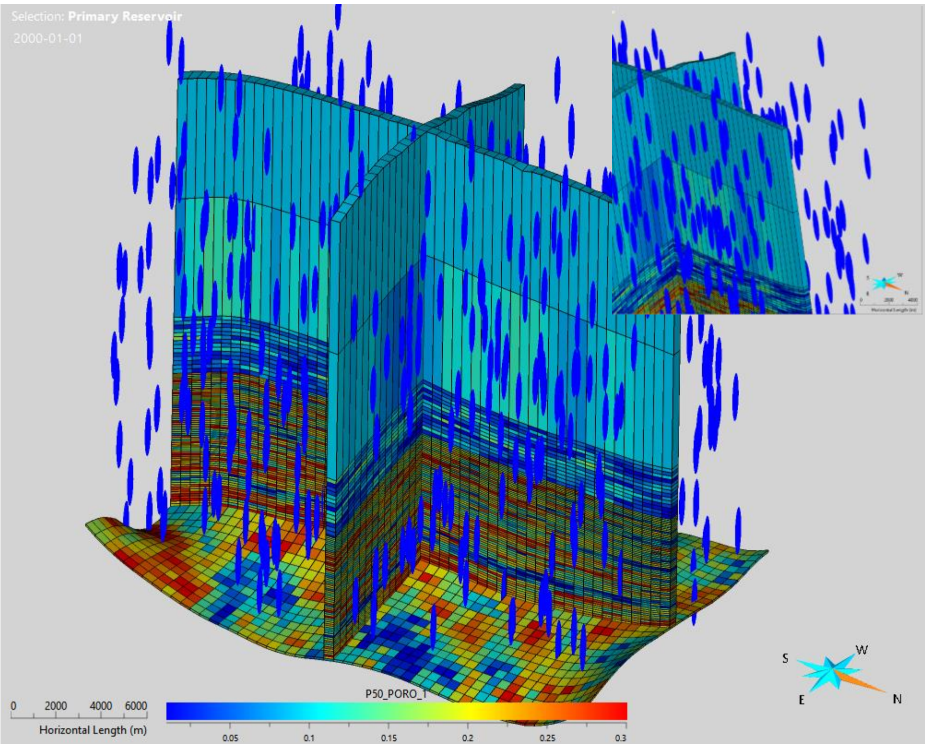

Figure 25- Test 2 Model

Test 3

Test 3 utilized a fracture intensity of 50 fractures per cubic kilometer, considering fractures of 1000 meters length with NE-SW strike and 45º dip. These fractures have a 1:10 height/length ratio and aperture is not considered for this study.

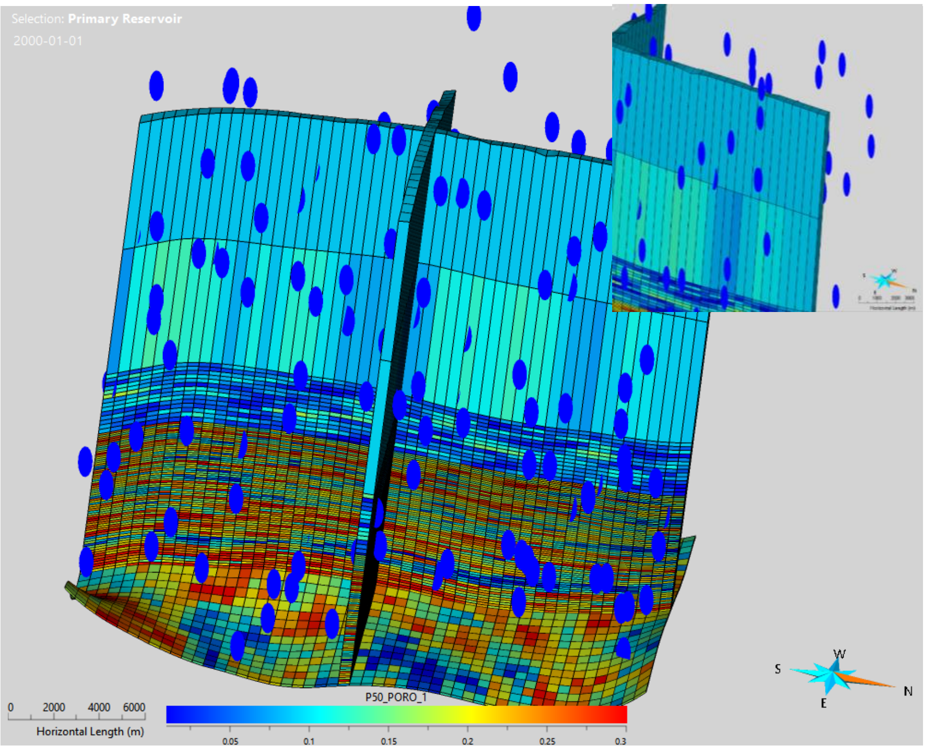

Figure 26- Test 3 Model

4.5 Fractures Properties Characterization

Following fractures interpretation, the characterization was carried out by applying a statistical approach. The statistical analysis utilized a statistical software named PAST4.17 (Hammer, Harper, & Ryan, 2001). The fracture characterization was conducted considering the key parameters required for the modelling process. This included analyzing the fractures' length, height, orientation (strike and dip), aspect ratio (height/length ratio of the fractures), as well as the fracture intensity within the area. The first step was to export the fracture files from the interpretation software, which are given as groups of points, corresponding to the interpretation picks. Each point has x, y and z coordinates.

X, Y, and Z values, which were obtained from the fracture picks' coordinates from each fracture interpretation are demonstrated in Table 5. After calculating a delta value of X, Y, and Z for each fracture, a single value was obtained for the three variables, presented in meters (Table 6). This step represents the foundation to perform the fracture characterization as most of the needed parameters were assessed by considering the delta X, Y, and Z values of each fracture.

Table 5- Fracture Picks Coordinates (Ftest2_18 example)

		X	Y	Z
INLINE 1266	XLINE 12315	4453972.50000	498872.00000	734.16760
INLINE 1268	XLINE 12315	4453961.50000	498909.50000	767.40698
INLINE 1272	XLINE 12315	4453932.50000	499005.28125	802.61658
INLINE 1287	XLINE 12315	4453825.00000	499364.50000	883.69958

Table 6- Ftest2_18 Length Calculations

	dX	dY	dZ	c^2	comp (m)
Ftest2_18	147.50	492.50	149.53	286672.31	535.4178864

For modelling purposes, it is essential to assess how the data of each parameter is distributed and to compare and analyze the statistics for each dataset. The goal is to identify the most effective method to extract the modelling parameters while aiding in the assessment of the variability of fractures in the area of study. The fracture projections on a stereonet (Figure 27), along with the interpretation that was conducted, indicate the presence of two major families of fractures with distinct strikes – one with NNE-SSW strike and the other with ESE-WNW strike. As a result, these two families were characterized and modelled individually, in the subsequent steps, as outlined below. The results are presented in the Results Chapter.

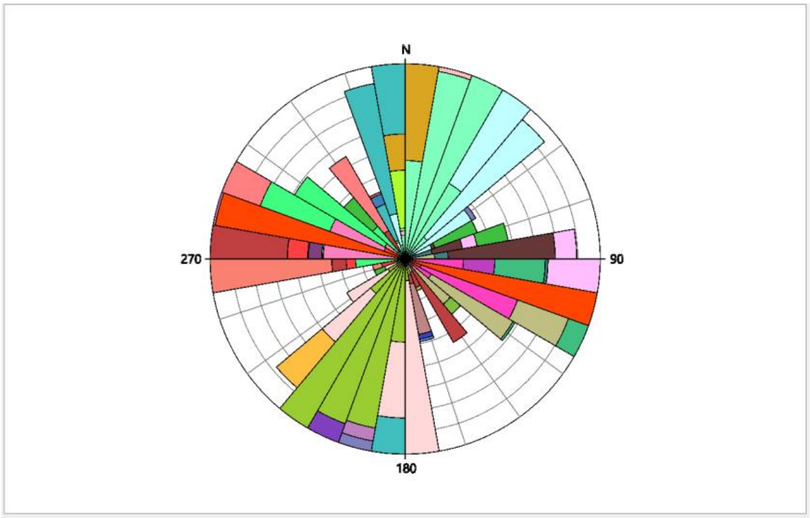

Figure 27- Fractures Projection on Stereonet

To perform the statistical analysis of the data, several steps were undertaken: histograms were analyzed, t-tests were performed to compare the means, and F-tests were applied to compare variances. In addition, normal-probability tests were conducted in some cases, along with Kolmogorov-Smirnov and Epps-Singleton tests, to compare the distributions between the two fracture families.

For the t-test, the p-value indicates the probability that the difference between means occurred by chance. If the p-value is below the considered significance level (0.05), it suggests that the difference between the samples' means is significant. The t-value and the t-critical value were also compared: if the t-value exceeds the critical value, the null hypothesis is rejected, and the means are considered different. Additionally, the Bayes factor was also used to interpret the results by quantifying the evidence for or against the null hypothesis. A Bayes factor greater than 1 shows evidence for the alternative hypothesis, while a value less than 1 favors the null hypothesis.

For the F-test, the F-value was calculated, comparing the ratio of the variances of the two samples. The p-value indicates the probability that the variance difference occurred by chance. If the p-value is below the significance level, the difference in variances is considered significant. The F-value was then compared with the F critical value: if the calculated F-value is larger than the F critical value, the null hypothesis (variances are equal) is rejected, indicating that the variances between the two samples are significantly different.

Regarding the Kolmogorov-Smirnov and Epps-Singleton tests, in both tests, the p-value provides the probability that the difference between the sample's distributions occurred by chance. If the p-value is smaller than the significance level, the test indicates that the distributions are significantly different, otherwise, they are considered similar.

Fractures Length:

Fracture length was initially calculated using the following equation (Equation 1):

$$c^2 = \Delta x^2 + \Delta y^2 + \Delta z^2$$

Equation 1- Fracture Length Formula

Fractures length input parameter admits a stochastic approach, therefore a suitable probability distribution was utilized as input. After being statistically analyzed, fractures' length observations seem to follow a lognormal distribution in both families. Although some outliers were identified they were considered in the analysis as they represent realistic length values.

Fractures orientation:

Fracture orientation (dip and strike) was extracted from AspenSKUA software after the fractures being displayed on a stereonet, with all strike values rescaled from 0 to 180º. This parameter also admits a stochastic approach, allowing a strike and dip distributions as inputs. After analyzing each variable, both strike and dip observations appear to follow a uniform distribution in both families.

Regarding the strike an approximation was made for both families to determine a representative range of strikes. Strike values were displayed in two tables to facilitate visualization (Table 7 and Table 8):

- 65% of the ESE family strikes range from 106º to 108º having 73% of the samples around 107º. For modelling purposes was considered a range from 106º to 108º as limits of the uniform distribution.
- 70% of the NNE family strikes range from 12º to 17º, having 76% of the samples around 17º and 24% of the samples ranging between 12 and 16º. For modelling purposes was considered a range from 12º to 17º as limits of the uniform distribution.

Table 7- ESE Family Strike Observations

8	9	12	13	14	15	16	17	21	24	26	28	31	37	38	40	43	44	60	63	65	67	70	72
1	1	2	3	3	1	2	35	1	1	1	1	1	2	1	1	2	1	1	1	1	1	1	1

Table 8- NNE Family Strike Observations

76	86	91	95	99	101	102	103	105	106	107	108	109	110	111	112	113	115	121	122	128	129	150	153	168	180
1	1	2	1	2	1	2	2	3	11	43	5	2	2	1	1	2	1	1	1	1	1	1	1	1	1

The same approach was conducted for dip values to determine a representative range for both families:

- 60% of the ESE family dips range from 75º to 90º (Table 9). For modelling purposes was considered a range from 75º to 90º as limits of the uniform distribution.
- 60% of the NNE family dips range from 85º to 90º (Table 10). For modelling purposes was considered a range from 85º to 90º as limits of the uniform distribution.

Table 9- ESE Family Dip Observations

13	14	23	27	30	32	37	38	39	41	43	44	48	49	51	53	56	58	59	63	67	68	69	70	71	73	74	75	77	78	79	81	83	89	90
1	1	1	2	2	1	1	1	1	1	1	1	1	2	1	1	3	1	1	1	2	1	3	2	1	2	1	3	2	1	1	1	1	18	27

Table 10- NNE Family Dip Observations

28	32	38	40	45	48	53	54	59	65	66	69	73	74	75	77	78	79	80	81	82	83	84	85	86	90
1	1	1	1	1	1	1	1	2	2	1	1	1	1	1	2	1	1	1	1	1	1	3	2	2	34

Fractures Aspect Ratio:

The statistical analysis of the Aspect Ratio (or height/length ratio) allowed to understand the samples' heterogeneity. Initially, the height/length ratio was computed based on the previously calculated length and height, with the last one corresponding to the Z value. By analyzing the histograms for each family, it was possible to conclude that the height/length ratios (H/L) did not fit a single-mode distribution. To address this, different mixture models were tested using histograms to find an appropriate fit for each family of fractures. Tests for multi-modal distributions were performed, using normal mixture models with 2, 3, or 4 modes.

The next approach was to plot the observations and identify a suitable distribution. The PAST4.17 statistical software offers built-in functions to create regression models, allowing the user to select from various pre-existing options to fit the data. The available regression models include linear, quadratic, exponential, power, von Bertalanffy, Gompertz, Hill's equation, logistic, and Michaelis-Menten. For the analysis, the models to be tested were chosen based on the highest R^2 values, indicating the best fit. Initially, an attempt to use a suitable model for both families was conducted but was unsuccessful. For the ESE family, several models were tested, including the linear, Gompertz, Hill's equation, Michaelis-Menten, and logistic distributions, but none achieved an R^2 value higher than 0.35. Regarding the NNE family, the same models were tested, with none of them surpassing an R^2 value of 0.29. The same approach was then applied to each group within the families. The logistic model provided the best fit, although some groups of fractures gave similar results to the families when considered without grouping.

Due to the lack of an appropriate distribution for such diverse data, the chosen approach was to establish a worst-case and best-case scenario for each family of fractures. These scenarios are represented by the minimum and maximum possible ratios. To evaluate these, two linear models were utilized to limit the observations on an xy plot, where x represents length and y represents height (Figure 28 and Figure 29). By computing the regression slope, defined as $\frac{\Delta y}{\Delta x}$ the height/length ratio can be expressed as 1:x.

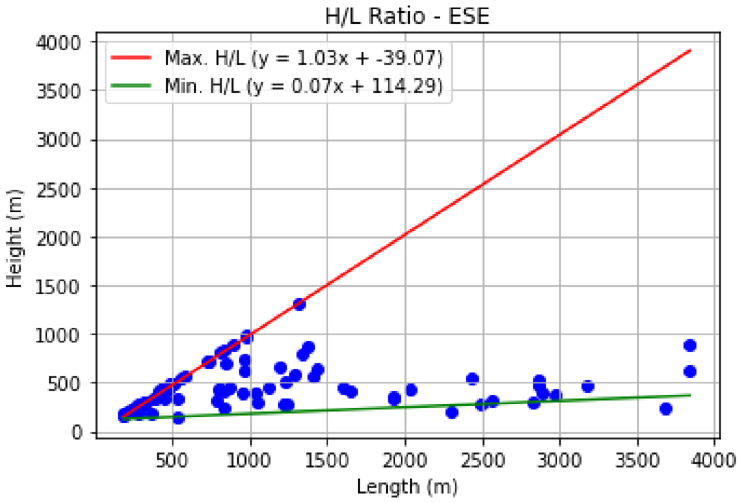

Figure 28- ESE Family H/L Plot

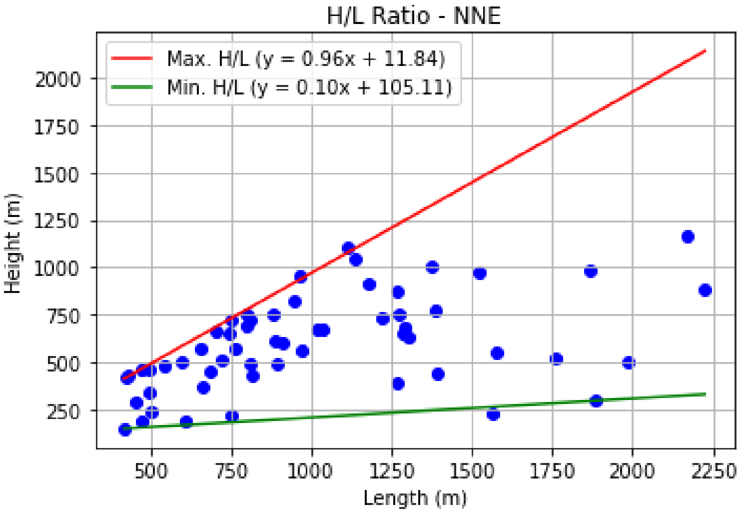

Figure 29- NNE Family H/L Plot

Assuming y = 1 the maximum and minimum ratios for the ESE family are calculated using both equations Equation 2, Equation 3):

$$\text{Max. ratio: } \frac{\Delta y}{\Delta x} = 1.03 \iff \Delta x = \frac{1}{1.03} = 0.97 \quad \rightarrow \text{ 1:0.97}$$

Equation 2- ESE max. ratio Linear Equation

$$\text{Min. ratio: } \frac{\Delta y}{\Delta x} = 0.07 \iff \Delta x = \frac{1}{0.07} = 14.29 \quad \rightarrow \text{ 1:14}$$

Equation 3- ESE min. ratio Linear Equation

Assuming y = 1 the maximum and minimum ratios for the NNE family are calculated using both equations (Equation 4, Equation 5):

$$\text{Max. ratio: } \frac{\Delta y}{\Delta x} = 0.96 \iff \Delta x = \frac{1}{0.96} = 1.04 \quad \rightarrow \text{ 1:1.04}$$

Equation 4- NNE max. ratio Linear Equation

$$\text{Min. ratio: } \frac{\Delta y}{\Delta x} = 0.10 \iff \Delta x = \frac{1}{0.10} = 10 \quad \rightarrow \text{ 1:10}$$

Equation 5- NNE min. ratio Linear Equation

Fracture Intensity:

In terms of fracture intensity, which was measured as the number of fractures per cubic kilometer, it was anticipated that the intensity would vary with depth. This happens due to the four groups of fractures that were identified during the interpretation, depending on which formations they intersected. To account for this, three vertical intervals were defined to measure fracture intensity: SB-C (between Seabed Top and Cacém Formation Top, C-TVG (between Cacém Top and Torres Vedras Group Top), and TVG-Alc (between Torres Vedras Group Top and Alcobaça Formation Top).

The fractures counted within each interval are related to the four previously defined groups of fractures (Seabed, Cacém and TVG, Cacém not TVG, and TVG not Cacém). For each interval, the following considerations were made based on which group of fractures could be observed:

- **SB-C**: includes fractures from the Seabed and Cacém not TVG groups.
- **C-TVG**: includes fractures from the Seabed, Cacém and TVG, and Cacém not TVG groups.
- **TVG-Alc**: includes fractures from the Seabed, Cacém and TVG, and TVG not Cacém groups.

Given that the number of fractures also varies significantly across the study area, the following approach was to divide the interpreted area into three large sections of equal size and count the fractures in each. After that, each of the large sections was divided into four smaller sections, and the fractures were counted again. This process was repeated by dividing the smaller sections into even smaller ones, having a total of 31 of the smallest sections, as shown on Figure 30. Finally, the number of fractures within each section was counted.

The sections were divided into equal-sized areas, with the largest sections having the same area among themselves, the smaller sections also sharing equal areas among them, and the smallest sections following the same pattern. Since certain regions contain a high concentration of fractures while others have lower concentrations, this method helps to better understand how fracture intensity varies laterally, depending on the section being analyzed, even though the sections have the same surface area.

The volumes of each section were then calculated (as illustrated in Figure 31) using the formations horizons (interpretated in previous stages of the PilotStrategy project) as top and bottom limits, having as result three values per section, corresponding to the three depth intervals mentioned above. Afterwards fracture intensity was determined as the number of fractures per section volume (results on Appendix 7).

Given the absence of a suitable distribution for the data, the chosen approach was to establish a worst-case and best-case scenario for each interval in both fracture families. These scenarios are again represented by the minimum and maximum possible value of fractures intensity and were used as input in the modelling phase.

Figure 30- Sections considered for Intensity Calculation, 3D Seismic volume (in black) and prospect (in red)

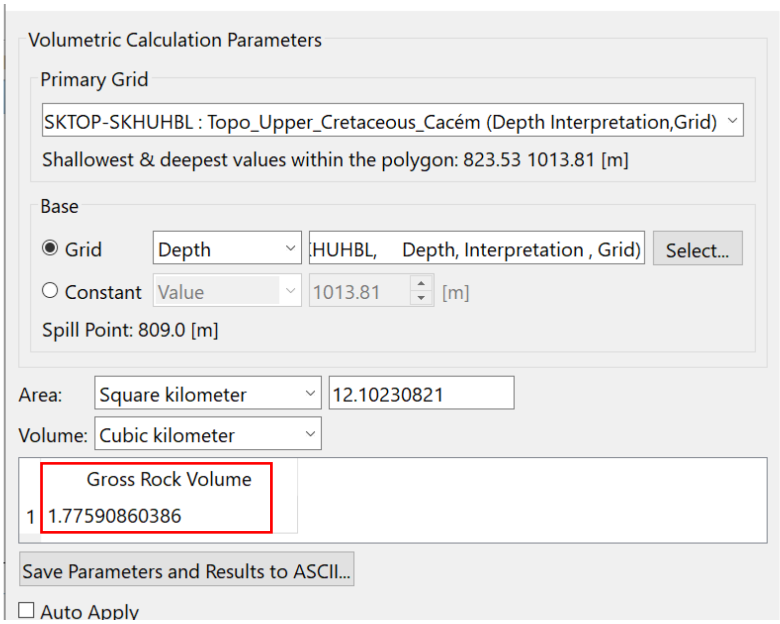

Volumetric Calculation Parameters

Primary Grid

SKTOP-SKHUHBL : Topo_Upper_Cretaceous_Cacém (Depth Interpretation,Grid)

Shallowest & deepest values within the polygon: 823.53 1013.81 [m]

Base

● Grid Depth :HUHBL, Depth, Interpretation , Grid)

○ Constant Value 1013.81 [m]

Spill Point: 809.0 [m]

Area: Square kilometer 12.10230821

Volume: Cubic kilometer

	Gross Rock Volume
1	1.77590860386

Figure 31- C-TVG interval volumetric calculation

Outliers:

In order to understand the role of outliers in the statistical analysis, it was crucial to determine if they impact the modelling parameters. The following section describes the method used to identify and evaluate outliers, contributing to decide whether they should be included or excluded from the analysis of each modelling parameter.

The method used to identify outliers was the Grubbs' Test. It calculates the "R" statistic, which is the standardized residual (how far each data point deviates from the sample mean in terms of standard deviation). The "Rcrit" is the critical value, which defines the threshold above which a value is considered an outlier.

The values where "R" exceeds "Rcrit" and $p < 0.05$ are detected as outliers (values highlighted in pink on Table 11). Values with "R" greater than the corresponding "Rcrit" indicate that the point is an extreme value, compared to the distribution of the data. If the statistical tests do not directly detect the highest values in a dataset as outliers based on residual calculations, values higher than those detected by Grubbs' test can also be considered as outliers. If lower values are outliers, it is reasonable to consider even higher values outliers as well, because they deviate even further from the data's tendency.

Table 11- ESE Family Length Outliers (Example)

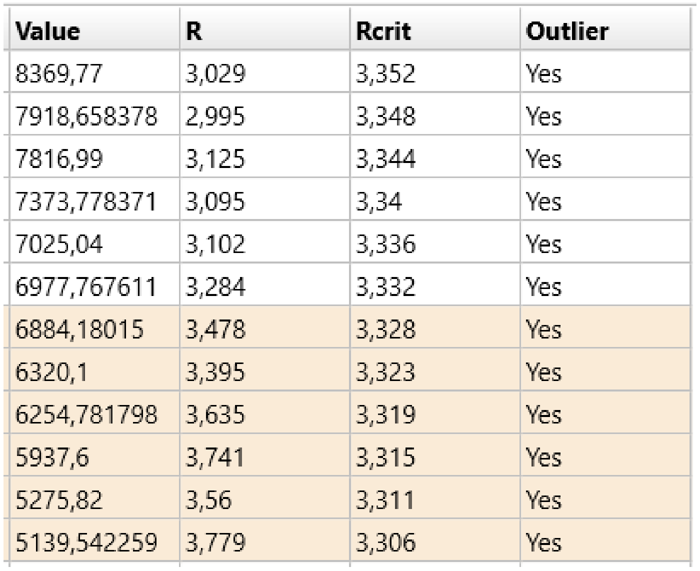

Value	R	Rcrit	Outlier
8369,77	3,029	3,352	Yes
7918,658378	2,995	3,348	Yes
7816,99	3,125	3,344	Yes
7373,778371	3,095	3,34	Yes
7025,04	3,102	3,336	Yes
6977,767611	3,284	3,332	Yes
6884,18015	3,478	3,328	Yes
6320,1	3,395	3,323	Yes
6254,781798	3,635	3,319	Yes
5937,6	3,741	3,315	Yes
5275,82	3,56	3,311	Yes
5139,542259	3,779	3,306	Yes

5 Results and Discussion

5.1 Statistical Analysis

To perform the statistical analysis of the data, several steps were undertaken (considering each family of fractures separately for each parameter): histograms were analyzed, t-tests were performed to compare the means, and F-tests were applied to compare variances. In addition, normal-probability tests were conducted in some cases, along with Kolmogorov-Smirnov and Epps-Singleton tests, to compare the distributions between the two fracture families. This analysis revealed the following results:

Strike:

Fracture interpretation and fracture projections' analysis confirmed the existence of two major families of fractures with distinct strikes, being orthogonal with each other — NNE-SSW and ESE-WNW. This suggests that the fractures were formed during two separate tectonic events, although coeval development of both fracture sets cannot be discarded, in an extensional stress regime (Bai, Maerten, Gross, & Aydin, 2002). Consequently, these two families were characterized and modelled separately, as two different scenarios.

- The ESE family appears to follow a normal distribution centered in a very sharp peak (Histogram 1), being highly concentrated around 107º, with 18 outliers being values lower than 99º or greater than 113º.
- The NNE family appears to follow a normal distribution between 10º and 30º (Histogram 2), centered around 15º, with 13 outliers being values greater than 37º.

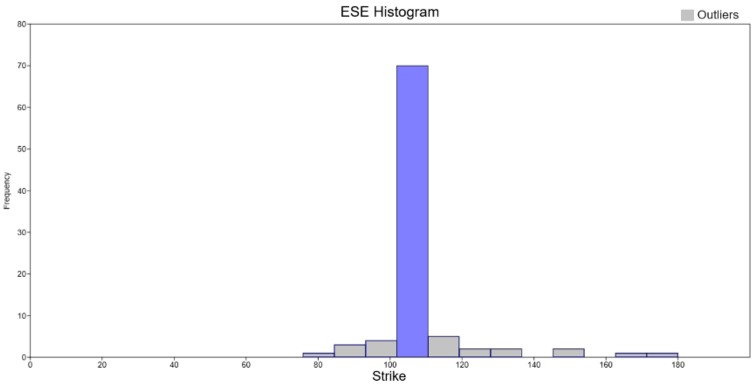

Histogram 1- ESE Family Strike

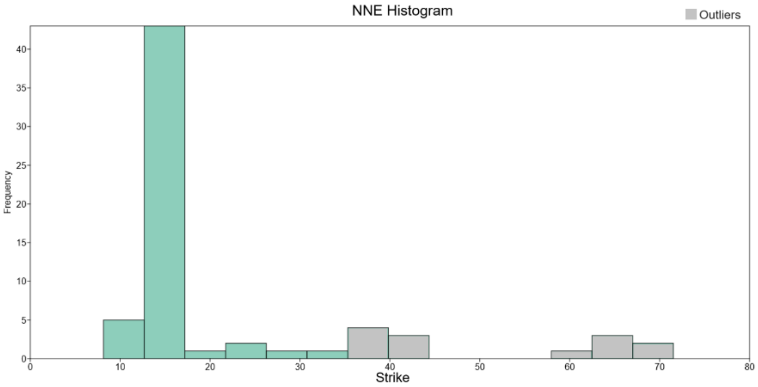

Histogram 2- NNE Family Strike

- After removing the outliers for both families and performing normality tests (Table 12) the Shapiro-Wilk and Anderson-Darling tests do not show normality results (p-value lower than the significance level of 0.05) combined with a normal-probability plot (Figure 32 and Figure 33) where the observations show significant deviations from the expected normal pattern, suggesting a non-normal distribution.

Table 12- Strike (without outliers) Normality Tests

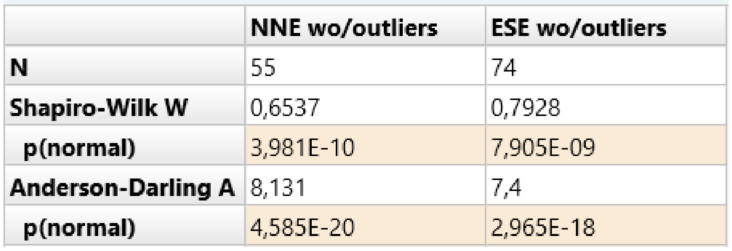

	NNE wo/outliers	**ESE wo/outliers**
N	55	74
Shapiro-Wilk W	0,6537	0,7928
p(normal)	3,981E-10	7,905E-09
Anderson-Darling A	8,131	7,4
p(normal)	4,585E-20	2,965E-18

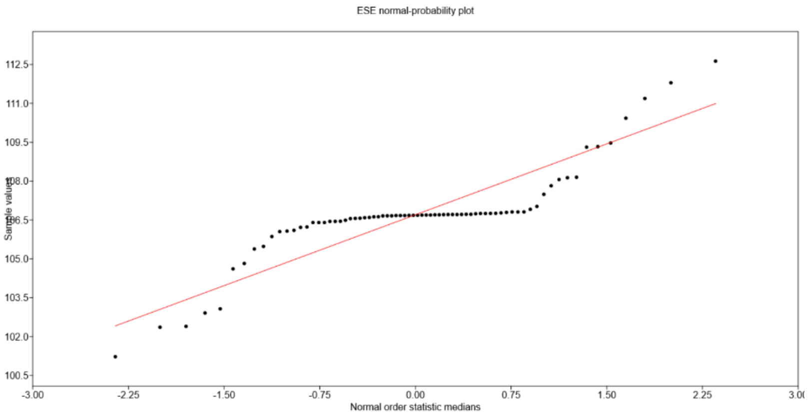

Figure 32- ESE normal-probability Plot

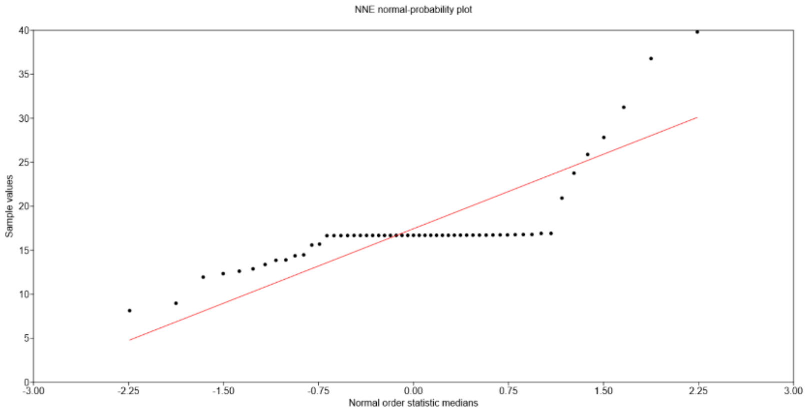

Figure 33- NNE normal-probability Plot

By analyzing the strike's histograms, both with and without outliers, it initially appeared that the strikes followed a normal distribution. However, after conducting normal tests (Shapiro-Wilk and Anderson-Darling), the results indicated the data did not satisfy the assumptions of normality, being necessary to adopt an alternative approach to simplify the data treatment. The simplification strategy involved defining a range of strike values for each family of fractures, based on the dominant strike ranges observed in the dataset. For instance, in the ESE family, 65% of the strikes fell between 106º and 108º, which led to the decision to use 106º-108º as the representative range for this family in the model. Similarly, for the NNE family, 70% of the strikes were clustered between 12º and 17º, resulting in 12º-17º being selected as the strike range. This simplification clarifies the modelling process by reducing the complexity of the data, while still capturing the most important trends. Although this method abdicates some of the finer details in the data, it ensures that the key characteristics of each family are preserved for modelling and interpretation.

Dip:

- Both families follow a uniform distribution, with the median value used to define the minimum and maximum values. The ESE family has a uniform distribution between 75º and 90º (Histogram 3) the NNE family ranges from 85º to 90º (Histogram 4). The ESE family has 18 outliers (values equal to or less than 51º), while the NNE family has 13 outliers (values equal to or less than 66º).

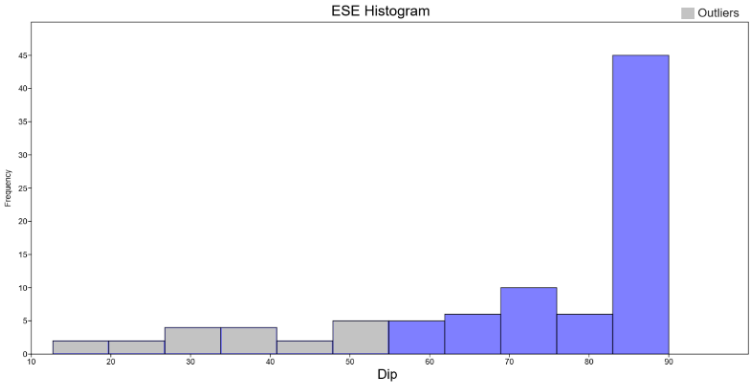

Histogram 3- ESE Family Dip

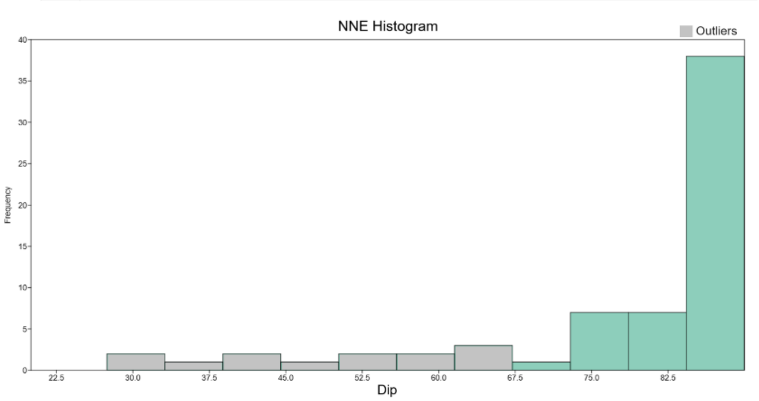

Histogram 4- NNE Family Dip

- The Kolmogorov-Smirnov test (Figure 34) is inconclusive regarding whether the two variables have similar distributions (p-value much lower than the significance level of 0.05), but the Epps-Singleton test (Figure 35) confirms that the two variables may have similar distributions (p-value greater than 0.05).

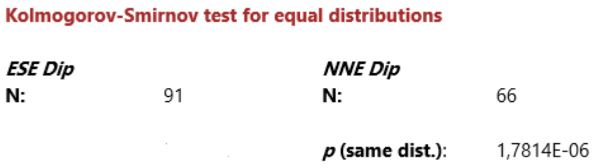

Kolmogorov-Smirnov test for equal distributions

ESE Dip
N: 91

NNE Dip
N: 66

p **(same dist.):** 1,7814E-06

Figure 34- Dip Kolmogorov-Smirnov test

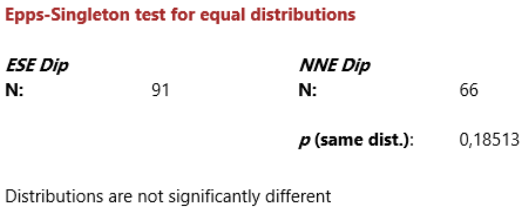

Epps-Singleton test for equal distributions

ESE Dip
N: 91

NNE Dip
N: 66

p **(same dist.):** 0,18513

Distributions are not significantly different

Figure 35- Dip Epps-Singleton test

Length:

- The NNE family follows a lognormal distribution, and the ESE family also follows a lognormal distribution. Both histograms show positive skewness (Histogram 5 and Histogram 6) and after logarithmic transformation, the NNE family histogram shows a normal distribution (Histogram 8).

- Regarding the outliers, the NNE family has 8 outliers (values equal or greater than 2655 m), while the ESE family has 12 outliers (values equal or greater than 5140 m).

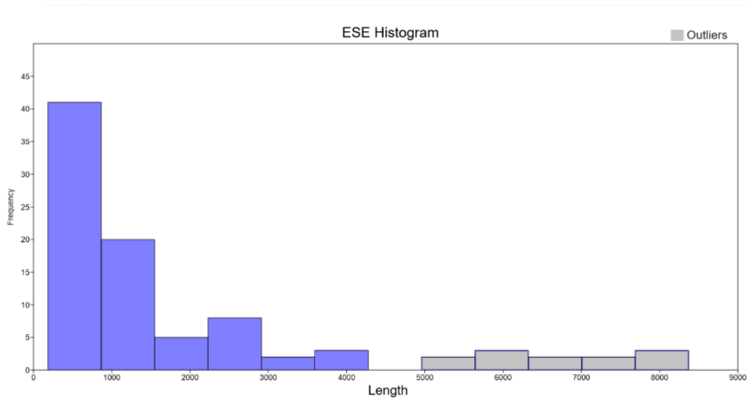

Histogram 5- ESE Family Length

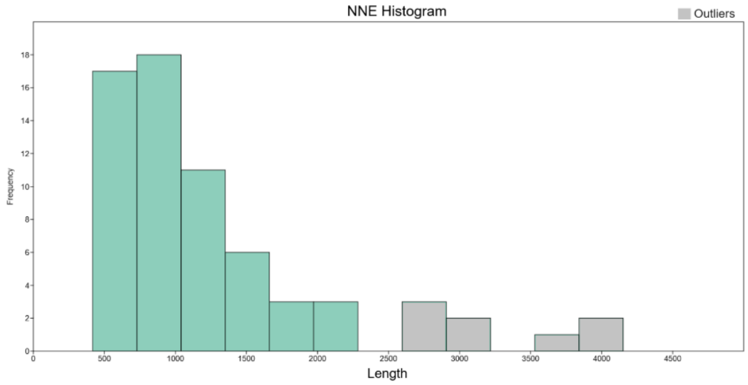

Histogram 6- NNE Family Length

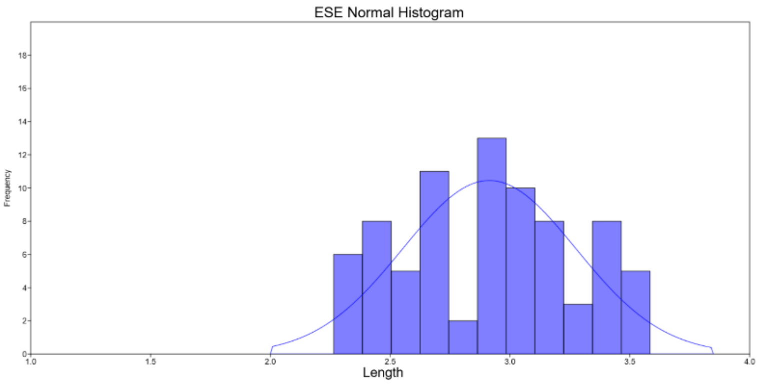

Histogram 7- ESE Family Normal-Fit

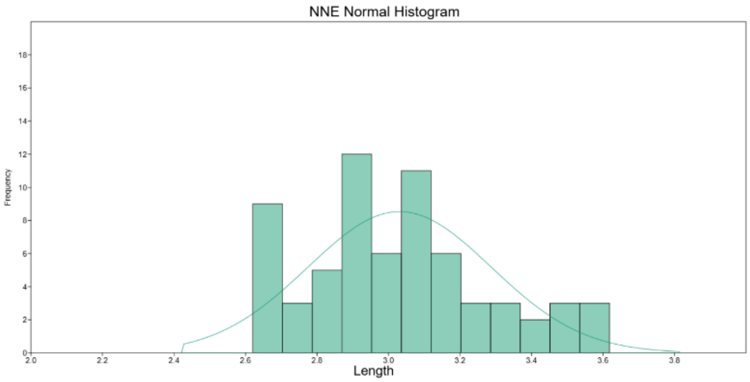

Histogram 8- NNE Family Normal-Fit

- The Shapiro and Anderson tests for the transformed values confirm the normality of the NNE family (p-values greater than 0.05) but do not show normality for the ESE family (p-values less than 0.05) as demonstrated on Table 13.

Table 13- Length normality tests

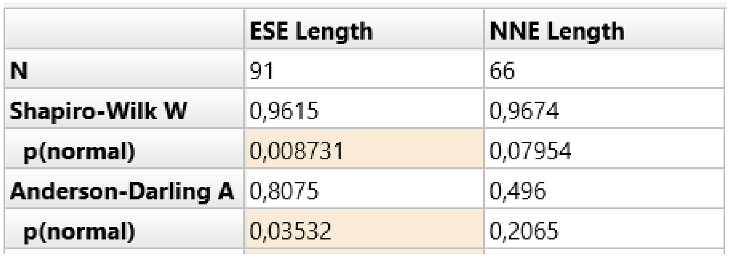

	ESE Length	**NNE Length**
N	91	66
Shapiro-Wilk W	0,9615	0,9674
p(normal)	0,008731	0,07954
Anderson-Darling A	0,8075	0,496
p(normal)	0,03532	0,2065

- After removing the outliers from the ESE family and performing a logarithmic transformation, the data closely follow a normal distribution (Histogram 7). When adjusted to a normal-probability model (Figure 36), the data fit the model with a correlation coefficient of 0.98. Normality tests also suggest a normal distribution of the data.

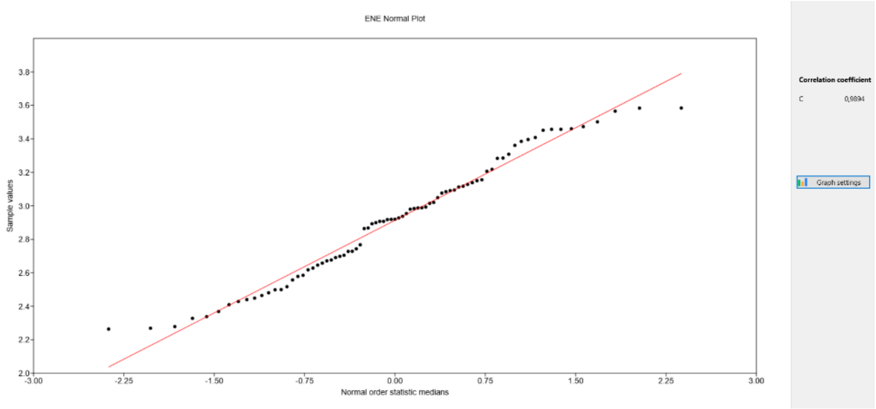

Figure 36- ESE Family Length normal-probability plot

- The t-test (Figure 37) does not reveal evidence about the equality of means, while the F-test (Figure 38) shows different variances (F value greater than the critical F value, and p lower than the significance level).

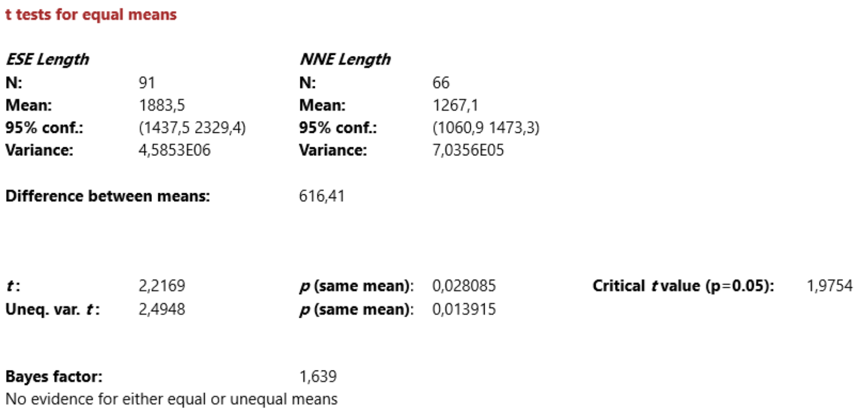

```
t tests for equal means

ESE Length                                NNE Length
N:              91                        N:              66
Mean:           1883,5                    Mean:           1267,1
95% conf.:      (1437,5 2329,4)           95% conf.:      (1060,9 1473,3)
Variance:       4,5853E06                 Variance:       7,0356E05

Difference between means:                 616,41


t:              2,2169                    p (same mean):  0,028085      Critical t value (p=0.05):   1,9754
Uneq. var. t:   2,4948                    p (same mean):  0,013915


Bayes factor:                             1,639
No evidence for either equal or unequal means
```

Figure 37- Length t-test

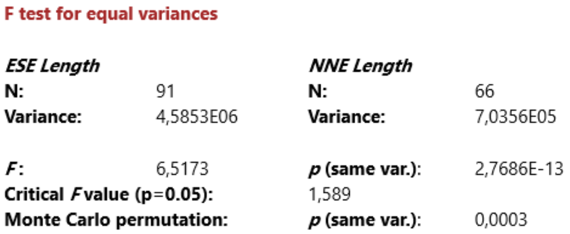

```
F test for equal variances

ESE Length                            NNE Length
N:                      91            N:                  66
Variance:               4,5853E06     Variance:           7,0356E05

F:                      6,5173        p (same var.):      2,7686E-13
Critical F value (p=0.05):            1,589
Monte Carlo permutation:              p (same var.):      0,0003
```

Figure 38- Length F-test

For modelling purposes, the decision was to include outliers in the length parameter, assuming that combined fractures (two or more fractures apparently connected) may have contributed to the highest length values, which consequently affected the analysis of this parameter and consequently the H/L ratio.

Height:

- The ESE family follows a lognormal distribution. Histogram 11 shows positive skewness, and after logarithmic transformation, the histogram displays a normal distribution (Histogram 9). The NNE family follows a normal distribution, as shown in Histogram 10.

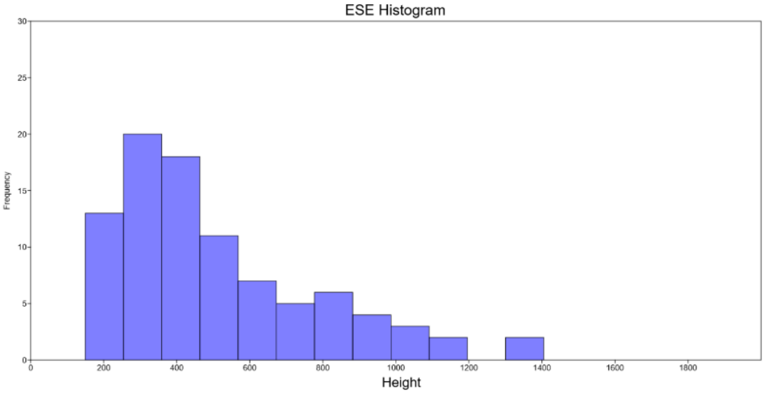

Histogram 11- ESE Family Height

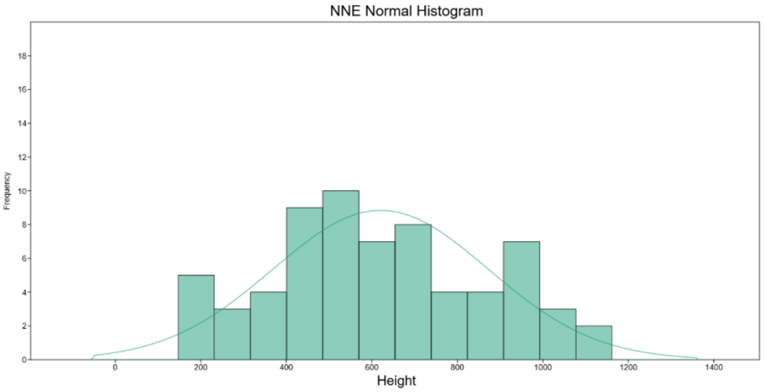

Histogram 10- NNE Family Height

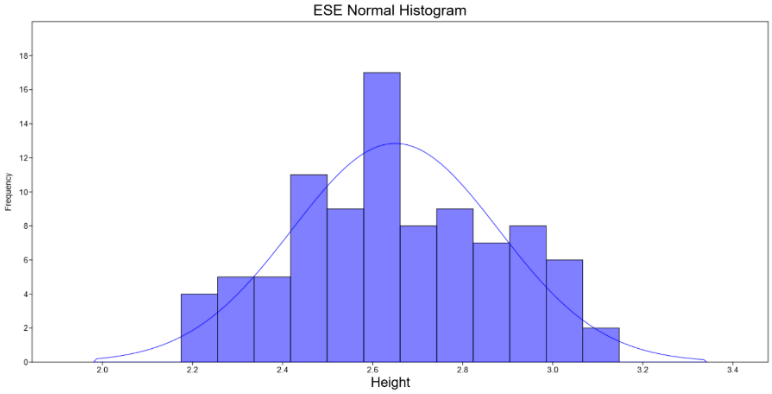

Histogram 9- ESE Family Height Normal-Fit

- Normal-probability tests on both variables (with the ESE family transformed logarithmically) confirm the distributions (Shapiro and Anderson test p-values greater than 0.05) as demonstrated on Table 14.

Table 14- Height normality tests

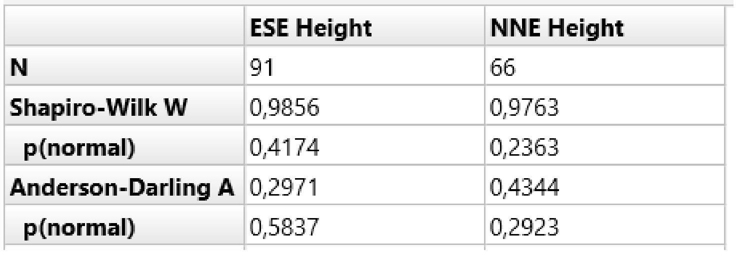

	ESE Height	NNE Height
N	91	66
Shapiro-Wilk W	0,9856	0,9763
p(normal)	0,4174	0,2363
Anderson-Darling A	0,2971	0,4344
p(normal)	0,5837	0,2923

- The t-test (Figure 39) indicates different means for the variables, and the F-test (Figure 40) suggests that the variances are likely equal (the calculated F value is lower than the critical F value, and the p-value is greater than 0.05).

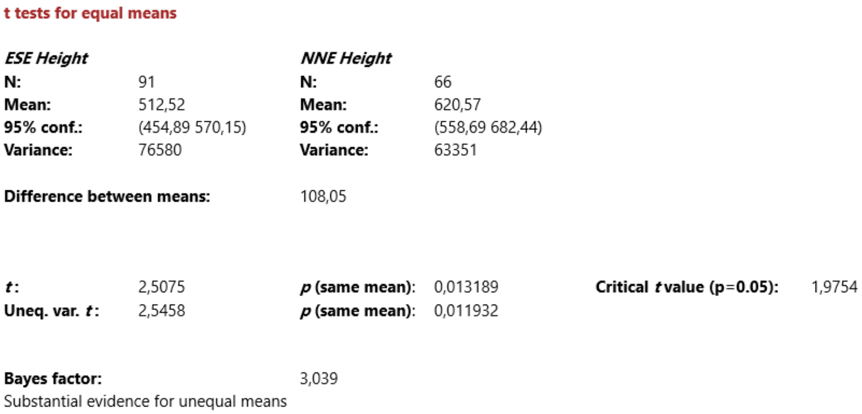

```
t tests for equal means

ESE Height                           NNE Height
N:              91                   N:              66
Mean:           512,52               Mean:           620,57
95% conf.:      (454,89 570,15)      95% conf.:      (558,69 682,44)
Variance:       76580                Variance:       63351

Difference between means:            108,05


t:              2,5075               p (same mean):  0,013189        Critical t value (p=0.05):    1,9754
Uneq. var. t:   2,5458               p (same mean):  0,011932


Bayes factor:                        3,039
Substantial evidence for unequal means
```

Figure 39- Height t-test

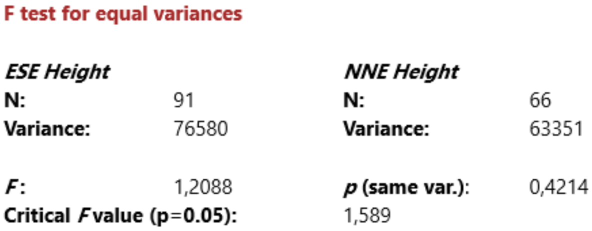

```
F test for equal variances

ESE Height                      NNE Height
N:              91              N:              66
Variance:       76580           Variance:       63351

F:              1,2088          p (same var.):  0,4214
Critical F value (p=0.05):      1,589
```

Figure 40- Height F-test

Aspect Ratio (H/L):

The histogram of the ESE family suggests a bimodal distribution (Histogram 13). However, the kernel density curve aligns with one of the peaks, but it does not match the other peak as accurately (Histogram 12). When using mixture models, the 4-mode model showed the highest log-likelihood and the lowest AIC value (Histogram 14), indicating a better fit than the bimodal model, however, the kernel density curve does not match the peaks as shown in . In contrast, the NNE family's histogram indicates a trimodal distribution

(Histogram 15), with the kernel density curve matching the observed distribution (Histogram 16). Based on these results, the trimodal normal distribution appears to be the best fit for the NNE family, and the 4-mode model for the ESE family. Since none of the distribution fits both families, another approach was taken to find a distribution that would accommodate both families.

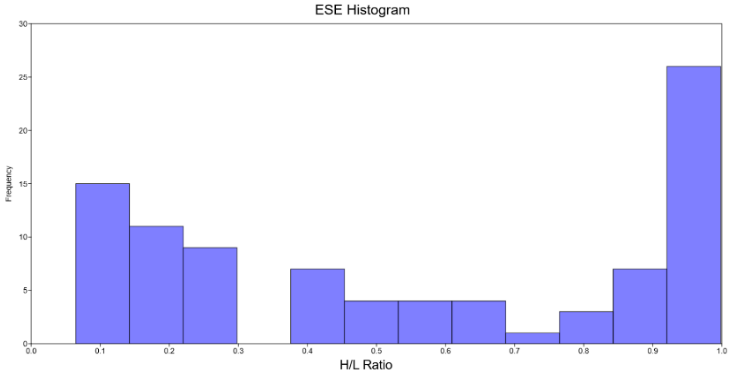

Histogram 13- ESE Family H/L

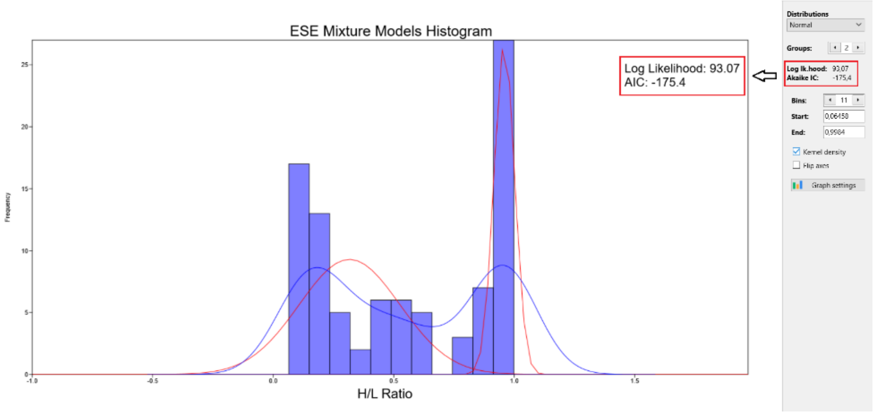

Distributions: Normal
Groups: 2
Log lk.hood: 93,07
Akaike IC: -175,4
Bins: 11
Start: 0,06458
End: 0,9984
☑ Kernel density
☐ Flip axes

Histogram 12- ESE Family H/L Bimodal with kernel density curve (in red)

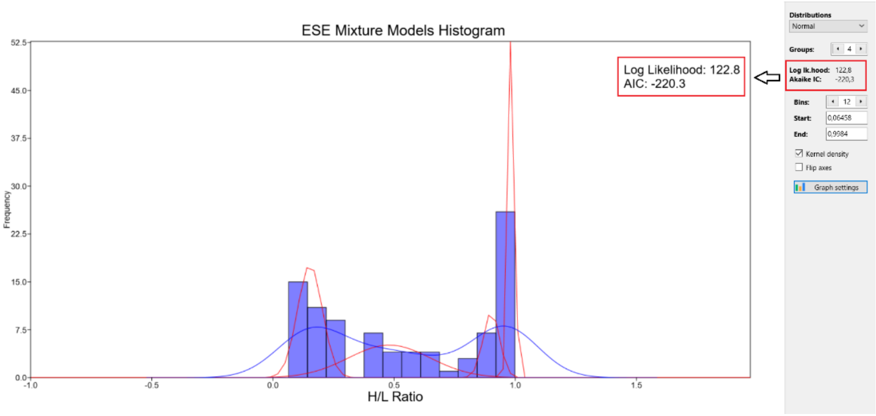

Distributions: Normal
Groups: 4
Log lk.hood: 122,8
Akaike IC: -220,3
Bins: 12
Start: 0,06458
End: 0,9984
☑ Kernel density
☐ Flip axes

Histogram 14- ESE Family H/L 4-Modes with Kernel Density Curve (in red)

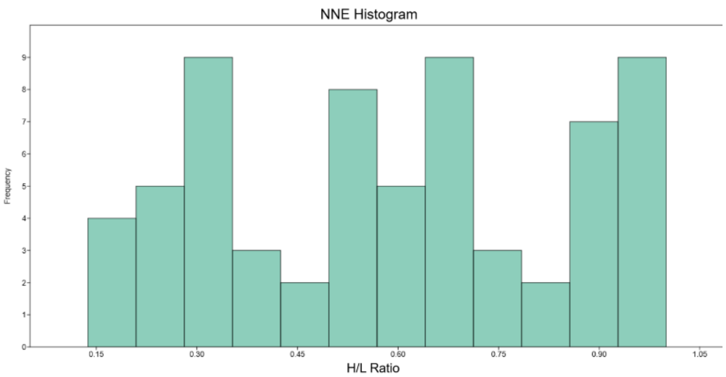

Histogram 15- NNE Family H/L

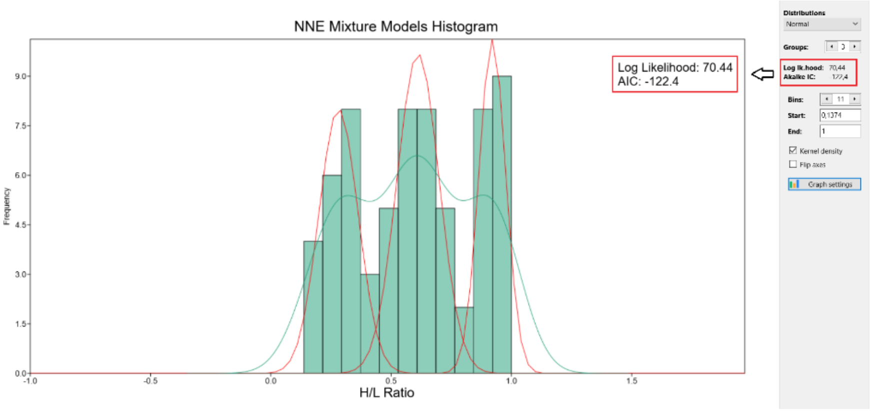

Distributions: Normal
Groups: 3
Log lk.hood: 70,44
Akaike IC: -122,4
Bins: 11
Start: 0,1374
End: 1
☑ Kernel density
☐ Flip axes

Histogram 16- NNE Family H/L with kernel density curve (in red)

The observations were plotted, and various models were tested for both families. For the ESE none of the models produced a R² value higher than 0.35 (Figure 41), indicating that even the best-fit model accounted for only 35% of the data, while the NNE family models' did not achieve a R² value greater than 0.29 (Figure 42), meaning that, at most, only 29% of the data was represented by the models. These results are both referring to the logistic model.

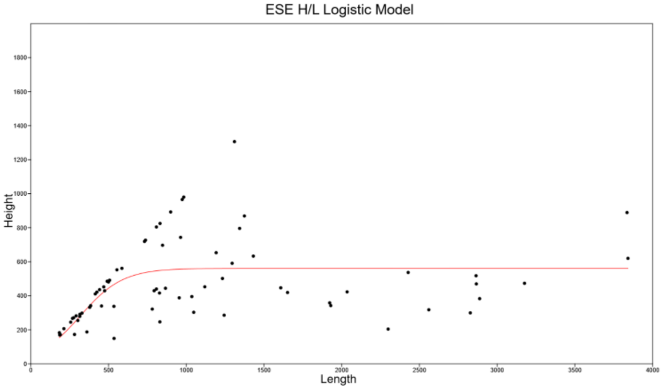

Figure 41- ESE Family H/L Logistic Model

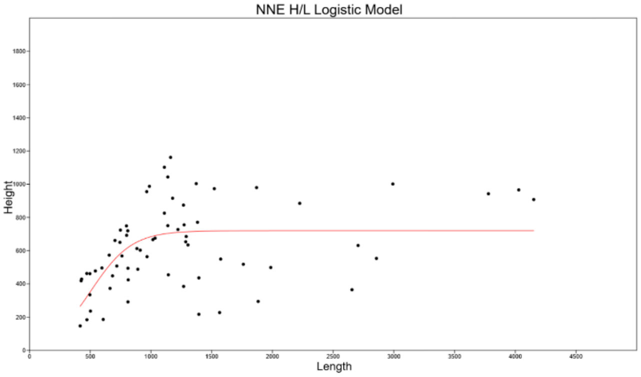

Figure 42- NNE Family H/L Logistic Model

Regarding the observations from each group within the families appeared to follow two distinct distributions - one portion aligned with the logistic model, while the other seemed to follow a linear distribution with a steep positive slope. These results indicate that none of the tested models were able to adequately capture the complexity of the data for either family meaning that the height/length ratios are heterogeneous when analyzed by groups and/or families of fractures.

Given the absence of a suitable distribution for such diverse data, the final approach was to define a worst-case and best-case scenario for each fracture's family by limiting the observations with two linear models – a maximum and a minimum model – and using the regression slope values to assess the maximum and minimum values of height/length ratio of each family.

The presence of two distinct distributions within the same family of fractures impacted the interpretation of the data. This complexity made it challenging to determine a single representative height/length ratio for each family. As a result, a simplification was necessary to address the heterogeneity. The approach taken was to define worst-case and best-case scenarios, representing the maximum and minimum possible values of the height/length ratio for each family. The decision to use an approach based on worst-case and best-case scenarios is a practical solution when a more accurate model cannot be found. By identifying the boundaries of the height/length ratios, the method captures the full extent of the data's variability while avoids forcing to fit the data into a single model that doesn't fit accurately and instead offers a more flexible way to understand the fracture behavior. Although this approach may lose some precision, it offers reliability by ensuring the variability within the data is accounted. Therefore, it is acknowledged that although the worst-case/best-case simplification helps handling the complexity of the data, it can mask some details, potentially resulting in predictions that are either too conservative or too optimistic.

Fracture Intensity:

Each section that was defined for the fractures' intensity assessment, from the largest to the smallest, had different volumes due to variations in the thickness of the formations. The results showed considerable variations in fracture intensity both laterally and vertically.

Even though there were only three different section sizes — larger sections around 189 km², smaller ones around 47 km², and the smallest sections around 12 km² — all sections revealed different volumes as it's shown on Figure 43 and Figure 44. This was due to lateral changes in the thickness of the formations. As a consequence, the volume of the defined intervals also varied within sections, even when their areas were the same.

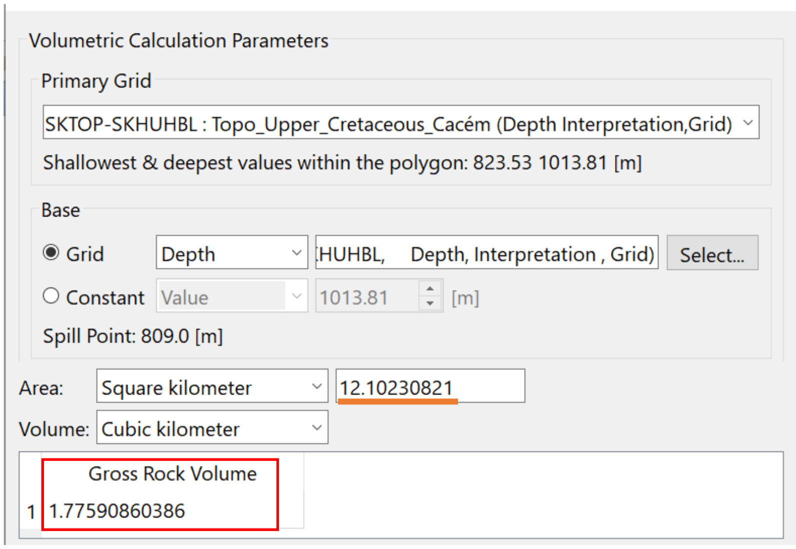

Volumetric Calculation Parameters

Primary Grid

SKTOP-SKHUHBL : Topo_Upper_Cretaceous_Cacém (Depth Interpretation,Grid)

Shallowest & deepest values within the polygon: 823.53 1013.81 [m]

Base

● Grid Depth HUHBL, Depth, Interpretation , Grid) Select...

○ Constant Value 1013.81 [m]

Spill Point: 809.0 [m]

Area: Square kilometer 12.10230821

Volume: Cubic kilometer

	Gross Rock Volume
1	1.77590860386

Figure 43- C-TVG Volumetric Calculation (in section 1.2)

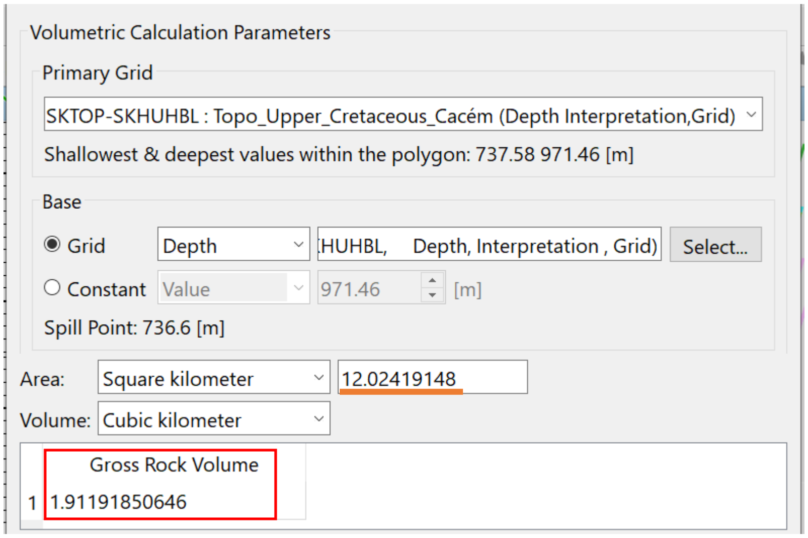

Volumetric Calculation Parameters

Primary Grid

SKTOP-SKHUHBL : Topo_Upper_Cretaceous_Cacém (Depth Interpretation,Grid)

Shallowest & deepest values within the polygon: 737.58 971.46 [m]

Base

● Grid Depth HUHBL, Depth, Interpretation , Grid) Select...

○ Constant Value 971.46 [m]

Spill Point: 736.6 [m]

Area: Square kilometer 12.02419148

Volume: Cubic kilometer

	Gross Rock Volume
1	1.91191850646

Figure 44- C-TVG Volumetric Calculation (in section 1.3)

The SB-C interval includes all formations between the seabed surface (whose depth also varies laterally) and the top of the Cacém formation, comprising the Aveiro Group and Espadarte Formation. This is the thickest interval of the three, leading to the largest volumes and the lowest fracture intensity values (ranging from 0.03 to 0.95 fractures per cubic kilometer for the ESE family and 0.02 to 1.1 fractures per cubic kilometer for the NNE family).

The C-TV interval includes the Cacém Formation which ends at the top of the following formation, the Torres Vedras Group. It has the smallest thickness, resulting in the lowest volumes and the highest fracture intensity values (ranging from 0.16 to 6.97 fractures per cubic kilometer in the ESE family and 0.12 to 7.56 fractures per cubic kilometer in the NNE family).

The TV-Alc interval, which ranges from the top of the Torres Vedras Group to the top of the Alcobaça Formation, has intermediate volume and fracture intensity values compared to the other two intervals (ranging from 0.06 to 2.24 fractures per cubic kilometer in the ESE family and 0.06 to 4.04 fractures per cubic kilometer in the NNE family).

Given the absence of a suitable distribution for the data, the chosen approach was to establish a worst-case and best-case scenario for each interval in both fracture families. These scenarios are again represented by the minimum and maximum possible value of fracture intensity and the results are presented on Table 15. The average value of fracture intensity was also calculated.

Table 15- Fracture Intensity Results

Interval	**Strike ESE**	**Strike NNE**
SB-C	Max. = 0.95 Mean = 0.26 Min. = 0.03	Max. = 1.10 Mean = 0.33 Min. = 0.02
C-TV	Max. = 6.97 Mean = 1.41 Min. = 0.16	Max. = 7.56 Mean = 2.38 Min. = 0.12
TV-Alc	Max. = 2.24 Mean = 0.47 Min. = 0.06	Max. = 4.04 Mean = 0.77 Min. = 0.06

By progressively dividing the study area into smaller sections for fracture intensity assessment, lateral variations in the fracture distribution were addressed. This approach ensured that areas with a high concentration of fractures were isolated and counted separately from areas with fewer fractures. The vertical variation was addressed by defining distinct depth intervals, which allowed a more accurate and realistic analysis of the area.

The method of reducing the considered volume and defining intervals at different depths to count the number of fractures, instead of analyzing the entire study area at once, with its varying conditions was particularly effective since the fractures being studied did not all intersect the same formations or spread constantly across the region. Although this method was considered the most effective, potential biases can occur, as fracture intensity can be influenced by the defined intervals and their respective volumes. As mentioned, the lowest intensity values are related to the largest volumes, while the highest intensities correspond to the smallest volumes. This is expected since intensity is calculated as the number of fractures per unit of volume, which could introduce some bias to the results. Defining boundaries with minimum and maximum intensity values ensures that both extreme values of the fracture intensity are accounted for as well as the full extent of the data, offering a robust approach to handle the variability.

5.2 Fracture Models

The objective of developing the fracture models is to provide relevant information regarding the behavior of fracture networks within the geological complex, in order to understand the potential for CO_2 storage in the target area. These models are designed to assess the influence of fractures on the feasibility and conditions of the storage complex, focusing on the integrity of the sealing formation.

For the models' computation, the first step was to determine which scenarios should be computed by selecting and combining the available input options for each parameter. Since there are two major families of fractures previously identified, the different scenarios were developed based on that consideration. Similar scenarios were created for both families, each one including the respective parameter values specific to each family.

The models considered as worst-case scenarios were not visible due to a limitation in the modelling software, which restricts the visualization of fractures when the density is too low. Consequently, it was necessary to create an additional scenario that considered an average density value, in order to analyze more models, allowing a more comprehensive discussion. Since the height/length ratio was also a parameter that varied between the worst and best-case models, the decision made was to include the minimum height/length ratio values in the models with the average density value. This approach ensured that these minimum ratio values were accounted in the analysis, rather than being excluded due to the inability to observe the worst-case models. Table 16 and Table 17 summarize the input values used in each computed model.

The development of different fracture network scenarios allowed to have a comprehensive characterization of the fractures in the study area by proposing different possibilities on how the fractures might occur in the region. The models created from these scenarios allowed the visualization of the potential fracture distributions within the area while considering the main fracture characteristics such as length, height, orientation and aspect ratio. This provided a useful analogue to understand the fracture behavior in the prospect area.

Table 16- ESE Family Scenarios

Best-Case ESE	**Model 1**	**Model 2**	**Model 3**
Length	Lognormal (Mean=1883.5 st.dev=2142.3)	Lognormal (Mean=1883.5 st.dev=2142.3)	Lognormal (Mean=1883.5 st.dev=2142.3)
Strike	Uniform (Max= 108º Min.= 106º)	Uniform (Max= 108º Min.= 106º)	Uniform (Max= 108º Min.= 106º)
Dip	Uniform (Max= 90º Min.= 75º)	Uniform (Max= 90º Min.= 75º)	Uniform (Max= 90º Min.= 75º)
H/L Ratio	1:0.97	1:0.97	1:0.97
Intensity	0.95	6.97	2.24
Average-Case ESE	**Model 1**	**Model 2**	**Model 3**
Length	Lognormal (Mean=1883.5 st.dev=2142.3)	Lognormal (Mean=1883.5 st.dev=2142.3)	Lognormal (Mean=1883.5 st.dev=2142.3)
Strike	Uniform (Max= 108º Min.= 106º)	Uniform (Max= 108º Min.= 106º)	Uniform (Max= 108º Min.= 106º)
Dip	Uniform (Max= 90º Min.= 75º)	Uniform (Max= 90º Min.= 75º)	Uniform (Max= 90º Min.= 75º)
H/L Ratio	1:14	1:14	1:14
Intensity	0.26	1.41	0.47
Worst-Case ESE	**Model 1**	**Model 2**	**Model 3**
Length	Lognormal (Mean=1883.5 st.dev=2142.3)	Lognormal (Mean=1883.5 st.dev=2142.3)	Lognormal (Mean=1883.5 st.dev=2142.3)
Strike	Uniform (Max= 108º Min.= 106º)	Uniform (Max= 108º Min.= 106º)	Uniform (Max= 108º Min.= 106º)
Dip	Uniform (Max= 90º Min.= 75º)	Uniform (Max= 90º Min.= 75º)	Uniform (Max= 90º Min.= 75º)
H/L Ratio	1:14	1:14	1:14
Intensity	0.03	0.16	0.06

Table 17- NNE Family Scenarios

Best-Case NNE	**Model 1**	**Model 2**	**Model 3**
Length	Lognormal (Mean=1267.1 st.dev=838.8)	Lognormal (Mean=1267.1 st.dev=838.8)	Lognormal (Mean=1267.1 st.dev=838.8)
Strike	Uniform (Max= 17º Min.= 12º)	Uniform (Max= 17º Min.= 12º)	Uniform (Max= 17º Min.= 12º)
Dip	Uniform (Max= 90º Min.= 85º)	Uniform (Max= 90º Min.= 85º)	Uniform (Max= 90º Min.= 85º)
H/L Ratio	1:1.04	1:1.04	1:1.04
Intensity	1.1	7.56	4.04
Average-Case NNE	**Model 1**	**Model 2**	**Model 3**
Length	Lognormal (Mean=1267.1 st.dev=838.8)	Lognormal (Mean=1267.1 st.dev=838.8)	Lognormal (Mean=1267.1 st.dev=838.8)
Strike	Uniform (Max= 17º Min.= 12º)	Uniform (Max= 17º Min.= 12º)	Uniform (Max= 17º Min.= 12º)
Dip	Uniform (Max= 90º Min.= 85º)	Uniform (Max= 90º Min.= 85º)	Uniform (Max= 90º Min.= 85º)
H/L Ratio	1:10	1:10	1:10
Intensity	0.33	2.38	0.77
Worst-Case NNE	**Model 1**	**Model 2**	**Model 3**
Length	Lognormal (Mean=1267.1 st.dev=838.8)	Lognormal (Mean=1267.1 st.dev=838.8)	Lognormal (Mean=1267.1 st.dev=838.8)
Strike	Uniform (Max= 17º Min.= 12º)	Uniform (Max= 17º Min.= 12º)	Uniform (Max= 17º Min.= 12º)
Dip	Uniform (Max= 90º Min.= 85º)	Uniform (Max= 90º Min.= 85º)	Uniform (Max= 90º Min.= 85º)
H/L Ratio	1:10	1:10	1:10
Intensity	0.02	0.12	0.06

5.2.1 ESE Family Scenarios

The best-case scenario includes three models (Figure 45, Figure 46, and Figure 47) with different intensity values, representing the maximum fracture intensity within each depth interval. This means that in each interval the fractures have the same height/length ratio (1:0.97), while having strikes ranging from 106º to 108º and dips from 75º to 90º. Fracture lengths follow a lognormal distribution with an average of around 1884 meters. These results show that the fractures within the best-case scenarios do not vary significantly regarding its strike and the height/length ratio suggests that each fracture has a length value similar to its height. Model 2 shows the highest fracture intensity.

Average-case scenario comprises three models (Figure 48, Figure 49, and Figure 50) with different intensity values, which represent the average fracture intensity in each depth interval. In these intervals, the fractures have the same height/length ratio (1:14), while strikes range from 106º to 108º and dips between 75º to 90º. Fracture lengths follow a lognormal distribution with a mean value of around 1884 meters. These results indicate a small variation in the fracture strike (short range of strikes) and the height/length ratio reveals that each fracture has a length 14 times higher than its height. Model 2 presents the highest fracture intensity as expected. Fracture models exhibiting the reservoir grid considered for modelling purposes are shown in Appendix 8.

In the worst-case scenario, all parameter values are identical to those in the average-case models, except for the fracture intensity, which is defined as the lowest possible value for this family. This low intensity makes the models impossible to visualize, as mentioned above.

The results obtained do not seem to reflect natural conditions, with fracture dimensions being the primary issue. Some fractures revealed excessively large heights, sometimes even exceeding the dimensions of the geological grid itself. Consequently, due to the influence of these height results, the height/length ratio also shows values that deviate from realistic conditions, with fractures that should exhibit the highest height/length ratio (average-case models) appearing as ellipses with nearly equal axis lengths.

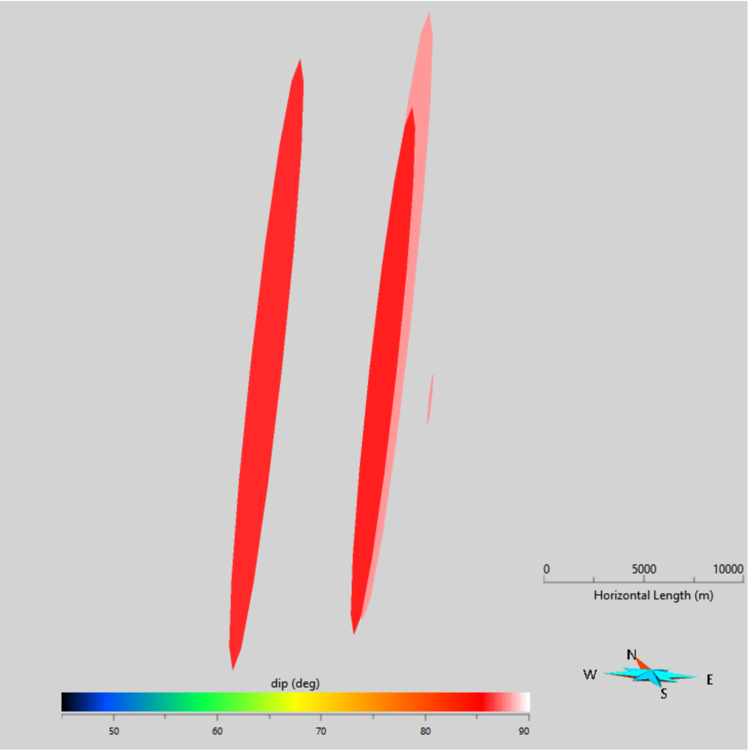

Figure 45- ESE Family Best-Case Model 1 with Dip property displayed

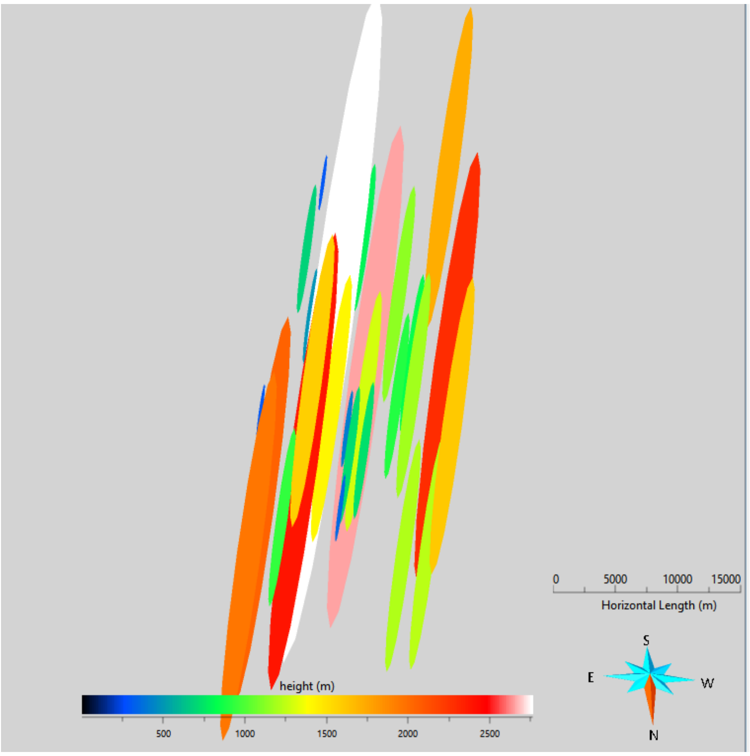

Figure 46- ESE Family Best-Case Model 2 with Height property displayed

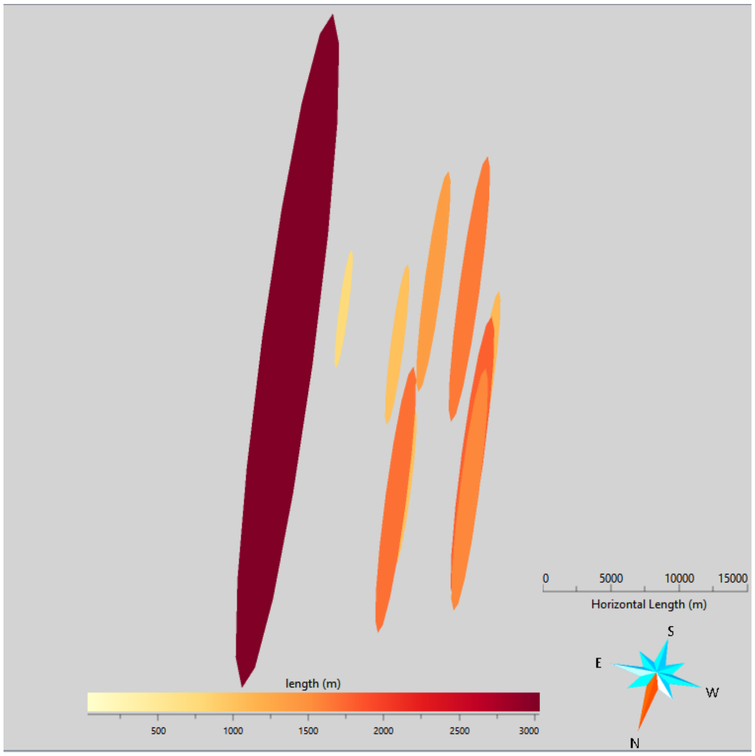

Figure 47- ESE Family Best-Case Model 3 with Length property displayed

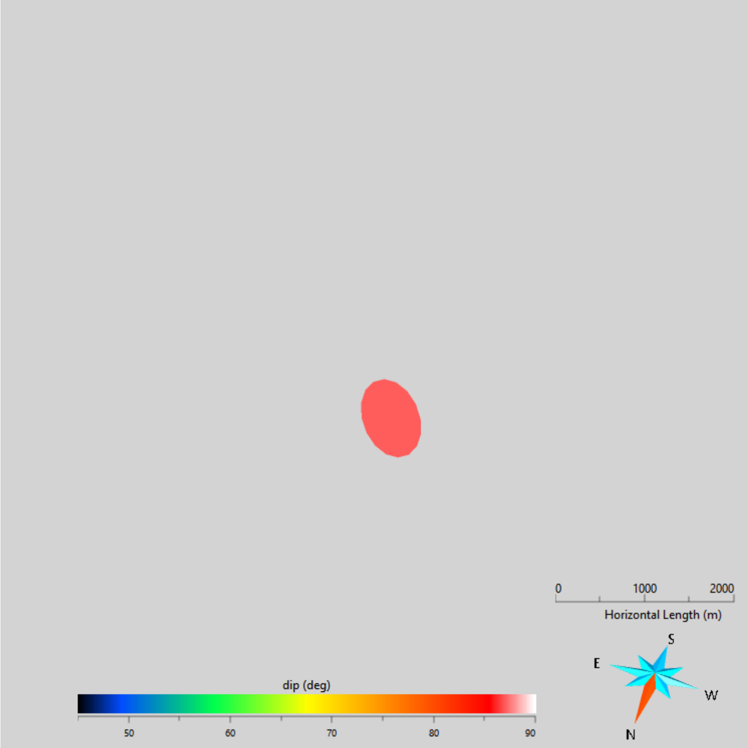

Figure 48- ESE Family Average-Case Model 1 with Dip property displayed

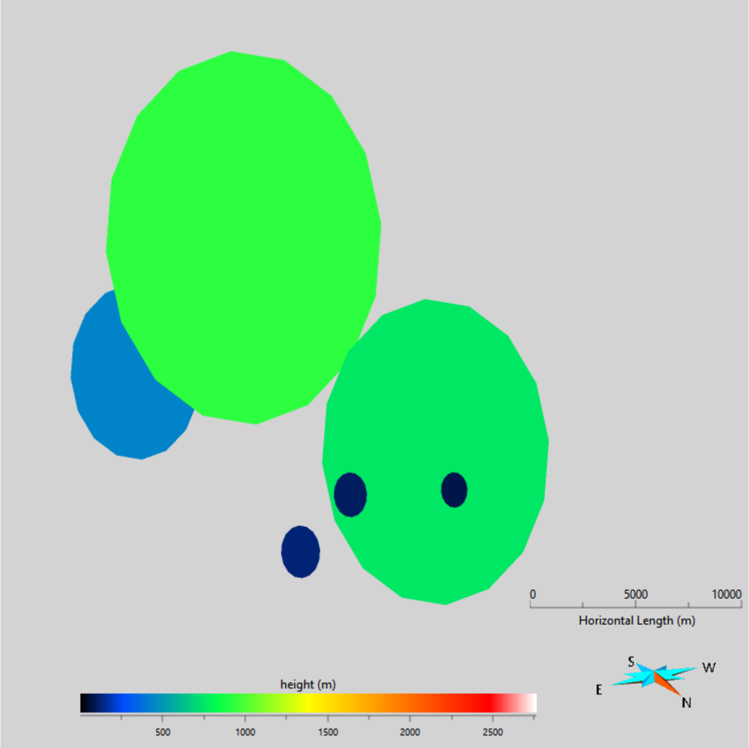

Figure 49- ESE Family Average-Case Model 2 with Height property displayed

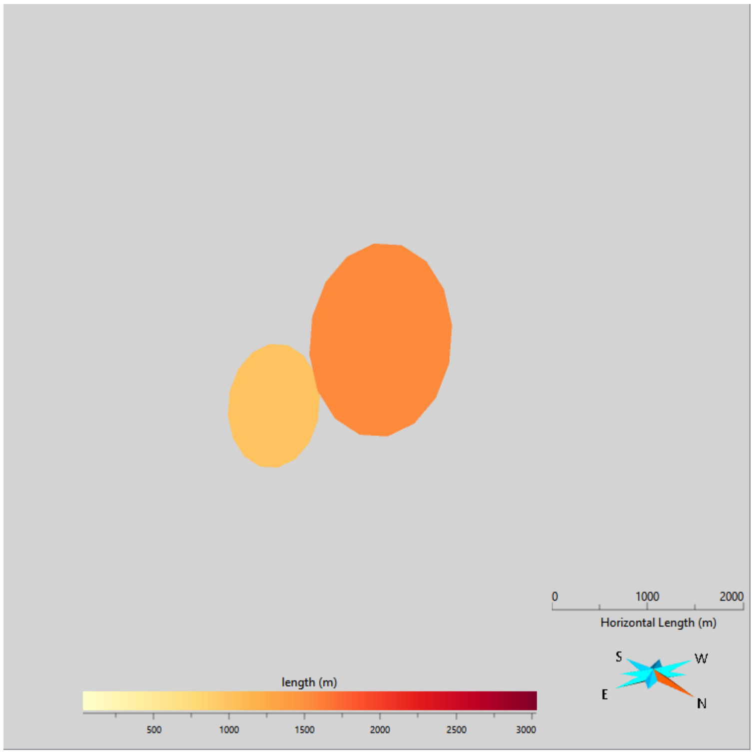

Figure 50- ESE Family Average-Case Model 3 with Length property displayed

5.2.2 NNE Family Scenarios

The best-case scenario includes three models (Figure 51, Figure 52, and Figure 53) with varying intensity values, representing the highest fracture intensity within each depth interval. This means that

in each interval the fractures share the same height/length ratio (1:1.04), while having strikes ranging from 12º to 17º and dips between 85º to 90º. Fracture lengths follow a lognormal distribution with an average of around 1267 meters. These results show that the fractures within this family are predominantly subvertical to vertical, with a small variation in dip. The height/length ratio suggests that the fractures' lengths are nearly equal to their heights. Once again, Model 2 shows the highest fracture intensity.

The Average-case scenario includes three models (Figure 54, Figure 55, and Figure 56) with different intensity values, representing the average fracture intensity in each depth interval. In these intervals, the fractures have the same height/length ratio (1:10), while strikes range from 12º to 17º and dips from 85º to 90º. Fracture lengths follow a lognormal distribution with an average of around 1267 meters. These results suggest that the fractures in this family are predominantly subvertical or vertical, having a small variation in their dips. The height/length ratio indicates that each fracture is 10 times longer than its height. As expected, Model 2 exhibits the highest fracture intensity. Fracture models exhibiting the reservoir grid considered for modelling purposes are shown in Appendix 9.

In the worst-case scenario, all parameter values are equal to those in the average-case models, except for the fracture intensity, which is set as the minimum possible value for this family. These extremely low intensity values make the models impossible to visualize, as previously referred.

Similarly to the ESE Family models, the obtained results are unrealistic. Some fractures showed excessively large heights, in some cases exceeding the dimensions of the geological grid. Consequently, the height/length ratio also shows values that deviate from realistic conditions, with fractures that should exhibit the highest height/length ratio (average-case models) appearing as ellipses with nearly equal axis sizes.

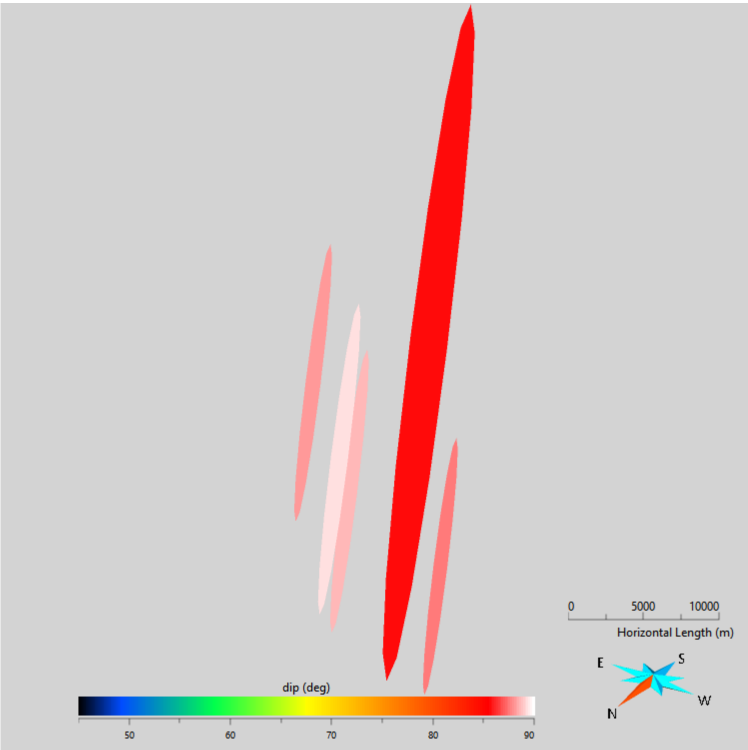

Figure 51- NNE Family Best-Case Model 1 with Dip property displayed

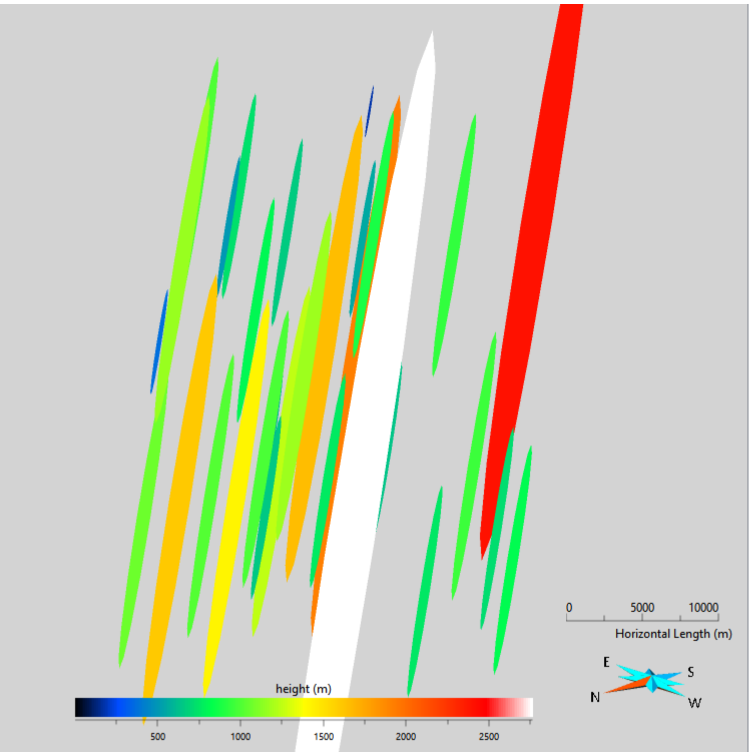

Figure 52- NNE Family Best-Case Model 2 with Height property displayed

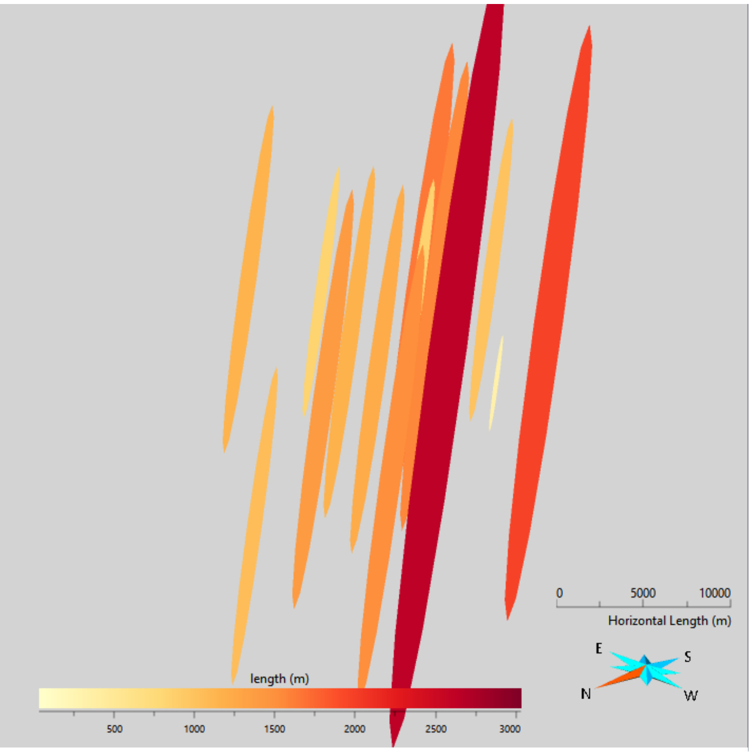

Figure 53- NNE Family Best-Case Model 3 with Length property displayed

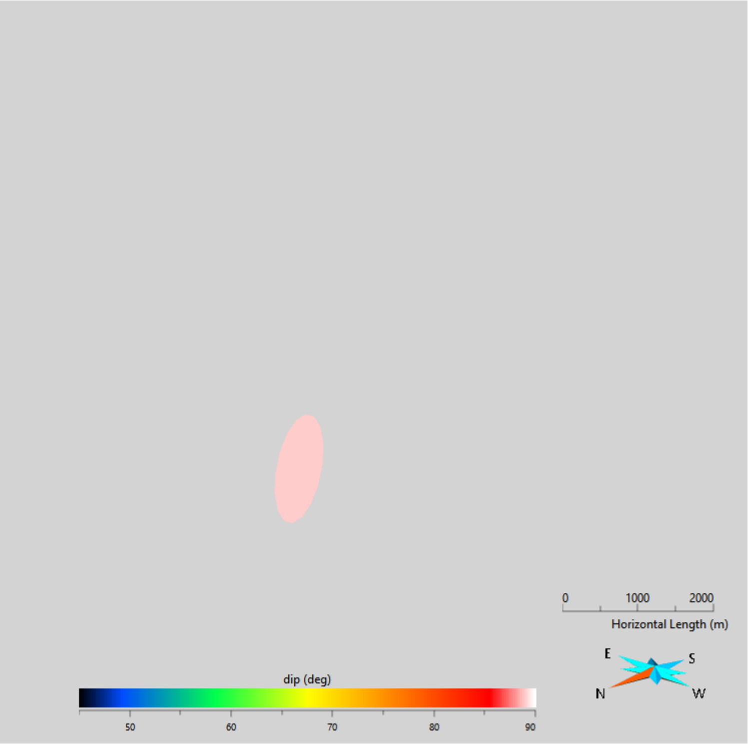

Figure 54- NNE Family Average-Case Model 1 with Dip property displayed

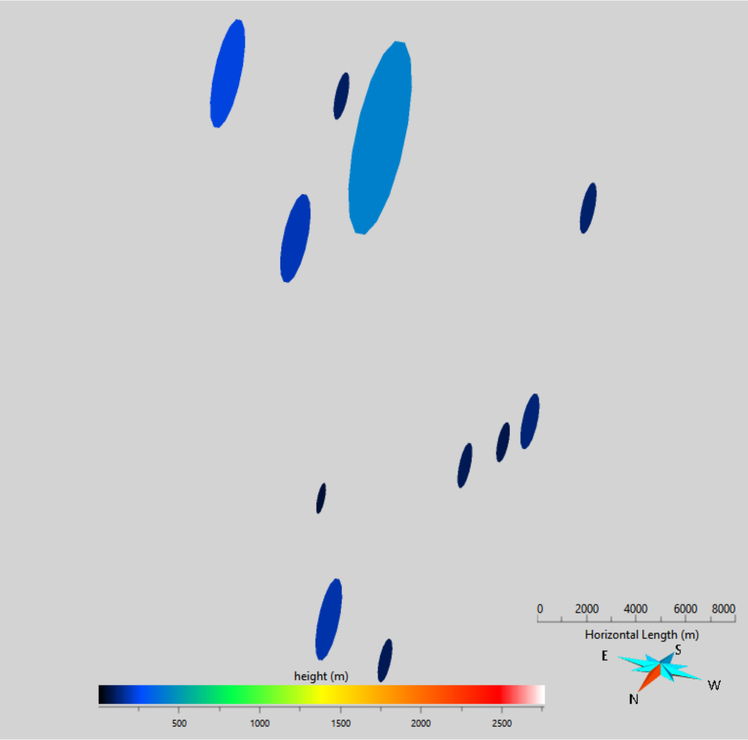

Figure 55- NNE Family Average-Case Model 2 with Height property displayed

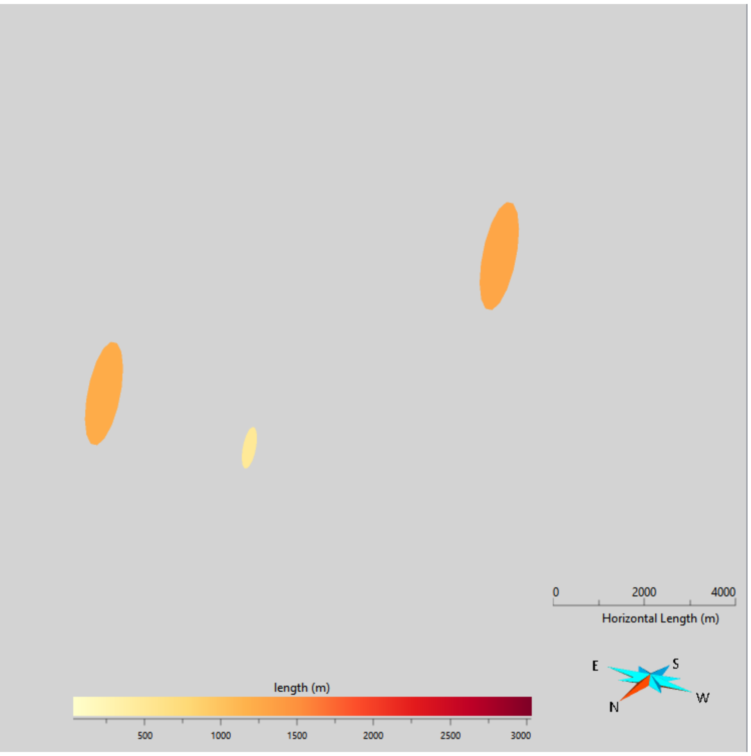

Figure 56- NNE Family Average-Case Model 3 with Length property displayed

6 Conclusions

6.1 CCUS Role

The use of CCUS is essential for industry decarbonization, providing an important solution to mitigate emissions in challenging sectors like cement, iron and steel, and chemicals. Alongside strategies like improving energy efficiency, electrification (including hydrogen production), and increased renewable energy use, CCUS is part of a comprehensive technology mix that can achieve significant emissions reductions at the lowest cost in these industries. Establishing CCUS hubs with shared CO_2 transport and storage infrastructure in industrial zones could reduce costs for facilities implementing carbon capture in production. Thus, CCUS serves as a vital tool for a cost-effective energy transition in line with the Paris Agreement’s goals.

6.2 Fracture Interpretation and Classification

After performing the interpretation and subsequently classification of the fractures within the study area, some conclusions were taken:

- The use of seismic attributes in this study provided important insights that would have been difficult to identify through traditional seismic data interpretation alone. After testing different attributes, the relief attribute was identified as particularly effective for detecting fractures. The relief attribute highlights variations in the acoustic impedance, which are often associated with fractures, especially in areas where the coherence attributes failed to provide clear results. The success of the relief attribute lies in its ability to emphasize these small-scale discontinuities.
- The definition of a target area within the Cabo Mondego 3D volume for this analysis allowed the exclusion of areas previously interpreted. This ensures that the analysis focuses on detecting new fractures that were not identified in earlier stages of the PilotStrategy project.
- During fracture interpretation, errors may occur since it is a human-driven process, meaning it relies on the interpreter's judgment and decisions. This introduces subjectivity, which can lead to inconsistencies or inaccuracies when identifying the fractures, thereby influencing the presented results.
- The classification of fractures into four distinct groups provides a structured framework to understand the fracture variability in the study area. This classification system was based on the depth of the fractures, focusing on whether the fractures cross important formations. The selection of three crosslines and three inlines was strategically made to capture representative fracture groups across the study area. These sections were selected by their relevance to the fracture classification system, ensuring that the key features of each group were observed.
- One of the challenges with the use of equidistant sections is that fracture intensity can vary laterally across the region. As a result, some sections might exhibit more complexity than others, which could lead to biased interpretations if not carefully managed. The decision to extend the interpretation to northern and southern sections, depending on the identified fracture groups, helps to mitigate this by expanding the analysis.

6.3 Fracture Modelling

Regarding the fracture characterization and modelling, considering the results and challenges encountered, several conclusions can be drawn:

- The modelling tests conducted with the beta version of AspenSKUA v14.5 provided valuable conclusions about the functionality of the software and its application to fracture modelling. By using fictional data, these tests allowed to experiment various input parameters, including fracture intensity, orientation (strike and dip), and height/length ratio. The tests also revealed that the software is well-suited to handle the complexity of the fracture data in the study area. The purpose of these initial modelling tests, besides getting familiar with the software and understanding parameter selection, is to prepare for more detailed modelling, which can be relevant when working with a beta version of the software.
- Although the developed fracture models provided important insights, it is crucial to account for the errors associated with these models which result from several factors mentioned above: Fracture interpretation subjectivity since it is a human-driven process, leading to potential errors in fracture identification. The method conducted to assess fracture intensity by reducing the volume and defining depth intervals, although effective, introduced biases as intensity values were influenced by the size of the volumes.
- The use of worst-case and best-case scenarios for fracture intensity and height/length ratios captured the data's full range but simplified the models, potentially ignoring smaller details and reducing precision. Including outliers in the fracture length parameter added complexity but ensured a more comprehensive analysis. Additionally, it is acknowledged that the study area serves as an analogue for the prospect area, creating uncertainty about whether the prospect location will exhibit the same fracture characteristics.
- Finally, the beta version of the modelling software also presented several issues, particularly with the fracture dimensions. Some fractures were given unrealistic heights, even larger than the geological grid. This also impacted the height/length ratio, leading to fractures that should show high height/length ratios but instead appear almost circular, with nearly equal axis sizes.

Despite these uncertainties and errors, the approach provided a reliable framework for understanding fracture behavior, taking into account the data’s complexity and practical limitations. The practical impact of this work lies in its contribution to an ongoing project, where the results from this fracture characterization will be integrated into the dynamic simulations. This study aims to offer important information about how the fracture networks behave in the region, emphasizing the importance of maintaining the integrity of the seal and assessing the potential risks these fractures may cause to the storage complex.

7 References

Anders, M., & Wiltschko, D. (1994). Microfracturing, paleostress and the growth of faults. *Journal of Structural Geology*, 795-815.

Arts, R. e. (2008). *What does CO2 geological storage really mean?* CO2GeoNet.

Azerêdo, A., Duarte, L., Henriques, M., & Manuppella, G. (2003). *Da dinâmica continental no Triásico aos mares no Jurássico Inferior e Médio.* Lisboa: Instituto Geológico e Mineiro.

Bachu, S. (2007, November 7). Progress in Energy and Combustion Science. *CO2 storage in geological media: Role,means, status and barriers to deployment*, pp. 254-273.

Bachu, S., & Adams, J. (2003). Sequestration of CO2 in geological media in response to climate change: capacity of deep saline aquifers to sequester CO2 in solution. *Energy Conversion and Management*, 3151-3175.

Bai, T., Maerten, L., Gross, M., & Aydin, A. (2002). Orthogonal cross joints: do they imply a regional stress rotation? *Journal of Structural Geology*, 77-88.

Bernardes, L., Carneiro, J., & Abreu, M. (2013). International Journal of Global Warming. *CO2 hydrates as a climate change mitigation strategy: definition of stability zones in the Portuguese deep offshore*.

Berner, R. A. (2003, november 20). Nature. *The long-term carbon cycle, fossil fuels and atmospheric composition*, pp. 323-326.

Blunt, M. (2010, December). Grantham Institute for Climate Change Briefing paper No4. *Carbon dioxide storage*, p. 14.

Boavida, D. e. (2011). Energy Procedia . *Integrated infrastructure for CO 2 transport and storage in the west Mediterranean*, pp. 2440-2447.

Bulhões, E., & Nogueira de Amorim, W. (2005). Princípio da SismoCamada Elementar e sua aplicação à Técnica Volume de Amplitudes (tecVA). *9th International Congress of the Brazilian Geophysical Society.* Salvador.

Busch, A., & Kampman, N. (2018). Migration and Leakage of CO 2 From Deep Geological Storage Sites. In J. A.-F. Stéphanie Vialle, *Geological Carbon Storage: Subsurface Seals and Caprock Integrity* (pp. 283-303). John Wiley & Sons.

Carneiro, J., & Mesquita, P. (2020). *Key data for characterising sources, transport options, storage and uses in promising regions. EU H2020 STRATEGY CCUS Project 837754.*

Carneiro, J., Boavida, D., & Silva, R. (2011). First assessment of sources and sinks for carbon capture and geological. *International Journal of Greenhouse Gas Control*, 538-548.

Casacão, J., Silva, F., Rocha, J., Almeida, J., & Santos, M. (2023). AAPG Bulletin. *Aspects of salt diapirism and structural evolution of Mesozoic–Cenozoic basins at the West Iberian margin*, pp. 49-85.

CCUS Hub. (n.d.). *Northern Lights/Longship*. Retrieved from The CCUS Hub: https://ccushub.ogci.com/focus_hubs/northern-lights/

Childs, C., Manzocchi, T., Walsh, J. J., Bonson, C. G., Nicol, A., & Schöpfer, M. P. (2009). A geometric model of fault zone and fault rock thickness variations. *Journal of Structural Geology*, 117-127.

Chopra, S., & Marfurt, K. (2007). *Seismic Attributes For Prospect Identification and Reservoir Characterization.* Seg Geophysical Developments.

DGEG. (n.d.). *Geologia do Petróleo - Sistemas petrolíferos*. Retrieved from DGEG: https://www.dgeg.gov.pt/pt/areas-setoriais/geologia/petroleo-armazenamento-de-co2/geologia-do-petroleo/sistemas-petroliferos/

Évora, U. (2018). *Carbonatação in-situ para redução de emissões de CO2 de fontes energéticas e industriais no Alentejo.* Retrieved from https://www.uevora.pt/investigar/projetos?id=3822

Faulkner, D., Jackson, C., Lunn, R., Schlische, R., Shipton, Z., Wibberley, C., & Withjack, M. (2010). A review of recent developments concerning the structure, mechanics and fluid flow properties of fault zones. *Journal of Structural Geology*, 1557-1575.

Global CCS Institute. (2021). *Understanding CCS.* Global CCS Institute.

Global CCS Institute. (2023). *Facilities Database*. Retrieved from co2re: https://co2re.co/FacilityData

Hammer, Ø., Harper, D., & Ryan, P. (2001). Paleontological Statistics Software Package for Education and Data analysis. *Paleontologia Electronica*, 1-9.

IEA. (2019). *Putting CO2 to Use: Creating Value from Emissions.* IEA.

IEA. (2019). *Transforming Industry through CCUS.* IEA.

IEA. (2020). *Energy Technologies Perspectives.* IEA.

IEA. (2020). *Special Report on Carbon Capture Utilisation and Storage - Energy Technology Perspectives.* IEA.

IEA. (2021). *CCUS around the world in 2021: northern-lights*. Retrieved from iea.org: https://www.iea.org/reports/ccus-around-the-world-in-2021/northern-lights

IEA. (2021). *Portugal Energy Policy Review.* IEA.

IEA. (2022). *CO2 Emissions in 2022.* IEA.

Institute, E. (2023). *Statistical Review of World Energy.* Energy Institute.

IPCC. (2005). *Special Report on Carbon Dioxide Capture and Storage.* New York, USA: Cambridge University Press.

IPCC. (2018). *Global Warming of 1.5°C. An IPCC Special Report on the impacts of global warming of 1.5°C above pre-industrial levels and related global greenhouse gas emission pathways .* Intergovernmental Panel on Climate Change.

Jornal de Negócios. (2023, November 23). *Conselho de Ministros aprova criação de mercado voluntário de carbono em Portugal*. Retrieved from Jornal de Negócios: https://www.jornaldenegocios.pt/economia/ambiente/detalhe/conselho-de-ministros-aprova-criacao-de-mercado-voluntario-de-carbono-em-portugal

Kullberg, J. (2000). *Evolução Tectónica Mesozóica da Bacia Lusitaniana*. Lisboa.

Kullberg, J., Rocha, R., Soares, A., Rey, J., Terrinha, P., Callapez, P., & Martins, L. (2006). Geologia de Portugal no contexto da Ibéria. *A Bacia Lusitaniana: Estratigrafia, Paleogeografia e Tectónica*, pp. 317-368.

Lemos de Sousa, M., Rodrigues, C., Diogo, M., & Jesus, A. (2010). Carvões portugueses: A revalorização moderna possível de um recurso geológico. O caso-de-estudo da Bacia Carbonífera do Douro. In A. R. J.M. Cotelo Neiva, *Ciências Geológicas: Ensino, Investigação e sua História* (p. 168). Lisboa: Associação Portuguesa de Geólogos (APG).

Marques da Silva, D., Caeiro, M. H., Pereira, P., Ribeiro, C., Carneiro, J., Casacão, J., & Pina, B. (2023). *Report on Conceptual Geological Models. Deliverable WP2/D2.7, EU H2020 PilotSTRATEGY project 101022664 report.* Lusitanian Basin (Portugal): In Wilkinson, M.

Nicol, A., Seebeck, H., Field, B., McNamara, D., Childs, C., Craig, J., & Rolland, A. (2017). 13th International Conference on Greenhouse Gas Control Technologies. *Fault permeability and CO2 storage* (pp. 3229 – 3236). Lausanne, Switzerland: Energy Procedia.

Pena Reis, R., Pimentel, N., & Garcia, A. (2010). Boletim de Geociencias - Petrobras. *The Lusitanian Basin (Portugal): Stratigraphic analysis and geodynamic evolution*, pp. 23-52.

Pereira, P., Ribeiro, C., & Carneiro, J. (2021). Petroleum Geoscience. *Identification and characterization of geological formations with CO2 storage potential in Portugal*, p. 20.

Pinheiro, L., Wilson, R., Pena dos Reis, R., Whitmarsh, R., & Ribeiro, A. (1996). The Western Iberia Margin: A Geophysical and Geological Overview. In R. Whitmarsh, D. Sawyer, A. Klaus, & D. Masson, *Proceedings of the Ocean Drilling Program* (pp. 4-23).

Proença Cunha, P., & Pena dos Reis, R. (1994). Cretaceous Research. *Cretaceous sedimentary and tectonic evolution of the northern sector of the Lusitanian Basin (Portugal)*, pp. 155-170.

Rasmussen, E., Lomholt, S., Andersen, C., & Vejbæk, O. (1998). Aspects of the structural evolution of the Lusitanian Basin in Portugal and the shelf and slope area offshore Portugal. *Tectonophysics*, 199-225.

Ringrose, P. (2020). SpringerBriefs in Earth Sciences. *How to Store CO2 Underground: Insights from early-mover CCS Projects*, p. 129.

Rocha, R., & Soares, A. (1984). Mem.Notícias. *Algumas reflexões sobre a sedimentação jurássica na orla meso-cenozóica ocidental de Portugal*, pp. 133-142.

Seixas, J., Fortes, P., Dias, L., Carneiro, J., Mesquita, P., Boavida, D., . . . Whiriskey, K. (2015, February). CO2 Capture and Storage in Portugal. *A Bridge to a Low Carbon Economy*, p. 43.

Smith, J., Durucan, S., Korre, A., & Shi, J. (2011). Carbon dioxide storage risk assessment: Analysis of caprock fracture network connectivity. *International Journal of Greenhouse Gas Control*, 226-240.

Strategy CCUS. (2021). *D1.8 – Publishable Summary of Project first period.*

Tejo Energia. (2011). *Estudo de viabilidade de adopção de captura e armazenagem de CO2 na Central Termoelétrica do Pego.* Retrieved from https://www.uevora.pt/investigar/projetos?id=1615

Terrinha, P., Neres, M., Duarte, J., Silva, S., Mata, J., & Matias, L. (2019). The Alpine Orogeny in the West and Southwest Iberia Margins. *The Geology of Iberia: A Geodynamic Approach*, 487–505.

UNFCCC. (2022). *United Nations Climate Change Annual Report 2022.* UNFCCC.

United Nations. (1992). *United Nations Framework Convention On Climate Change.* Bonn, Germany: UNFCCC.

World Bank. (2017). *Report of the High-Level Comission on Carbon Prices.* Carbon Pricing Leadership Coalition.

World Bank. (2023). *Carbon Pricing Dashboard*. Retrieved from Carbon Pricing Dashboard: https://carbonpricingdashboard.worldbank.org/

Yuhang Wang, C. V. (2021). International Journal of Greenhouse Gas Control . *CO2 Storage in deep saline aquifers: impacts of fractures on hydrodynamic trapping*, p. 18.

Zhang, D. a. (2014). Mechanisms for geological carbon sequestration. *23rd International Congress of Theoretical and Applied Mechanics* (pp. 319-327). Beijing, China: Elsevier Ltd.

Zoback, M., & Gorelick, S. (2012). Proceedings of the National Academy of Sciences. *Earthquake triggering and large-scale geologic storage of carbon dioxide*, p. 5.

Appendix

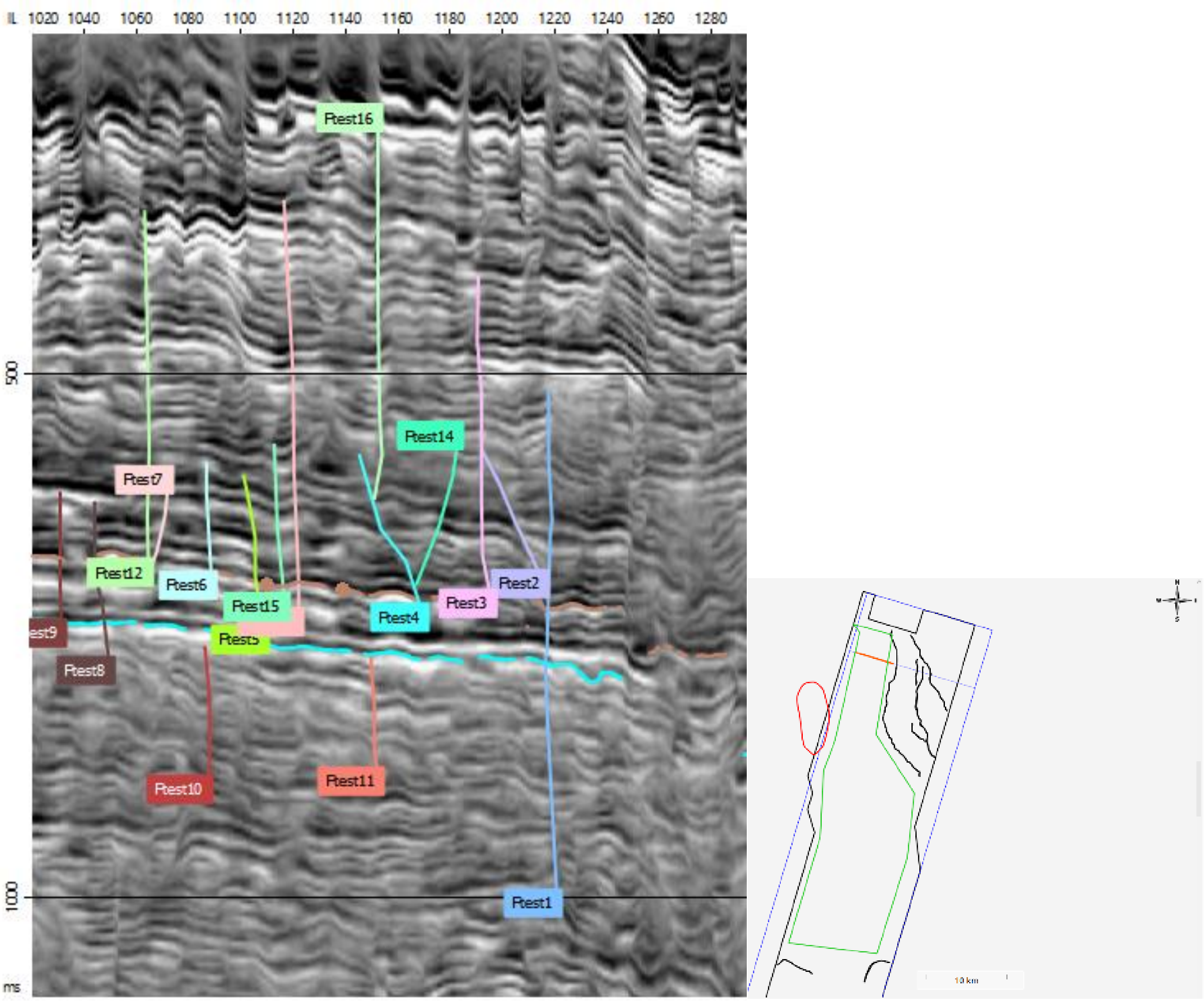

Appendix 1- Fracture Interpretation on Crossline 14475 (left) and Line location (right)

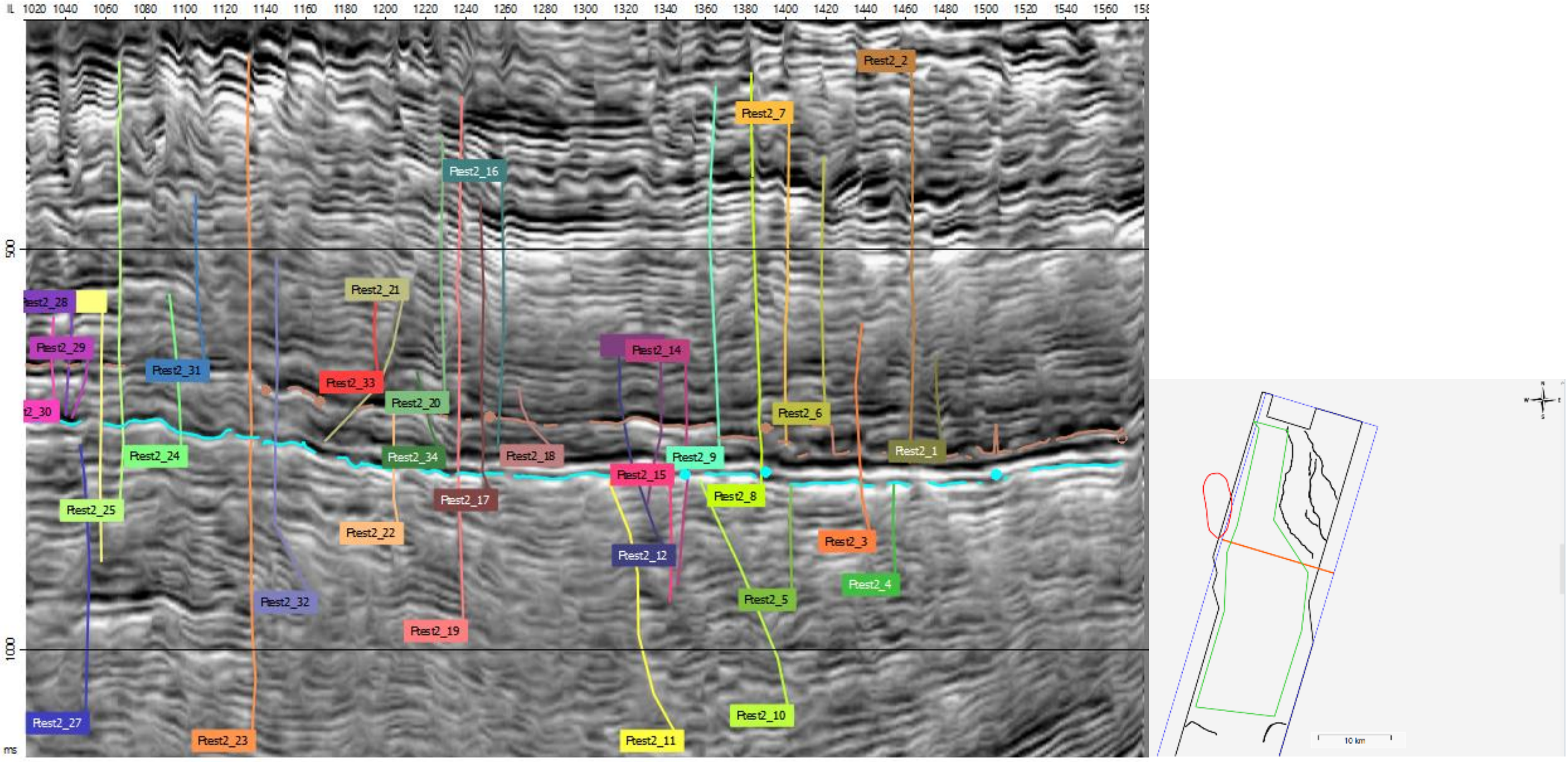

Appendix 2- Fracture Interpretation on Crossline 12315 (left) and Line location (right)

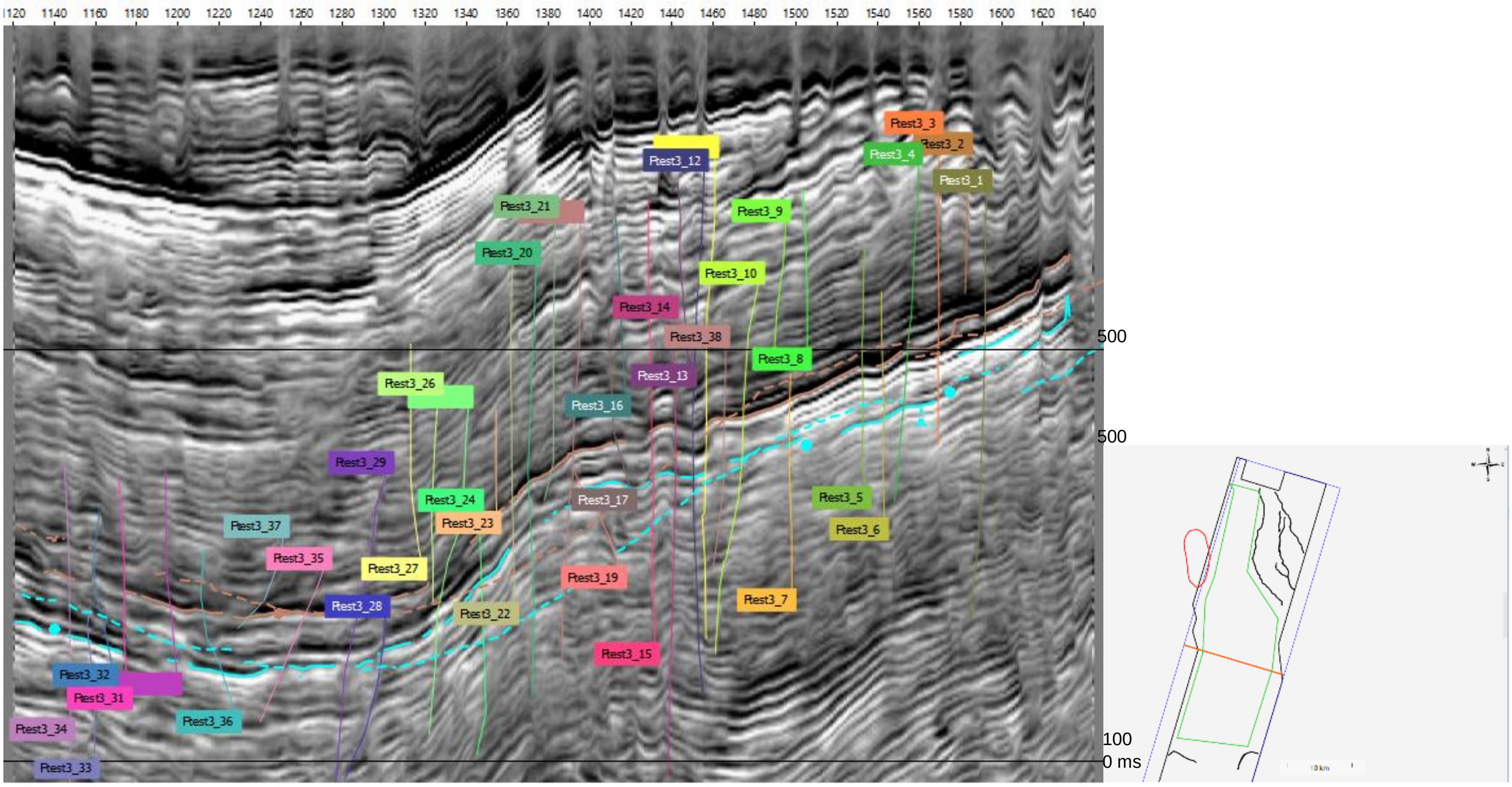

Appendix 3- Fracture Interpretation on Crossline 10875 (left) and Line location (right)

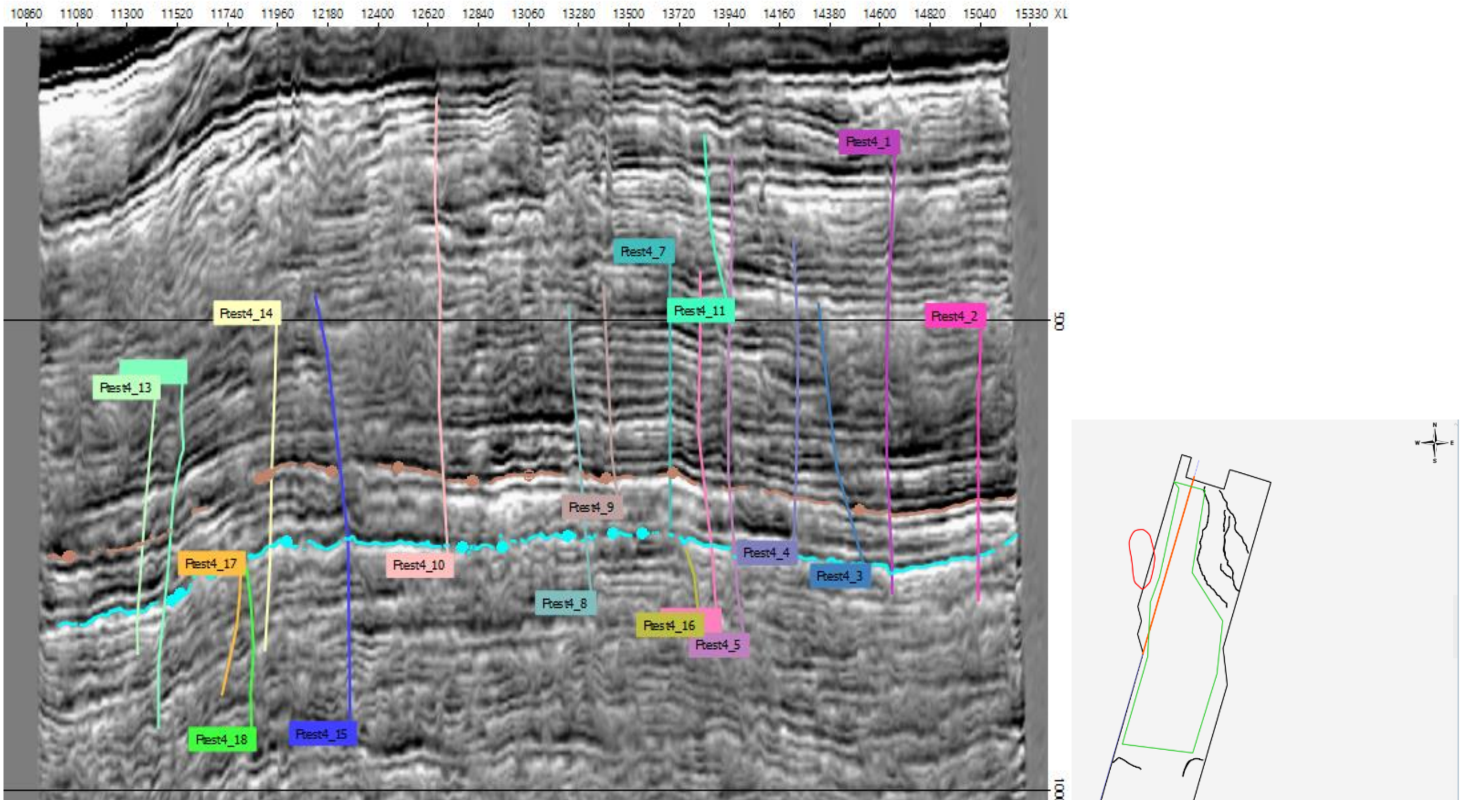

Appendix 4- Fracture Interpretation on Inline 1110 (left) and Line location (right)

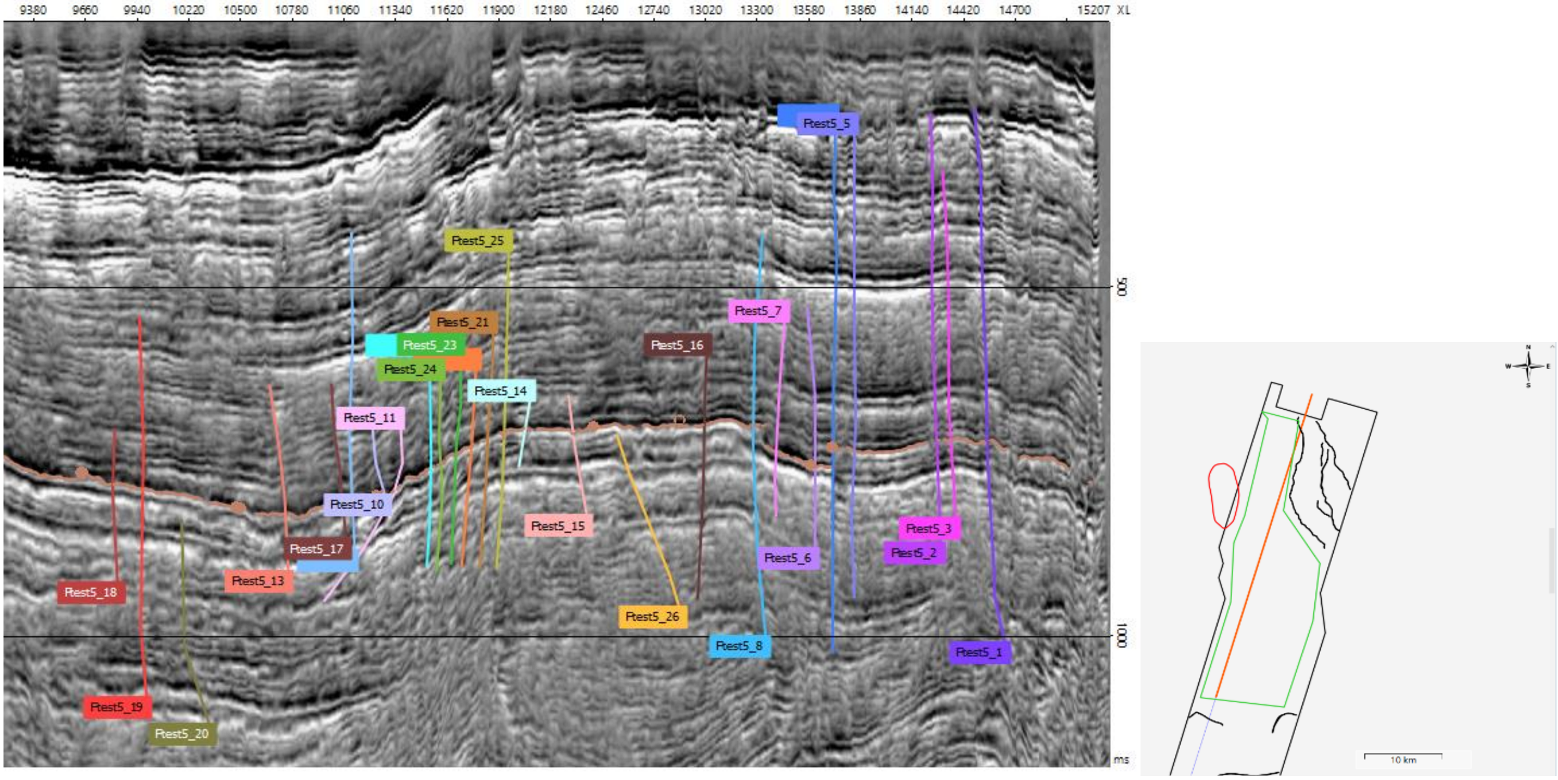

Appendix 5- Fracture Interpretation on inline 1220 (left) and Line location (right)

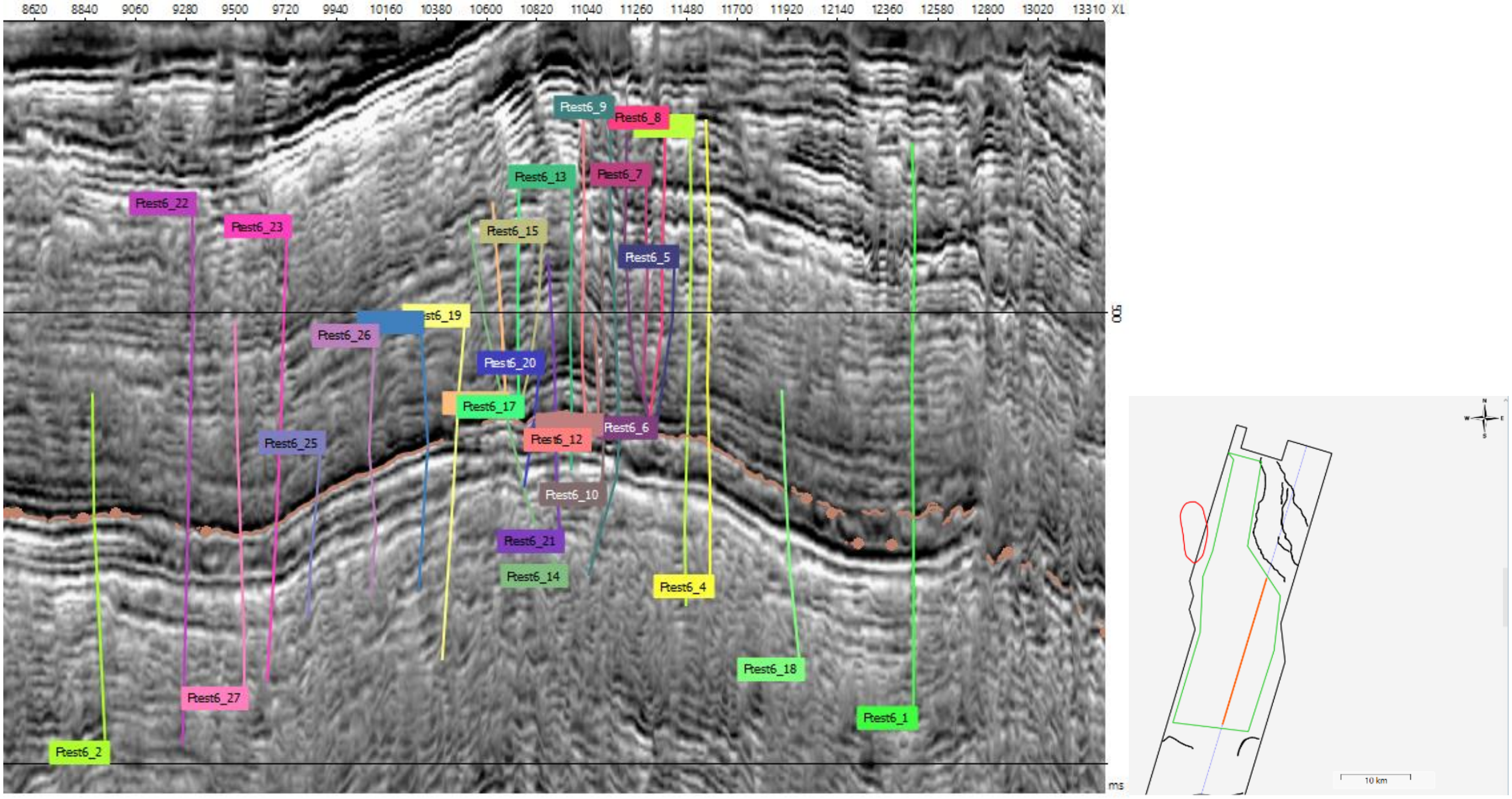

Appendix 6- Fracture Interpretation on Inline 1420 (left) and Line location (right)

Appendix 7- ESE Family (left) and NNE Family (right) Fracture Intensity Results per interval (columns) and sections (lines)

Fractures ESE	**SB-C**	**C-TVG**	**TVG-Alc**
Main 1	0.080692	0.5209302	0.1297753
Small 1	0	0.2799552	0.1158279
1.1	0	0.5592841	0.2458815
1.2	0	1.1261261	0.4737091
1.3	0	0.5230126	0.2187705
Small 2	0.064292	0.5554784	0.2392774
2.1	0	1.015744	0.4710316
2.2	0.246154	0.999001	0.4781257
Small 3	0.247498	1.1290323	0.0790889
3.1	0	0.6489293	0
3.2	0.318573	1.3869626	0
3.3	0.901597	4.4080605	0.3087373
3.4	0.944882	3.6968577	0.3676471
Small 4	0.096429	0.4737091	0.1998668
4.1	0.354359	1.7974835	0.7594937
4.2	0.12216	0.6265664	0.2662407
4.3	0.150625	0.6578947	0.2766252
4.4	0.383583	1.9379845	0.8132285
Main 2	0.054626	0.5934718	0.2319647
Small 5	0.031283	1.0217486	0.5498198
5.1	0.114469	3.5608309	1.521684
5.2	0	2.3269343	1.1355894
5.3	0	0.554939	0.7082153
5.4	0	1.2158055	0.5281225
Small 6	0.197336	1.8410042	0.6496143
6.1	0.778412	6.9664345	2.240717
6.2	0.580383	2.514142	0.3631082
6.3	0	1.330672	0.591716
6.4	0	0	0
Small 7	0.03202	0.575374	0.2356129
7.1	0	0	0
7.2	0.127845	1.7533606	0.7213272
7.3	0	1.1737089	0.4663092
Small 8	0.028947	0.1819174	0.068055
8.1	0.122205	0.7077141	0.2655337
8.2	0	0	0
Main 3	0.033879	0.1788909	0.0567354
Small 9	0.03098	0.1591343	0.0654536
9.1	0	0	0.2281542
9.2	0.122624	0.6493506	0.3210273
Small 10	0.125247	0.7696748	0.1466168
10.1	0.364166	1.285347	0.5267316
10.2	0.485732	3.2867707	0.661157
10.3	0	0	0

Fractures NNE	**SB-C**	**C-TVG**	**TVG-Alc**
Main 1	0.129107	1.190698	0.5191013
Small 1	0.059855	1.399776	0.5791394
1.1	0	0	0
1.2	0.110181	5.067568	2.1316911
1.3	0.123305	1.046025	0.437541
Small 2	0	0	0
2.1	0	0	0
2.2	0	0	0
Small 3	0.494997	3.548387	1.7399557
3.1	0.507292	3.244646	1.4269406
3.2	0.159286	0.693481	0.3146633
3.3	1.030397	7.556675	3.7048472
3.4	1.102362	6.777572	4.0441176
Small 4	0	0	0
4.1	0	0	0
4.2	0	0	0
4.3	0	0	0
4.4	0	0	0
Main 2	0.023411	0.118694	0.0994135
Small 5	0	0	0.0610911
5.1	0	0	0
5.2	0	0	0
5.3	0	0	0.2360718
5.4	0	0	0
Small 6	0.098668	0.502092	0.3248071
6.1	0.259471	1.266624	0.6402049
6.2	0.145096	0.628536	0.3631082
6.3	0	0	0
6.4	0	0	0.3272251
Small 7	0	0	0.1178064
7.1	0	0	0.2375297
7.2	0	0	0.2404424
7.3	0	0	0
Small 8	0	0	0.13611
8.1	0	0	0.5310674
8.2	0	0	0.2979738
Main 3	0.076229	0.402504	0.0567354
Small 9	0	0	0
9.1	0	0	0
9.2	0	0	0
Small 10	0.281805	1.731768	0.2199252
10.1	0.849721	4.498715	0.2633658
10.2	0.364299	2.465078	0.9917355
10.3	0.123335	0.70028	0

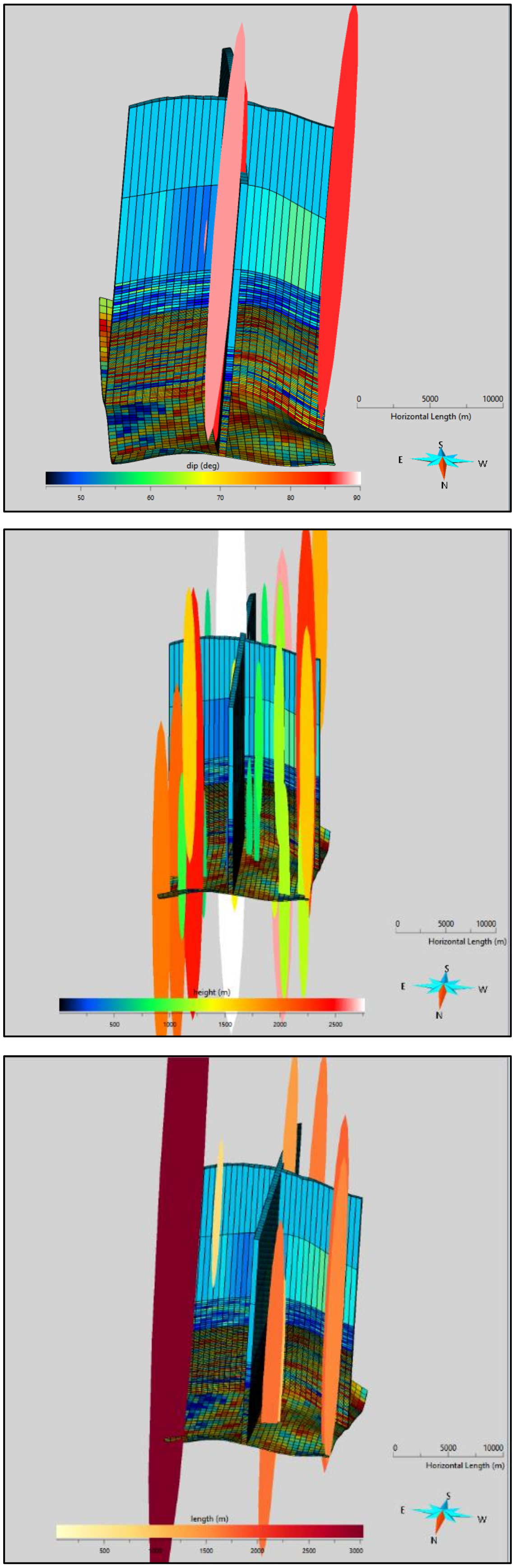

Appendix 8- ESE Family Best-Case Models (left) and Average-Case Models (right) with Reservoir Grid

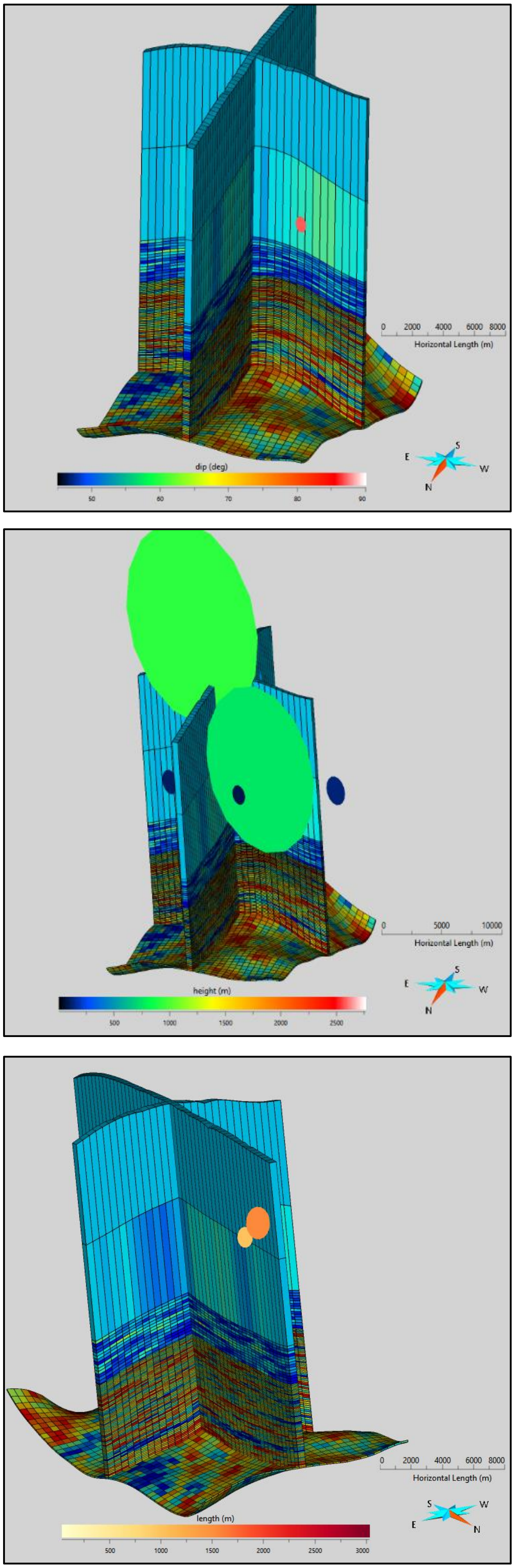

Appendix 9- NNE Family Best-Case Models (left) and Average-Case Models (right) with Reservoir Grid